A MINIMAL THREE-DIMENSIONAL TROPICAL CYCLONE MODEL

Dissertation
in the Physics Faculty at the
Ludwig-Maximilians-University
Munich

by

Hongyan Zhu
from
Wendeng

Munich, 15 April, 2002

First Examiner: Prof. Dr. Roger Smith

Second Examiner: Prof. Dr. Ulrich Schumann

Date of the Oral examination: 17, 07, 2002

Abstract

A minimal three-dimensional numerical model designed for basic studies of tropical cyclone behaviour is described. The model is formulated in σ-coordinates on an f- or β-plane and has three vertical levels, one characterizing a shallow boundary layer and the other two representing the upper and lower troposphere, respectively. It has three options for treating cumulus convection on the subgrid scale and a simple scheme for the explicit release of latent heat on the grid scale. The subgrid-scale schemes are based on the mass-flux models suggested by Arakawa and Ooyama in the late 60s, but modified to include the effects of precipitation-cooled downdrafts. They differ from one another in the closure that determines the cloud-base mass flux. One closure is based on the assumption of boundary-layer quasi-equilibrium proposed by Raymond and Emanuel.

It is shown that a realistic hurricane-like vortex develops from a moderate strength initial vortex, even when the initial environment is slightly stable to deep convection. This is true for all three cumulus schemes as well as in the case where only the explicit release of latent heat is included. In all cases there is a period of gestation during which the boundary-layer moisture in the inner core region increases on account of surface moisture fluxes, followed by a period of rapid deepening. Precipitation from the convection scheme dominates the explicit precipitation in the early stages of development, but this situation is reversed as the vortex matures. These findings are similar to those of Baik *et al.* who used the Betts-Miller parameterization scheme in an axisymmetric model with eleven levels in the vertical. The most striking difference between the model results using different convection schemes is the length of the gestation period, whereas the maximum intensity attained is similar for the three schemes. The calculations suggest the hypothesis that the period of rapid development in tropical cyclones is accompanied by a change in the character of deep convection in the inner core region from buoyantly-driven, predominantly upright convection to slantwise forced moist ascent.

The roles of shallow convection, precipitation-cooled downdrafts, and the vertical transport of momentum by deep convection on vortex evolution in the model are investigated. We explore also the sensitivity of the calculations to changes in horizontal resolution, sea surface temperature, the sea surface energy exchange coefficient, the initial vortex strength, the time scale for deep convection, and the inclusion of dissipative heating. The findings are compared with those of other studies.

We explore two different methods: the Charney-Philips grid (CP-grid) and the Lorenz-grid (L-grid), for discretizing equations in the vertical. We find evidence that a computational mode in the temperature field in the L-grid model is excited during the period of rapid vortex intensification. The comparison shows that the vortex asymmetries that develop during the mature stage are sensitive to the choice of vertical grid and those that occur in the CP-grid are more realistic.

CONTENTS

Chapter 1. Introduction 1

1.1 Overview of tropical cyclones 1

1.2 Buoyancy and convection 5

1.3 Moist convection 6

1.4 Representation of convection schemes in tropical cyclone models 8

1.5 Simple tropical cyclone models 11

1.6 Motivation 14

Chapter 2. Description of the model 16

2.1 Governing equations 16

2.2 Explicit moist processes 17

2.3 Radiative cooling 17

2.4 Surface turbulent fluxes 18

2.5 Boundary and initial conditions 18

2.6 Subgrid-scale diffusion 19

2.7 Numerical methods 20

Chapter 3. Cumulus parameterizations schemes 21

3.1 The cloud model 21

3.2 Subgrid-scale heat and moisture sources 24

3.3 Downdraft thermodynamics 25

3.4 The modified 1969-Arakawa scheme 26

3.5 The modified 1995-Emanuel scheme 27

3.6 The modified 1969-Ooyama scheme 28

Chapter 4. Control experiment 29

4.1 Overview of vortex evolution 29

4.2 Details of vortex evolution 31

4.3 Summary 38

Chapter 5. The role of three important physical processes 41

5.1 Inclusion of shallow convection 41

5.2 Exclusion of precipitation-driven downdrafts 51

5.3 Inclusion of vertical momentum transfer by parameterized convection 55

5.4 Summary 59

Chapter 6. Sensitivity studies on the model parameters 61

6.1 Effect of horizontal resolution 61
6.2 Effect of sea surface energy exchange coefficient 62
6.3 Sensitivity to the sea surface temperature 64
6.4 Inclusion dissipative heating 66
6.5 Weak initial vortex 67
6.6 Sensitivity to convection time scale 67
6.7 Sensitivity to variants of the mass flux formulation in the Emanuel scheme 69
6.8 Summary 70

Chapter 7. Effects of vertical differencing 71

7.1 Definition of L-grid, A-grid and CP-grid 71
7.2 Governing equations in the CP-grid model 73
7.3 The vertical differencing in the CP-grid model 73
7.4 Physical process in the CP-grid and L-grid models 75
7.5 Comparison of results with the L-grid and CP-grid 76
7.6 Summary 85

Chapter 8. Model appraisal 87

Chapter 9. Summary and conclusions 89

Appendix 92

A. The initial sounding data 92
B. Some details of the numerical method 92
C. Conservation equation for part or all of a grid cell 93
D. Calculation of the cumulus precipitation 95
E. Maximum potential intensity (MPI) theory 95
F. Derivation of the dissipative heating 98
G. Discrete equations for the CP-grid model 99

References 103

Acknowledgements

Curriculum vitae

Chapter 1. Introduction

1.1 Overview of tropical cyclones

Tropical cyclone are nearly circular, warm-core intense vortical storms which develop over the tropical oceans in regions of very warm surface water. Strong winds and precipitation are concentrated near their centers, typically within a radius about 100 km. Coincident with the strongest winds, convective updrafts, fed by inward spiraling surface winds, release latent heat drawn from the ocean to power the storm. The clear eye, which is 15-30 km in radius, contains the axis of vortex rotation and is surrounded by the strongest winds. The eye is characterized by the warmest temperatures in the vortex, low humidity, low pressure, in extreme cases more than 10 percent below that in the undisturbed tropical atmosphere, and low speed winds.

Tropical cyclones have different names in the different regions. They are called *hurricanes* in the Atlantic and East Pacific regions, *typhoons* in the Western North Pacific and simply *tropical cyclones* in the Australian and South Pacific regions.

TABLE 1. Saffir-Simpson Scale

Saffir-Simpson Scale	Max.Wind Speed (mph) [knots]	Minimum Sfc. Pressure (mb)
1	74-95 [64-83]	>= 980
2	96-110 [84-96]	979-965
3	111-130 [97-113]	964-945
4	131-155 [114-135]	944-920
5	> 156 [> 135]	< 920

The simplest characterization of hurricane intensity in the Atlantic and East Pacific regions is the Saffir-Simpson scale: from Category 1 —barely a hurricane— to Category 5 —the worst imaginable (see Table 1). Category 5 hurricanes are the most extreme and also the most rare. Only two, the 1935 Labor Day Storm and Camille in 1969 are recorded to have struck the United States. Andrew, at the very top of Category 4 was the third strongest U.S. landfall, which caused the United States' most expensive natural disaster with 27 billion US dollar's worth of property destroyed.

A typical hurricane intensifies slowly, remaining in Category 1 or reaching 2 or even 3 before it runs ashore or drifts north out of the tropics. The strongest hurricanes, such as Andrew in 1992, intensify rapidly and go from Category 1 or 2 to Category 4 or 5

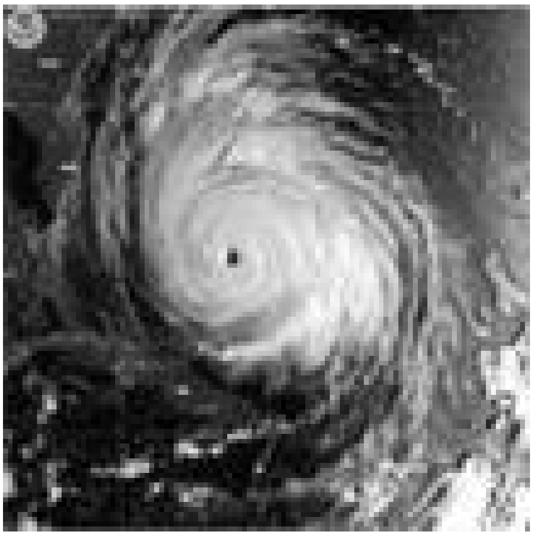

Figure 1. Satellite image of Hurricane Oliver (1994)(from Hurricane Research Division (HRD)).

in just a day or two.

For the Australian region and in international practice, the warning terminology is different from the Saffir-Simpson scale. The classification is:

Strong Wind Warning:	Winds averaging 25 to 33 kn.
Gale Warning:	Winds averaging 34 to 47 kn.
Storm Warning:	Winds averaging 48 to 63 kn.
Hurricane Warning:	Winds averaging more than 63 kn.

The satellite image of Hurricane Oliver (1994) in Fig. 1 shows the essential structure of a tropical cyclone: a clear eye enclosed by a ring of clouds, which is in turn surrounded by inward spiraling bands of convection. These features are common to all tropical cyclones.

A cross-section of a tropical cyclone in the radius-height plane (Fig. 2) shows that the mature tropical cyclone consists of a horizontal quasi-symmetric circulation (primary circulation) on which is superposed a thermally-direct vertical circulation (secondary circulation). Due to the surface friction in the boundary layer, which is typically about 500 m deep in the tropics, the counter-clockwise spiraling air near the surface converges toward the lower pressure and rises around the eye in deep cumulus clouds, the so-called eyewall region. Although the inflowing air loses absolute angular momentum* to the sea, it gains heat stored as water vapour. In the tropical cyclone, the

* The total absolute angular momentum per unit mass is $M = rV + \frac{f}{2}r^2$, where r is the physical radius, f is the Coriolis parameter and V is the tangential wind component.

air in the boundary layer is moistened as it spirals inwards over the warm ocean, and it expands and cools, and condenses when it is forced upwards out of the boundary layer. The latent heat released from the condensation is responsible for the warm core in the cyclone. A small fraction of the heat released appears as an elevated temperature perturbation at a particular height, which is responsible for the cyclone spinup by producing the convergence above the boundary layer, and most of it is balanced by the adiabatic cooling that occurs as air parcels continue to rise and expand. Rotunno and Emanuel (1987) explained the tropical cyclone as a type of Carnot engine. As the vortex intensifies, the surface pressure decreases, which results in an increase of the saturation mixing ratio at the sea surface temperature. With increasing surface wind and surface saturation mixing ratio, the surface fluxes between the ocean and the boundary layer air increase. As a result the subcloud-layer equivalent potential temperature rises above the ambient values and the vortex core becomes warmer than its environment. When the vortex is saturated in the eye wall region, the radial gradient of virtual temperature is determined by that at the top of the boundary layer because the saturation equivalent potential temperature is conserved along the moist adiabatic ascent and the virtual temperature of an air parcel at a particular pressure level is a monotonically-increasing function of its saturation equivalent potential temperature. In the tropical cyclone, the updrafts may rise as high as 16 km where the air flows outward to the environment. The source of the storm's energy is the heat drawn from the warm sea surface at 28-29^{o}C and this heat is returned to the surrounding upper atmosphere at a temperature of about -70^{o}C.

The center of the tropical cyclone is free of deep cloud. As shown in Fig. 1, the deep clouds that enclose the eye form the eyewall. These clouds entrain air from the eye at low levels, and descending motion caused by the vertical perturbation pressure gradient in the eye region dries, and warms inside the eye. As the air warms, it becomes less dense so that the surface pressure falls. The clouds also draw air radially inward from outside the eye, thus concentrating the counter-clockwise rotation and increasing the swirling winds. In a tropical cyclone, the strongest winds are near the surface and just outside the eyewall even though there is the strongest friction there as well. A study by Smith (2002) examined the development of a region of super-gradient winds* in the surface boundary layer of a model cyclone. The calculations show that supergradient winds are to be expected because air parcel suffer large inward displacements in the boundary layer. Even though absolute angular momentum is only partially conserved in this layer, large tangential wind speeds that can be attained can exceed those that exist locally above the boundary layer.

Hurricane track forecasts have improved steadily over the past three decades, ow-

---

* Supergradient means that the sum of the centrifugal and Coriolis forces exceeds the inwards-directed radial pressure gradient so that the net force is radially outwards.

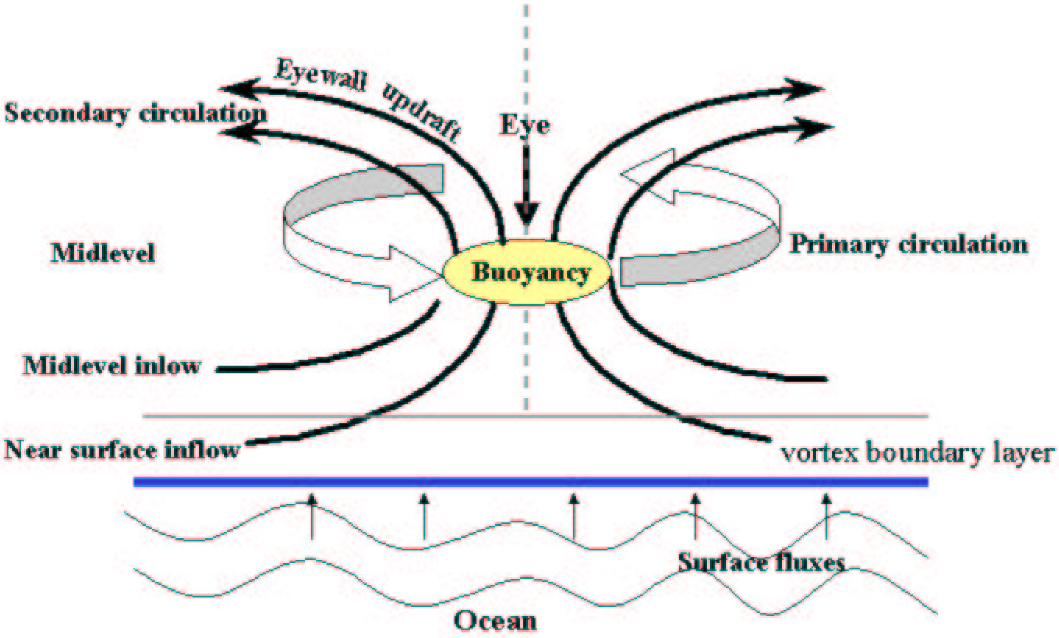

Figure 2. Schematic vertical cross-section of tropical cyclone showing the primary (tangential) and second (vertical) circulation

ing to a combination of better observations, much improved understanding of vortex motion and much improved numerical models (DeMaria and Kaplan, 1997). These improvements, coupled with advances in warning systems and emergency preparedness, have brought about a significant decline in loss of life. In contrast to the improvement in track forecasts, there has been comparatively little advance in predictions of intensity change, in spite of the application of sophisticated numerical models. Part of the reason is that the physical processes associated with moist convection and its interaction with the larger-scale flow are incompletely understood and their representation in atmospheric models still leaves much to be desired. As an example, the experience with Hurricane Opal of 1995 demonstrates that intensity predictions compare poorly to the skill exhibited by track forecasts[†]. Hurricane Opal was a category 2 hurricane that strengthened to a category 5 overnight. In the morning the storm struck a populated coastline where the residents had prepared for a weaker hurricane which they saw on the television before they went to bed. Forecasters at the National Hurricane Center use half a dozen of models to guide track forecasts. For intensity forecasting, only one model has been available (until recently) and that was based on climatology and persistence. These rudimentary tools indicate the challenge of forecasting intensity and our inadequate understanding of moist processes. There is an acute need to improve the representation of moist convective processes in the forecast models of tropical cyclones. The work in this thesis mainly seeks to understand the transport of heat, water and momentum by moist convection in an idealized tropical cyclone model and how the representation of convection has an effect on the evolution of model tropical cyclones.

[†] see http://www. aoml.noaa.gov/general/WWW000/text/opal.html/

1.2 Buoyancy and convection

If a body lighter than a fluid be forcibly immersed in it, the body will be driven upwards by a force equal to the difference between its weight and the weight of the fluid displaced.

——————Archimedes , circa B.C.

According to Emanuel (1994), "convection encompasses only a class of relatively small-scale, thermal direct circulations which result from the action of gravity upon an unstable vertical distribution of mass, with "vertical " taken to mean "along the gravitational vector." " The restricted definition of convection includes a broad variety of phenomena in planetary atmospheres, from the structure of the planetary boundary layer to the dynamics of tropical cyclones. Moist convection is organized over many scales, from microscopic turbulence to squall lines and tropical cyclones.

In order to understand the nature of convection in the atmosphere, it is necessary to understand the buoyancy force in fluid dynamics.

If an isolated body of density ρ_1 is immersed in a fluid of density ρ_2, the buoyancy force per unit mass is

$$B = g\frac{(\rho_2 - \rho_1)}{\rho_1}. \tag{1}$$

where g is the gravitational acceleration. The assumption is that the pressure distribution around the body is determined by the hydrostatic pressure in the far environment.

For an ideal gas $p = \rho RT$, where p is the pressure, R is the gas cnstant for dry air, the bouyancy force can be written in terms of temperature or potential temperature alone :

$$B = g(\frac{T'}{\overline{T}}) \quad or \quad B = g(\frac{\theta'}{\overline{\theta}}), \tag{2}$$

where T' is the temperature deviation from the environmental value $\overline{T}$ and θ' is the potential temperature deviation from the environment value of $\overline{\theta}$. However we have to bear in mind that Eq. (2) is satisfied on the assumption that the pressure in the air parcel is equal to the pressure in the far environment. The expression (2) may not be accurate in the case of the intense vortex in which the central pressure is much less than that in the environment at the same level. In a rapidly-rotating axisymmetric vortex, an air parcel experiences not only the gravitational force, but also a centrifugal force v^2/r and Coriolis force fv, where v is the tangential wind component at radius r and f is the Coriolis parameter. As a result, isobaric surfaces have a vertical slope that is normal to the effective gravity, $\mathbf{g_e} = (v^2/r + fv, -g)$ as shown in Fig. 3. Then the Archimedes' force acting on the parcel is $-\mathbf{g_e}\rho_o$ and the effective weight of the parcel is

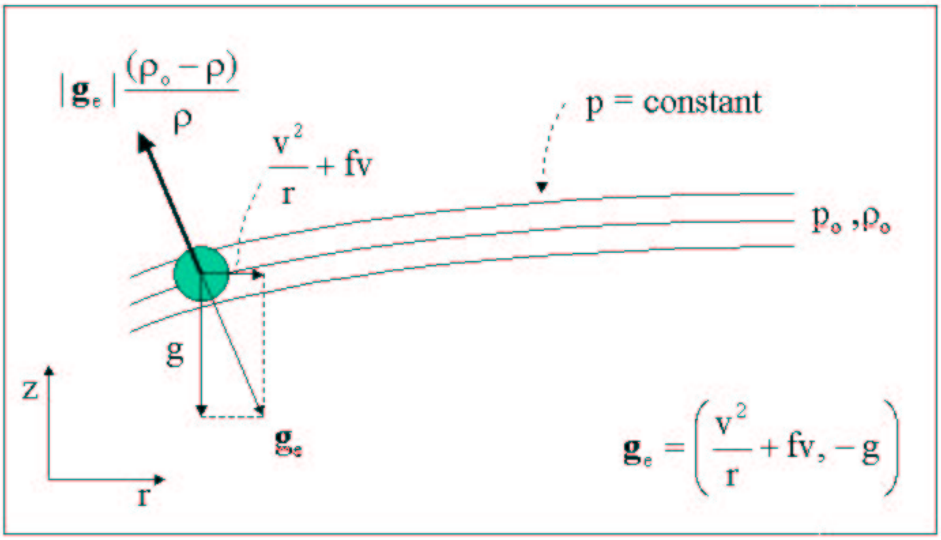
$|\mathbf{g}_e|\frac{(\rho_o-\rho)}{\rho}$
$\frac{v^2}{r}+fv$
p = constant
p_o, ρ_o
g
$\mathbf{g}_e$
z
r
$\mathbf{g}_e = \left(\frac{v^2}{r}+fv, -g\right)$

Figure 3. Schematic radial-height cross-section of isobaric surfaces in a rapidly-rotating vortex showing the forces on an air parcel including the gravitational force and the centrifugal and Coriolis forces. The Archimedes force $-\mathbf{g_e}\rho_o$ slopes upwards and outwards while the weight $\mathbf{g_e}\rho$ slopes downwards and inwards. Thus the net force acting on the parcel is $|\mathbf{g_e}|(\rho_o - \rho)/\rho$, which if $\rho < \rho_o$ is in the direction shown.

$\mathbf{g_e}\rho$, where ρ_o is the far-field density along the same isobaric surface as the parcel. If the parcel has a different tangential wind speed v' to that of its environment v, as might be the case, for example, if it were displaced to its current position while conserving its absolute angular momentum, then the *net* radial force that it experiences per unit mass will be equal to $\mathrm{g}[\rho(v'^2/r + fv') - \rho_o(v^2/r + fv)]/\rho$, a generalization of the radial component of the buoyancy force. We examine now how air parcels acquire buoyancy.

1.3 Moist convection

As air rises in the atmosphere it expands. In the absence of heat sources or sinks it cools at the dry adiabatic lapse rate (DALR). If the sample contains any water vapour, the point is finally reached where it is so cold that the vapour begins to condense into liquid water or ice, the so called lifting condensation level (LCL). When water vapour condenses, it releases latent heat to the air. For an incremental change in water vapour mixing ratio, dr, the quantity of heat released is given by $Q = -L_v dr$, where L_v is the latent heat vaporization of water. So, as saturated air continues to rise past its LCL, the release of latent heat prevents the temperature from falling as fast as the DALR. The new rate of decrease of temperature is called the moist adiabatic lapse rate, which unlike the DALR is not a constant. There are two approximations for a moist adiabatic process, the reversible-adiabatic and the pseudo-adiabatic process. The difference is that in the pseudo-adiabatic process all the condensed water is assumed to be immediately (and irreversibly) removed from the system, while in the reversible adiabatic case, all the water is assumed to be carried along by the system. Pseudo-adiabatic is a better approximation for deep convection (Mapes and Houze, 1992)

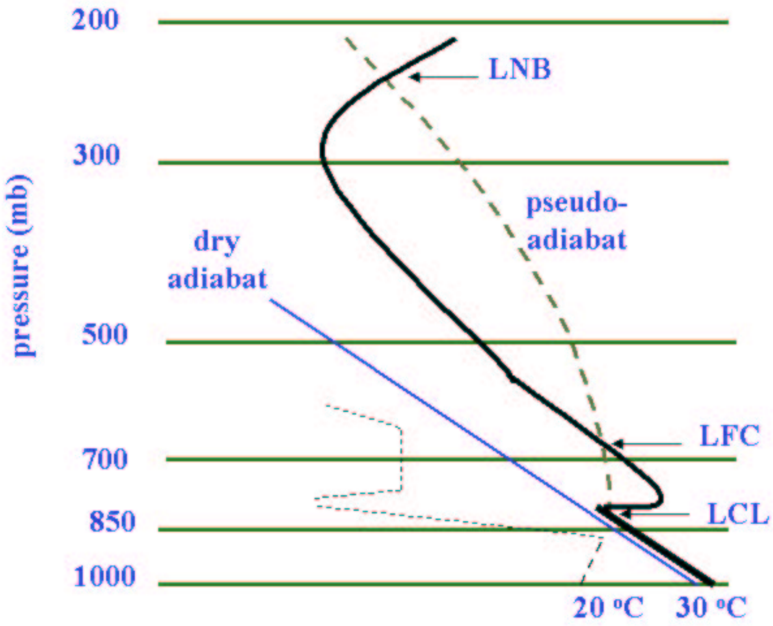

Figure 4. Thermodynamic diagram showing an example of an atmospheric sounding. The straight line shows a dry adiabat, while dashed curve shows a pseudo-moist adiabat. Thick solid and dashed lines show the measured temperature and dew point, respectively.

and reversible-adiabatic is a better choice for the non-precipitating shallow convection (Betts, 1986).

The traditional way of assessing the stability of the atmosphere to moist convection is the thermodynamic diagram. An example is shown in Fig. 4, where the solid thin line is a dry adiabat, and the dashed curve is a pseudo-adiabat. The LCL is where the actual temperature of environment first crosses the pseudo-adiabat line and an air parcel, which is lifted from the surface, becomes saturated. The pressure (or height) level at which the rising air parcel first acquires positive buoyancy is called level of free convection (LFC), and the pressure (or height) level at which it once again becomes negatively buoyant is called the level of neutral buoyancy (LNB).

The amount of energy per unit mass required to lift an air parcel to its LFC is called the convective inhibition (CIN) and the amount of energy per unit mass that can be released if the parcel reaches the LFC and rises to its LNB is called the convective available potential energy (CAPE). The potential energy for the generation of kinetic energy by evaporation in saturated precipitation-cooled downdraughts is called the downdraught convective available potential energy, or DCAPE. In this thesis, I mainly explore deep convection in tropical cyclones. The condition for deep convection requires the moist static energy* in the boundary layer to be larger than the saturated moist

[*] $h = c_pT + Lq + \Phi$, where c_p is the specific heat of dry air, T is the temperature, q is the mixing ratio and

static energy[†] in the middle and upper troposphere to enable the air parcel to rise to its LFC and release CAPE. The assumption is that there is no CIN, which is a reasonable approximation over the tropical oceans where values of CIN are relatively small.

The question now is how deep clouds heat the surrounding atmosphere. Numerical experiments with idealized deep convective cloud in a stably-stratified non-rotating environment suggest that subsidence occurs at the leading edge of a horizontally-propagating internal gravity wave (Bretherton and Smolarkiewicz, 1989; Nicholls *et al.*, 1991, Bretherton, 1993; Mapes, 1993). This subsidence leads to an adiabatic temperature rise in the cloud environment and tends to adjust the cloud-free environment towards the moist adiabatic lapse rate found in the cloud. At the same time, downdraughts that form during the cloud life cycle will also generate gravity waves associated with negative buoyancy perturbations and these downdraughts must produce ascent and adiabatic cooling in the environment to offset the warming by subsidence. In a rotating atmosphere, neglecting the effects of radiative cooling, the temperature perturbation produced by the subsidence must spread out on the order of a Rossby deformation radius[*], which is typically 1000 km or more in the undisturbed tropics, but may be much smaller in cyclonic disturbances, such as tropical cyclones (Shutts and Gray, 1994). Generally the deformation radius decreases as the circulation strength increases and may be only a few tens of kilometers in the core of a tropical cyclone (Ooyama, 1982).

1.4 Representation of convection schemes in tropical cyclone models

Cumulus convection is one of the central physical processes in tropical cyclone dynamics and it needs to be represented in tropical cyclone models. As explained in section 1.1, the vortex intensifies as a result of radial buoyancy gradients in the core region associated with convective heating. The fact that such buoyancy gradients are produced by all cumulus parameterization schemes, as well as by explicit schemes for latent heat release, explains why all the models with paramerization schemes are able to simulate tropical cyclone intensification with some degree of realism irrespective of the scheme (Smith 2000). However, convective clouds occur on scales that are typically too small to be resolved by numerical models and their collective effects must be represented, or parameterized, in terms of variables defined on the model grid.

Φ is the geopotential height.

[†] $h^* = C_pT + Lq^* + \phi$, q^* is the saturation mixing ratio

[*] The Rossby deformation radius is a natural length scale for adjustment in a rotating stratified fluid. For an axisymmetric disturbance with depth scale H, it is defined as NH/I, where N is the buoyancy frequency associated with the stable stratification and I is the inertial stability parameter defined by $I^2 = (f + \zeta)(f + 2v/r)$, where ζ is the vertical component of relative vorticity, f is the Coriolis parameter and v is the tangential velocity component at radius r (see e.g. Shapiro and Willoughby, 1982, Frank, 1983). For weak disturbances, $I \approx f$.

Parameterization is a scientific question rather than a technical problem in modelling.

There are three broad groups of parameterization schemes to represent cumulus convection in tropical cyclone models.

- Convection schemes based on the assumption of moisture convergence;
- Schemes based on the idea of moist convective adjustment;
- Schemes based on the assumption of quasi-equilibrium.

The Kuo-scheme (Kuo, 1965, 1974) has been widely used for its simplicity. It is based on the idea that convection occurs where there is moisture convergence. There is a near balance between precipitation and the vertical transport of water by the large-scale flow where deep convection occurs. Deep cumulus convection occurs in regions where the stratification is conditionally unstable, but only if there is low-level moisture convergence. A pseudo-moist adiabat is assumed.

A problem with the Kuo scheme (1965) is that too much of the water vapour that converges in a grid column is used to moisten the atmosphere, whereupon too little is available to heat the atmosphere and precipitate (see e.g. Kitade, 1980, p475). An extended version of the scheme was presented by Kuo (1974), in which the rate of moistening integrated over a vertical column of the atmosphere is equal to a small fraction b of the precipitation rate. Its physical basis has been seriously challenged in recent years (Raymond and Emanuel, 1993; Emanuel, 1994). There seems to be little scientific or observational basis for the assumption that the rate of moistening integrated over a vertical column of the atmosphere is equal to a small fraction of the precipitation rate. As it stands, the scheme would not be activated in a conditionally-unstable environment with no basic flow and zero CIN. It is unable to produce a realistic moistening of the atmosphere in a radiative-convective calculation for zero basic flow.

Rosenthal (1970a) describes a numerical model formulated in σ-coordinates having 7 levels vertically. As in the Kuo schemes, convection occurs only in the presence of low-level convergence and conditional instability. Moreover, there is no moistening of the atmosphere. Thus all the latent heat released is made available to the large-scale flow. At the same time, the vertical distribution of this heating adjusts the large-scale lapse rate towards a pseudo-adiabat. The same scheme was used in an asymmetric tropical cyclone model by Anthes *et al.* (1971a,b), Rosenthal (1970b, 1971), and a slightly modified form by Anthes (1972) and Yamasaki (1968a,b).

Adjustment schemes are based on the simple principle that convection tends to adjust the virtual temperature of the atmosphere back towards some equilibrium state.

Moist convective adjustment is applied to any model layer that becomes saturated and in which the lapse rate exceeds the moist adiabatic lapse rate. The moist static energy of the layer is held fixed during the adjustment. The equivalent potential temperature (θ_e) is constant with height after the adjustment. The total amount of precipitation during the adjustment is the integrated specific humidity difference between the initial value and the final saturated value from the cloud base to the cloud top, and the condensation heating increases the air temperature.

In a sense, the scheme is not a representation of subgrid-scale convection, but rather an adjustment to neutral stability in an explicitly simulated cloud. For large-scale model grids, the scheme is slow to respond to large-scale forcing as the air must first become saturated on the grid scale and because the rate of ascent is limited by the model's explicit vertical velocity, which is also limited by the grid scale. As a result, significant instability can accumulate during the time it takes for an explicit cloud to form. Another problem with convective adjustment is that the tropical atmosphere can become too moist.

An earlier moist convective adjustment scheme was developed by Manabe *et al.* (1965) and Kurihara (1973). A different type of adjustment scheme was introduced by Betts (1986). The idea is to relax the temperature and mixing ration profiles back to reference profiles over the depth of layers that are unstable to convection. The reference profiles, T_{ref} and q_{ref}, depend on the cloud top and are different for deep and shallow convection. The reference profiles for shallow convection are constructed from a mixing line along which θ_e and q change in proportion to each other, subject to an energy constraint and no latent heat release, while for deep convection, they are constructed empirically on the basis of observational data.

Emanuel (1994) points out that the Betts-Miller scheme has a great advantage over the Kuo-type schemes and moist adjustment schemes in that it contains no artificial constraints on the release of instability. As in nature, convection occurs when and where the atmosphere is unstable and the convection drives the atmosphere back to neutral stage. A weakness of the scheme is that there is no physical basis for a universal reference profile of relative humidity.

Arakawa and Schubert (1974) introduced a cumulus parameterization scheme based on the idea of quasi-equilibrium, which maintains that the collective effect of clouds is to remove the conditional instability of the large-scale flow at the rate that it is produced. The quasi-equilibrium hypothesis assumes that the characteristic time scale for the large-scale flow is much larger than the time scale for convective clouds. In their scheme, cumulus clouds are represented by a spectrum of steady entraining plumes , each plume having a different, but constant entrainment rate.The model "clouds" all

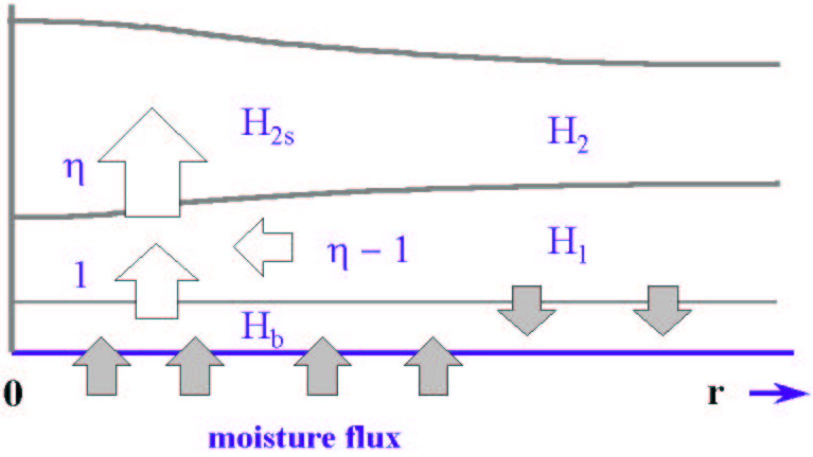

Figure 5. Flow configurations in Ooyama's problem. The moist static energy of air in the lower and upper troposphere and the surface boundary layer are H_1, H_2 and H_b, respectively, and H_2s denotes the saturated moist static energy of the upper layer. For each unit mass of air that exits the boundary layer, in a convective updraught, $\eta - 1$ units are entrained into the updraught and η units are deposited in the upper layer. (From Smith 2000)

have the same base, whereas the top of each cloud is determined by its level of neutral buoyancy, which decreases with increasing entrainment rate.

Rosenthal (1979) pointed out that the validity of using the Arakawa-Schubert scheme in a tropical cyclone model is far from clear, because the 'large scale flow' is not the synoptic scale, but rather the mesoscale. Accordingly, the separation between large-scale and convective time scales that leads to closure is weakened and probably invalidated. A further difficulty is the assumption that the fractional area of convection in a grid area is small compared with unity, which is generally not satisfied in a tropical cyclone model, especially in the eyewall region. These objections apply also to many of the schemes in use. More recent versions of the scheme as well as the concept of quasi-equilibrium are discussed by Randall *et al.* (1997a,b).

1.5 Simple tropical cyclone models

An important step in understanding any physical process is to isolate the processes from those that are less important. To understand tropical cyclone intensification, many simple models have been used for this purpose. Noteworthy examples of such models include the axisymmetric steady-state model of Emanuel (1986) and the axisymmetric time-dependent models of Ooyama (1969), DeMaria and Pickle (1988) which is based on Ooyama 1969's scheme and Emanuel (1989, 1995a). The last two models by Emanuel include new representations of moist convection, which reflect recent advances in our understanding of convective processes (see e.g. Smith, 2000).

Ooyama's 1969 model assumes that the large-scale hydrodynamical aspects of a tropical cyclone may be represented by an axisymmetric, quasi-balanced vortex in a stably stratified incompressible fluid, while the effects of moist convection may be formulated through the first law of the thermodynamics applied to an implicit model of penetrating convective clouds. The basic flow configuration has two layers of homogeneous fluid of different densities overlaying a shallow boundary layer of uniform thickness and having the same density as the layer above. The heating effects of deep cumulus clouds is represented in terms of a mass flux from the boundary layer into the upper layer wherever there is resolved-scale boundary-layer convergence (see Fig. 5). The representation is based on the idea that the deep cumulus clouds that form in such a region will entrain ambient air from the middle layer as they rise through this layer and detrain into the upper layer. It is assumed that for each unit of mass transferred from the boundary layer into the upper layer, $\eta - 1$ units of mass are entrained from the middle layer and transferred to the upper layer also. The entrainment rate is determined according to the conservation of moist static energy, which assumes that the air detrained into the upper layer is neutrally buoyant. The entrainment is a crucial factor in Ooyama's model as it leads to convergence in the middle layer which is required for vortex spin-up. In the regions of boundary-layer divergence, subsidence transfers mass and momentum from upper layer to the lower layer.

A major limitation of Ooyama's model is that it consists of three layers of homogeneous fluid and includes no explicit thermodynamic equation. As a result there is no direct diabatic heating and drying in regions of subsidence between layers by mass transfer. The entrainment rate is the only link between thermodynamics and dynamics. Angular momentum is transported vertically between the middle layer and upper layer by the convective mass flux, but there is no such transfer between the boundary layer and the middle layer because the radial profile of tangential velocity in these two layers is taken to be the same. As pointed by Emanuel (1989), the condition of convergence for the convection is quite artificial because the convection can't happen in the divergence region. The convective mass flux constructed in Ooyama (1969) is a special way to represent the vertical transfer in the shallow water model where the vertical velocity is not explicitly calculated.

All previous parameterization schemes are formulated for upright convection. Observations show a marked outward slope of the eye-wall convection in mature tropical cyclones (see e.g. Jorgensen, 1984) and at least in this region the convection is more "slantwise" than upright. To take account of this fact, Emanuel (1995a) formulated a tropical cyclone model in potential radius coordinates* in which the surfaces of absolute angular momentum are upright.

[*] proportional to the square root of the absolute angular momentum.

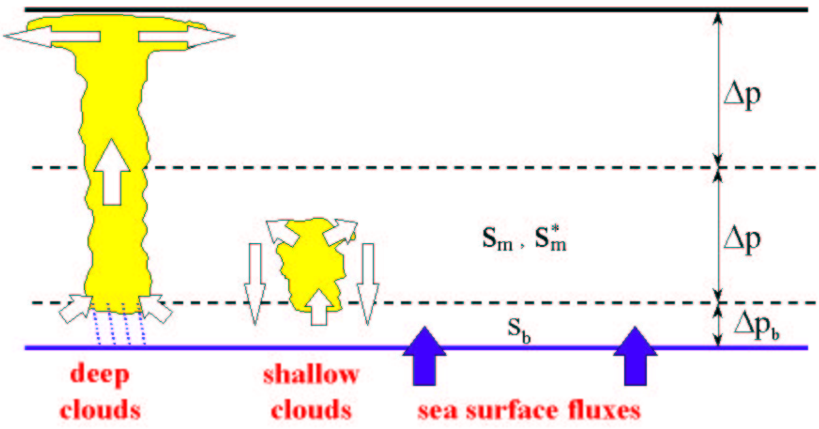

Figure 6. Vertical structure of the tropical cyclone model formulated by Emanuel (1995a). (from Smith, 2000)

For the idealized axisymmetric steady-state tropical cyclone model which is formulated by Emanuel, diabatic processes are represented by equating the saturated moist entropy of the free troposphere, defined assuming a reversible process, to the moist entropy of the subcloud layer along an angular momentum surface. In essence, cumulus convection is assumed to redistribute heat acquired from the sea surface so as to keep the environment locally neutral to slantwise moist convection, in the spirit of the quasi-equilibrium hypothesis.

Emanuel's 1995 model uses a convection scheme based on the concept of boundary-layer quasi-equilibrium (see Raymond, 1995). The basic configuration is shown in Fig.6. A convective mass flux, M_{ueq} is calculated on the assumption that there is an exact balance between the surface entropy flux from the ocean and the downward flux of low entropy air through the top of the boundary layer, neglecting the radiative cooling of the boundary layer. Unlike the Emanuel 1989's scheme, in Emanuel 1995's model , shallow clouds are not considered explicitly, but the moistening effects of convection are included by prescribing the detrainment of entropy in the lower troposphere as a function of the relative humidity in the middle layer. One disadvantage of Emanuel 1995's scheme is that there is no physical basis to determine the amount of detrainment of entropy into the lower troposphere, which has an effect on the moistening of lower troposphere and the rapid intensification of the vortex . The model behaviour using this scheme is very similar to that described by Emanuel (1989). In particular, the near saturation of a mesoscale column of the troposphere in the cyclone core is a prerequisite for intensification. Other limitations of Emanuel's models are the assumption of moist neutrality outside the convective region and the absence of an explicit water cycle.

The use of potential-radius coordinates in Emanuel's models provides higher resolution in the vortex core and facilitates the parameterization of slantwise convection, including the angular momentum transport. However, the use of these coordinates complicates the generalization of the models to three dimensions. Moreover, in reality the convection may not be exactly along angular momentum surfaces; if the convection is not neutral but releases CAPE, the sloping updraughts will have a component towards lower absolute angular momentum.

1.6 Motivation

Forecasting tropical cyclone intensity change is a difficult and challenging problem in tropical cylone research. There is an urgent need to improve such forecasts. Because of the recognized importance of moist convection in tropical cyclone dynamics, it is possible that any major improvement in intensity forecasts will depend on improvements in the representation of convection in tropical cyclone models. Therefore such improvements will require a better understanding of convection in tropical cyclones. Numerical models of tropical cyclones are the main tools to enhance our understanding of tropical cyclone dynamics. Even though now the computer power is able to carry out calculations of the complex models with a relatively high horizontal and vertical resolution and sophisticated representations of physical processes, there remains a role for simple models, the results from which are usually easier to interpret than those from models with complex representations of physical processes. Much insight into tropical cyclone behaviour has emerged from simple models, such as the three-layer axisymmetric model of Ooyama (1969), the axisymmetric models of Emanuel (1989, 1995a), and the three-layer, three-dimensional model of Anthes *et al.* (1971a,b) and Anthes (1972) are the good examples .

The aim of the present work is to develop a minimal three-dimensional tropical-cyclone model with a fully-integrated representation of moist physics that is suitable for basic studies of tropical-cyclone behaviour. The benefits of such a model are that it may be simple enough to provide insights into some aspects of the complex interactions that occur between moist convection and the larger-scale vortex circulation in a variety of situations.

This model has certain advantages compared with the models of Ooyama (1969) and Emanuel (1995a). In Ooyama 's 1969 model the rate of latent heat release is not equal to the rate at which potential energy (generated by the mass transfer between layers) is converted to kinetic energy (see Ooyama, 1969, P25). Also deep convection can't happen in the region where there is divergence in the boundary layer even if there is large convective instability. Emanuel's 1995 scheme is designed for an axisymmetric model formulated in potential radius coordinates. The generalization of the scheme to three dimensions requires substantial modification as potential radius is then inconvenient to use and its avoidance necessitates the introduction of an outflow layer. In his scheme, there is no way to calculate the precipitation from the entropy budget, and the detrainment of entropy in the middle and top layers is determined by artificial parameters. The three-dimensional model described here includes an integrated representation of moist processes with both a moisture and a thermodynamic equation, thereby avoiding the limitations of the Ooyama and Emanuel schemes.

Three different convection schemes are compared in the model to determine whether important features of cyclone evolution are sensitive to the use of a particular scheme. These schemes are based on the formulation suggested by Arakawa (1969). The case in which moist processes are represented only on the resolvable scale is examined also. The convection schemes differ only in the closure used to determine the cloud-base mass flux and they are essentially modifications of the schemes used by Arakawa (1969) , Ooyama (1969) and Emanuel (1995a). Modifications of the Arakawa and Ooyama schemes reflect the inclusion of precipitation-cooled downdrafts, while more major modifications of Emanuel's scheme are called for because of our use of Cartesian coordinates rather than potential radius coordinates.

In the next chapter, I describe the model and in chapter 3 the cumulus parameterization schemes. The control experiment is detailed in Chapter 4, in which the calculations with three different convection schemes and the one with only explicit moist process are examined. A paper based on chapters 2, 3 and 4 has been published by Zhu *et al.* (2001). In chapter 5, I explore the role of three physical processes on tropical cyclone intensification, namely shallow convection, precipitation-cooled downdrafts and cumulus momentum transport. The results of this chapter are published in the paper by Zhu and Smith (2002). The sensitivity of the model to various parameters is studied in chapter 6 with a view to further understanding the model and its limitations. Calculations of vortex evolution and vortex structure in the minimal hurricane model using the CP-grid and L-grid are compared in the chapter 7. Chapter 8 follows with a critical appraisal of the model. A summary and the conclusions are given in chapter 9.

Chapter 2. Description of the model

2.1 Governing equations

The model is based on the three-dimensional hydrostatic primitive equations in sigma-coordinates (x, y, σ) on an f-plane or β-plane, where x and y are in the zonal and meridional directions, respectively, and

$$\sigma = \frac{p - p_{top}}{p_s - p_{top}} = \frac{p - p_{top}}{p^*}, \tag{3}$$

$p^* = p_s - p_{top}$, p_s and p_{top} are the surface and top pressures and p_{top} is a constant, taken here to be 100 mb. Then the upper and lower boundary conditions require that $\dot{\sigma} = 0$ at $\sigma = 0$ and $\sigma = 1$, where $\dot{\sigma} = D\sigma/Dt$ is the 'vertical' σ-velocity and D/Dt is the material derivative. The zonal and meridional momentum equations and the hydrostatic equation are:

$$\begin{aligned}\frac{\partial u}{\partial t} = &- \left(u\frac{\partial u}{\partial x} + v\frac{\partial u}{\partial y} \right) - \dot{\sigma}\frac{\partial u}{\partial \sigma} + fv - \\ &\frac{R\theta\sigma(p^*\sigma + p_{top})^{\kappa-1}}{p_o^\kappa}\frac{\partial p^*}{\partial x} - \frac{\partial \Phi}{\partial x} + D_u\end{aligned} \tag{4}$$

$$\begin{aligned}\frac{\partial v}{\partial t} = &- \left(u\frac{\partial v}{\partial x} + v\frac{\partial v}{\partial y} \right) - \dot{\sigma}\frac{\partial v}{\partial \sigma} - fu - \\ &\frac{R\theta\sigma(p^*\sigma + p_{top})^{\kappa-1}}{p_o^\kappa}\frac{\partial p^*}{\partial y} - \frac{\partial \Phi}{\partial y} + D_v\end{aligned} \tag{5}$$

$$\frac{\partial \Phi}{\partial \sigma} = -\frac{Rp^*(p^*\sigma + p_{top})^{\kappa-1}}{p_o^\kappa}\theta, \tag{6}$$

where u and v are the velocity components in the x- and y-directions, $f = f_o + \beta y$ is the Coriolis parameter, f_o and $\beta = df/dy$ are constants, R is the specific gas constant for dry air, $\kappa = R/c_p$, c_p is the specific heat of dry air, θ is the potential temperature, Φ is the geopotential, D_u and D_v represent the frictional drag in the x- and y- directions, respectively (see section 2.4), and $p_o = 1000$ mb. In this paper, the calculations are carried out on an f-plane at 20°N. The surface pressure tendency equation, derived from the continuity equation * and boundary conditions is

$$\frac{\partial p^*}{\partial t} = -\int_0^1 \left(\frac{\partial (p^* u)}{\partial x} + \frac{\partial (p^* v)}{\partial y} \right) d\sigma \tag{7}$$

---

* In σ-coordinates, the continuity equation takes the differential form: $\frac{\partial p^*}{\partial t} + \frac{\partial (p^* u)}{\partial x} + \frac{\partial (p^* v)}{\partial y} + \frac{\partial (p^* \dot{\sigma})}{\partial \sigma} = 0$

and $\dot{\sigma}$ is given by

$$\dot{\sigma} = -\frac{1}{p^*}\int_0^\sigma \left(\frac{\partial(p^*u)}{\partial x} + \frac{\partial(p^*v)}{\partial y}\right) d\sigma + \frac{\sigma}{p^*}\int_0^1 \left(\frac{\partial(p^*u)}{\partial x} + \frac{\partial(p^*v)}{\partial y}\right) d\sigma \tag{8}$$

The thermodynamic and moisture equations are

$$\frac{\partial\theta}{\partial t} = -\left(u\frac{\partial\theta}{\partial x} + v\frac{\partial\theta}{\partial y}\right) - \dot{\sigma}\frac{\partial\theta}{\partial\sigma} + Q_\theta \tag{9}$$

and

$$\frac{\partial q}{\partial t} = -\left(u\frac{\partial q}{\partial x} + v\frac{\partial q}{\partial y}\right) - \dot{\sigma}\frac{\partial q}{\partial\sigma} + Q_q \tag{10}$$

where q is the specific humidity, Q_θ is the diabatic heat source and Q_q is the moisture source, the last two of which include contributions from surface fluxes (Chapter 2.4) and deep cumulus convection (section 3.2). The temperature T is related to θ by

$$T = \left(\frac{p}{p_o}\right)^\kappa \theta = \frac{(p^*\sigma + p_{top})^\kappa}{p_o^\kappa}\theta. \tag{11}$$

2.2 Explicit moist processes

Explicit condensation is treated in a similar way to Baik *et al.* (1990a), but the procedure is simpler here because of the coarser vertical resolution used. If at any time the air becomes supersaturated at a grid point, the specific humidity is set equal to the saturation specific humidity and the excess water vapour is condensed to liquid water. This water is assumed to precipitate out while the latent heat released is added to the air. The latent heat raises the air temperature and thereby the saturation specific humidity, requiring a further adjustment of the amount of condensed water, and so on. Accordingly, it is necessary to iterate to determine the final amount of condensed water and latent heat release, but the number of iterations required is small. Like Baik *et al.* (1990a), we apply this explicit procedure before the subgrid-scale convection scheme.

2.3 Radiative cooling

A Newtonian cooling term, $-(\theta - \theta_{ref})/\tau_R$, is added to the right-hand-side of the thermodynamic equation to crudely represent the effect of radiative cooling. In this expression θ_{ref} is the initial potential temperature profile of the basic state and τ_R is a radiative time scale. Following Emanuel (1989; see p3436) we take τ_R to be 12 h.

2.4 Surface turbulent fluxes

The turbulent flux of momentum to the sea surface and the fluxes of sensible heat and water vapour at the surface are represented by bulk aerodynamic formulae in the form

$$\begin{aligned}(F_u, F_v) &= -\rho C_d \left|\mathbf{u_b}\right| (u_b, v_b) \\ F_q &= \rho C_h \left|\mathbf{u_b}\right| (q_s^* - q_b) \\ F_{SH} &= \rho c_p C_h \left|\mathbf{u_b}\right| (T_s - T_b), \end{aligned} \tag{12}$$

where the subscript "b" denotes the value at the middle of the boundary, $\mathbf{u_b} = (u_b, v_b)$, T_s and q_s^* are the sea surface temperature and saturated specific humidity at this temperature, respectively; ρ is the near-surface air density; C_D is the surface drag coefficient; and C_h is the bulk transfer coefficient for heat and moisture. The quantity q_s^* depends also on the sea surface pressure. Here we set ρ equal to the mean density of the lower layer, ρ_b, and assume that $C_h = C_D$, with C_D calculated from the formula used by Shapiro (1992):

$$C_D = (1.024 + 0.05366 R_F \left|\mathbf{u_b}\right|) \times 10^{-3}, \tag{13}$$

where $R_F = 0.8$ is used to reduce the boundary layer wind, $\mathbf{u_b}$ to the 10-m level. The assumption that $C_D = C_h$ is simply expedient in view of the current lack of knowledge on how these quantities are related in high wind speeds. Emanuel (1995b) presents circumstantial evidence to suggest that the ratio C_D/C_h lies in the range 0.75 - 1.5. The sensitivity of our calculations to this ratio are included in a sensitivity study in section 6.2.

The frictional drag terms D_u and D_v in Eqs. (4) and (5) are obtained by dividing the corresponding terms F_u and F_v in Eq. (12) by the depth z_b and the density ρ_b of the lower layer. Similarly the contributions to the source terms Q_θ and Q_q in Eqs. (9) and (10) from the terms F_{SH} and F_q in Eqs. (12) are given by the relations: $Q_\theta = F_{SH}/(\rho_b c_p \pi_s z_b)$ and $Q_q = F_q/\rho_b z_b$, where $\pi_s = (p_s/p_o)^\kappa$ is the Exner function at the surface.

2.5 Boundary and initial conditions

The calculations are carried out in a zonal channel with rigid walls at $y = \pm Y$ and periodic boundary conditions at $x = \pm X$. It is assumed that there is no motion normal to the meridional boundaries (i. e. $v = 0$ at $y = \pm Y$) and that meridional gradients are zero at these boundaries (i. e. $\partial(u, \theta, q)/\partial y = 0$ at $y = \pm Y$). Surface pressure and geopotential are adjusted geostrophically to satisfy the equation

$$\frac{\sigma}{\rho}\frac{\partial p_s}{\partial y} + \frac{\partial \Phi}{\partial y} = -fu. \tag{14}$$

The initial axisymmetric vortex is barotropic and has the same tangential velocity distribution as that used by Smith *et al.* (1990) given by

$$v(r') = \frac{av_m\, r'\,(1 + br'^4)}{(1 + cr'^2 + dr'^6)^2}, \tag{15}$$

where $r' = r/r_m$, r is the radius from the vortex centre, r_m is the radius of maximum tangential wind speed, v_m, and a, b, c and d constants ($a = 1.78803$, $b = 4.74736 \times 10^{-3}$, $c = 0.339806$, $d = 5.37727 \times 10^{-4}$). Here we choose $v_m = 15\ ms^{-1}$, and $r_m = 120$ km. The computational domain size is 4000 × 4000 km^2 and the grid space is 20 km.

The initial mass and geopotential fields are obtained by solving the inverse balance equation, which takes the form (Kurihara and Bender 1980),

$$\nabla^2\Phi + \nabla(\frac{RT\sigma}{p}\nabla p^*) = 2J_{u,v} + f\zeta - \beta u, \tag{16}$$

where J is the Jacobian operator. The temperature is obtained from the hydrostatic equation (6). At $\sigma = 1$, where $\Phi_s = 0$, the equation can be written as

$$\nabla(RT_s\nabla lnp_s) = 2J(u_s, v_s) + f\zeta_s - \beta u_s, \tag{17}$$

where the subscript 's' denotes the surface value of the relevant quantity. This equation can be solved for the surface pressure field if the surface temperature is known.

The far-field temperature and humidity structure are based on the mean West Indies sounding for the hurricane season (Jordan 1957), but the near surface specific humidity has been reduced slightly so that the sounding is marginally stable to deep convection initially (see Appendix A). The environment surface pressure is 1015 mb, and the minimum surface pressure at the vortex centre is initially 1008 mb. Horizontal variations of specific humidity in the presence of the initial vortex are neglected. The sea surface temperature is taken to be 28°C.

2.6 Subgrid-scale diffusion

To filter out the energy in high frequency waves, a fourth-order horizontal diffusion term $D_4 = -k_1\nabla_h^4\chi$ is added to all prognostic equations with a diffusion coefficient $k_1 = 0.0008\Delta^4$, where ∇_h is the horizontal Laplacian operator and Δ is the horizontal grid spacing. At the boundaries, a second-order diffusion term $D_2 = k_2\nabla_h^2\chi$ is applied

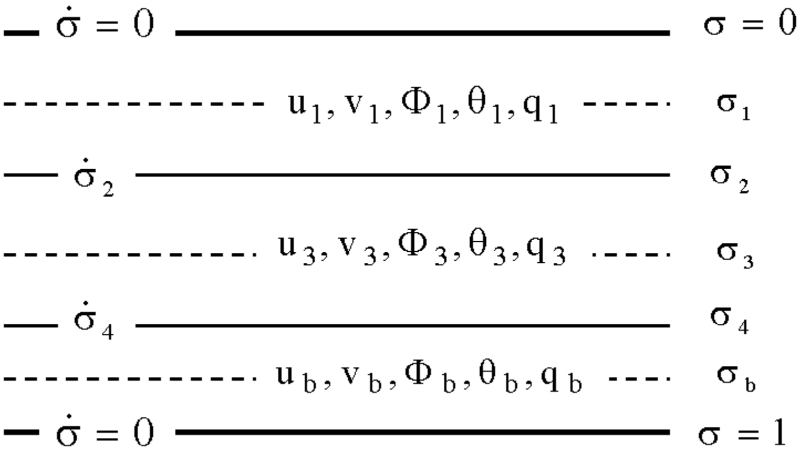

Figure 7. Configuration of σ-levels in the model showing locations where the dependent variables are stored. The horizontal velocity components, geopotential, potential temperature, specific humidity and the moist static energy used in the convection scheme (see Chapter 3) are calculated at levels-1, -3 and -b and the vertical velocity $\dot{\sigma}$ and convective mass flux are stored at levels-2 and -4.

with $k_2 = 0.0008\Delta^2$. The philosophy of such an approach is discussed by Pielke (1984; see section 10.6).

2.7 The numerical method

The model is divided vertically into three unequally deep layers with boundaries at $\sigma = 0$, σ_2, σ_4 and $\sigma = 1$ (see Fig. 7). All the dependent variables, such as horizontal velocity, potential temperature, specific humidity and geopotential, are defined in the middle of each layer ($\sigma = \sigma_1$, σ_3, and σ_b), and $\dot{\sigma}$ is staggered, i.e. it is defined at the boundaries between layers. This is the so-called Lorenz-grid (L-grid). The advantage with the L-grid model is that the total energy is conserved, and also the mean potential temperature and the variance of the potential temperature are conserved under adiabatic and frictionless processes (Arakawa and Suarez, 1983). The equations are expressed in finite-difference form in both the horizontal and vertical and integrated forward in time using the Adams-Bashforth third-order method.

The initial pressure, temperature, specific humidity and geopotential height in the middle of each layer and at the boundaries between layers are detailed in Appendix A.

Chapter 3. Cumulus parameterization schemes

There are three different options in the model for representing subgrid-scale deep cumulus convection. The first is a modified version of the scheme proposed by Arakawa (1969). In its original form, the scheme is similar to that proposed by Ooyama (1969), but is more general because the thermodynamic equation is included directly in the formulation, whereas in Ooyama's model the dynamics and thermodynamics are coupled only through the specification of the mass transfer between layers. The modified form of Arakawa's scheme described here includes the effects of precipitation-cooled downdrafts. The second scheme is based on the boundary-layer quasi-equilibrium scheme used by Emanuel (1995a), but differs from the original Emanuel scheme in certain important details as described in subsection 3.5 below. The third scheme, like Ooyama's scheme, assumes that the (net) cloud-base mass flux is proportional to the resolved-scale vertical velocity at the top of the boundary layer, but it includes also the effects of precipitation-cooled downdrafts. In fact, the only difference between the three schemes as implemented here lies in the closure assumption that determines the cloud-base mass flux.

3.1 The cloud model

The exchange of mass between a deep convective cloud and its environment within a grid column, and the exchange between adjacent grid columns is shown schematically in Fig. 8, again for the case of two-dimensional flow in the $x - \sigma$ plane. For the purpose of illustration only, all the mass exchange between adjacent grid cells is taken to occur through the boundary on the right of the grid column ($x = \Delta x$) and I consider the case in which the dependent variables are horizontally staggered with u_n stored on the boundary and other variables in the middle of a grid cell. In the present model, where the variables are not horizontally staggered, the configuration shown would apply to two adjacent grid columns. The subgrid-scale vertical transports are formulated by considering the cloudy and clear-air regions of the grid column separately. The subgrid-scale fluctuations in the dependent variables are associated with different (uniform) values of these quantities in these regions. *Deep convection is assumed to occur in a grid column if the moist static energy in the boundary layer h_b exceeds the saturation moist static energies in the upper and lower troposphere*, h_1^* and h_3^* (Henceforth, a star denotes the saturation value of a thermodynamic variable). The resolved-scale averaged mass fluxes $\overline{M}_n$ at levels-2 and -4 are assumed to be positive, and the negative sign

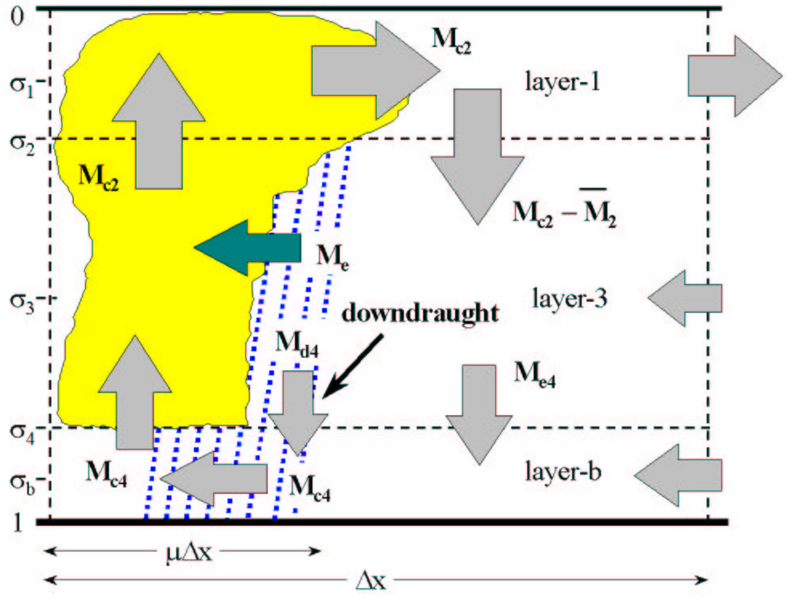

Figure 8. Schematic diagram of the vertical circulation within a grid column in the cumulus parameterization schemes used in this paper. The schemes are based on a steady state bulk cloud model which is assumed to occupy a small fraction μ of the grid box. The cloud takes mass from the boundary layer at a rate M_{c4} and detrains it to the upper layer at a rate M_{c2}. Entrainment of middle-layer air into the cloud takes place along the way at a rate M_e, just sufficient to ensure that the air detrains from the cloud at the same temperature as the environment at level-1 (i.e. detrainment of cloud air occurs at its level of neutral buoyancy). The downdraft mass flux M_{d4} is assumed to be proportional to M_{c4} and the downdraft is considered to be a part of the cloud environment. The resolved-scale flow in or out of the grid box is indicated in the diagram by arrows through the right boundary. The resolved- scale vertical mass fluxes are denoted by $\overline{M}_n$ (n = 2, 4) and the clear air mass flux at level-4 is denoted by M_{e4} (by clear air I mean the part of the cloud environment where there is no precipitation). If $\overline{M}_n$ is less than the *net* mass flux, $M_{cn} - M_{dn}$, associated with convection at a particular level, there is subsidence in the clear air (e.g. $M_{e4} > 0$) which warms and dries the cloud environment in the layer below.

represents ascending motion.

As in Arakawa and Ooyama's formulation, the three schemes described here are based upon a steady-state bulk cloud model, indicated by the cloud on the left of the diagram in Fig. 8. In the cloud model, M_{c4} is the cloud-base mass flux from the boundary layer to the middle layer, M_e is mass flux entrained into the cloud from the middle layer, and M_{c2} is the mass flux transferred from the middle layer to the upper layer inside the cloud (here a subscript 'c' denotes a cloud property). Continuity of mass requires that

$$M_{c2} = M_{c4} + M_e. \qquad (18)$$

Following Ooyama (1969) we assume that air which detrains from the cloud into layer-1 has zero buoyancy so that, although it is saturated, its temperature is the same as that of the environment in layer-1. Then

$$M_{c2}h_{c1} = M_{c4}h_b + M_e h_3. \tag{19}$$

where $h_{c1} = h_1^*$ is the saturation moist static energy of cloudy air in layer-1. As shown below, Eq. (19) determines the mass flux entrained into the cloud.

Combining (18) and (19), and writing

$$M_{c2} = \eta M_{c4}, \tag{20}$$

we obtain

$$\eta = 1 + \frac{h_b - h_1^*}{h_1^* - h_3} \tag{21}$$

and it follows using Eq. (18) that

$$M_e = (\eta - 1)M_{c4} \tag{22}$$

Note that the condition for deep convection $(h_b > h_1^*)$ ensures that the entrainment mass flux given by Eq. (22) is positive, provided that $h_1^* > h_3$; i.e. the atmosphere is stable with respect to middle-level convection. This condition is always satisfied in the present calculations.

It is assumed that precipitation falls into the cloud environment in layer-3 and that a precipitation-cooled downdraft brings air with the moist static energy of that layer into the boundary layer. Let M_{d4} be the downdraft mass flux from the middle layer to the boundary layer. Following Emanuel (1995a) we take the downdraft mass flux proportional to the updraft mass flux, i.e.

$$M_{d4} = \chi M_{c4}, \tag{23}$$

where the quantity χ is linked to the precipitation efficiency ε through the expression $\chi = 1 - \varepsilon$. Emanuel (1995a) relates ε to the relative humidity of the middle layer in a way that downdrafts are stronger when the middle layer is relatively dry and weaker when it is relatively moist. For a similar reason we define $\varepsilon = q_3/q_3^*$, where q_3^* is the saturation specific humidity in layer-3. Note that $0 \leq \chi \leq 1$.

Since the grid-averaged vertical velocity at each level is the sum of the average cloud and cloud environment mass fluxes within the grid box, the mass fluxes at levels-2 and -4 in the cloud environment are $M_{c2} - \overline{M}_2$ and $M_{c4} - \overline{M}_4$, respectively. The latter may be subdivided into an amount M_{d4} that occurs in precipitation and an amount $M_{e4} = M_{c4} - M_{d4} - \overline{M}_4$ that occurs in clear air (see Fig.8). Then, in the cloud-free environment in unit time, $M_{c2}h_{c1}$ units of h are detrained from the cloud to layer-1 and $(M_{c2} - \overline{M}_2)h_2$ units are transferred from this layer to layer-3 by the return circulation associated with the clouds. Altogether, $(M_{e4}h_4 + M_{d4}h_3)$ units of h are transferred from the middle layer to the boundary layer, partly as subsidence in precipitation-free air (the first term in this expression) and partly in precipitation-cooled downdrafts (the second term). Note that *(saturated) downdrafts in our model have a larger effect on the boundary layer moist static energy budget per unit mass transferred than subsidence in precipitation-free air. This is because the origin of downdraft air is higher and the moist static energy is lower.* In this respect, the formulation is different from that of Emanuel's (1989, 1995a), in which the moist entropy of downdraft air and subsiding clear air are the same. It is important to note that, while in many circumstances the precipitation-free, intra-cloud air will be subsiding (i.e. $M_{e4} > 0$), this does not have to be the case and I will show that regions of ascent may and do occur (i.e. $M_{e4} < 0$).

3.2 Subgrid-scale heat and moisture sources

The six equations governing the convection scheme consist of prognostic equations for the dry static energy, s $(= c_pT + \Phi)$, and q in each layer. Then the moist static energy, $h = s + Lq$. The formulation of the equations is essentially the same as that given by Arakawa (1969) and reproduced in the book by Haltiner (1971; see section 10.4), although both authors focus on the closure for middle-level convection, the conditions for which are never met in our model. The basis of the derivation is sketched briefly in Appendix C. The assumption that the fractional coverage of convective cloud, μ, in a grid column is small compared with unity enables the grid-averaged changes of these quantities to be approximated with the changes that occur in the cloud environment. Because the grid-scale and subgrid-scale vertical mass fluxes at any level are not independent (see section 3.1 above), the formulation of the source terms and vertical advection terms in Eqs. 9 and 10 need to be considered together wherever deep convection is called for in a grid column. Application of the volume-averaged conservation equation derived in Appendix C and the assumption that the cloud-environment mean of q and s is approximately equal to the mean over the entire grid cell leads to the following equations the rates-of-change of q and s in the top, middle, and boundary layer as a result of subgrid-scale fluxes:

$$\alpha_1 p^* \frac{\partial q_1}{\partial t} = M_{c2}\left(q_{c1} - q_1\right) - \left(M_{c2} - \overline{M}_2\right)\left(q_2 - q_1\right), \tag{24}$$

$$\alpha_3 p^* \frac{\partial q_3}{\partial t} = \left(M_{c2} - \overline{M}_2\right)\left(q_2 - q_3\right) - M_{d4}\left(q_{d4} - q_3\right) - \left(M_{c4} - M_{d4} - \overline{M}_4\right)\left(q_4 - q_3\right), \tag{25}$$

$$\alpha_b p^* \frac{\partial q_b}{\partial t} = M_{d4}\left(q_{d4} - q_b\right) + \left(M_{c4} - M_{d4} - \overline{M}_4\right)\left(q_4 - q_b\right), \tag{26}$$

$$\alpha_1 p^* \frac{\partial s_1}{\partial t} = -\left(M_{c2} - \overline{M}_2\right)(s_2 - s_1)\,, \tag{27}$$

$$\alpha_3 p^* \frac{\partial s_3}{\partial t} = \left(M_{c2} - \overline{M}_2\right)(s_2 - s_3) - M_{d4}(s_{d4} - s_3) - \left(M_{c4} - M_{d4} - \overline{M}_4\right)(s_4 - s_3)\,, \tag{28}$$

$$\alpha_b p^* \frac{\partial s_b}{\partial t} = M_{d4}(s_{d4} - s_b) + \left(M_{c4} - M_{d4} - \overline{M}_4\right)(s_4 - s_b), \tag{29}$$

where q_{c1} is the specific humidity of cloudy air in layer-1; s_{d4} and q_{d4} are the dry static energy and specific humidity of downdraft air as it crosses level-4; $\alpha_n = \Delta\sigma_n/g$, where $\Delta\sigma_n$, (n = 1, 3, b) are the thicknesses of layers-1, -3 and -b in terms of σ; and s_2, s_4, q_2, q_4 are obtained from values of s and q at adjacent levels by interpolation (the details are explained in Appendix B). We have included the grid-scale vertical fluxes in these equations to emphasize that they determine the *net* vertical motion in the cloud environment, but they, together with the grid-scale horizontal transports, are calculated in Eqs. (9) and (10) and the subgrid-scale increments to q and s are calculated from Eqs. (24) - (29) with the grid-scale vertical mass transports excluded.

The heating contributions from deep convection to Q_θ in Eq. (9) are obtained by calculating the increments in dry static energy, Δs_n, during a time step, using Eqs. (27) - (29) with the terms involving the grid-scale mean quantities $\overline{M}_2$ and $\overline{M}_4$ *excluded.* Then we set $Q_{\theta n} = \Delta s_n/(c_p \pi_n)$, where π_n is the Exner function at the appropriate σ-level (n = 1, 3, b). The moistening contributions Q_q in Eq. (10) are obtained in a similar way using Eqs. (24) - (26). When downdrafts are excluded, Eqs. (24) - (29) are identical to those given by Arakawa (1969).

It remains now to calculate the values of s_{d4}, q_{d4} and M_{c4}. The calculation of s_{d4} and q_{d4} is described in section 3.3 below. A closure assumption is required to determine the cloud-base mass flux, M_{c4}. The three methods explored here are described in section 3.4 – 3.5.

3.3 Downdraft thermodynamics

The calculation of s_{d4} and q_{d4} is indicated schematically in Fig. 9. It is assumed that rain falls into the air in layer-3 and partially evaporates until the air at this level becomes saturated and cooled to the wet- bulb temperature, T_{w3}. Then it is assumed that the cooled air descends into the boundary layer as rain continues to evaporate into it so as to just keep it saturated. The wet-bulb temperature at level-4, T_{w4}, is calculated by solving iteratively the equation

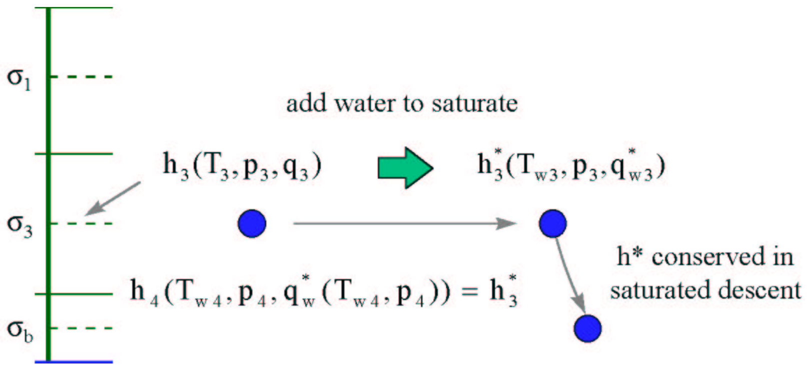
σ1
σ3
σb
add water to saturate
h3(T3,p3,q3)
h*3(Tw3,p3,q*w3)
h* conserved in saturated descent
h4(Tw4,p4,q*w(Tw4,p4)) = h*3

Figure 9. Schematic diagram showing how the downdraft temperature is determined. First, water is added to air parcels at level-3 until they are saturated. This lowers the temperature to the wet-bulb temperature T_{w3}, but increases the specific humidity to q^*_{w3}. It is assumed then that the parcels descend as precipitation continues to evaporate into them to keep them just saturated. The saturation moist static energy is approximately conserved during this descent.

$$c_pT_{w4} + gz_4 + Lq^*(T_{w4}, p_4) = h_3, \tag{30}$$

and the specific humidity at level-4, q_{w4}, is simply equal to $q^*(T_{w4}, p_4)$. Since the moist static energy of an air parcel is approximately conserved when liquid water evaporates into it as well as during saturated descent, downdrafts reduce the moist static energy of the boundary layer. Further, because the moist static energy of downdraft air at level-4 is less than that of precipitation-free air at this level, downdraft air is more effective in decreasing the boundary layer moist static energy than subsidence in precipitation-free air. This representation of downdrafts leads to the coldest boundary-layer temperature that can be achieved by precipitation-cooled subsidence. In reality the evaporation of precipitation is normally insufficient to keep downdrafts saturated, and this diminishes their cooling and moistening effect.

3.4 The modified 1969-Arakawa scheme

The closure for this scheme is obtained by assuming that deep convection tends to reduce the instability on the time, τ_{dc}, and in doing so drives the moist static energy of the upper layer towards that of the boundary layer. Mathematically we write

$$p^*\frac{\partial}{\partial t}(h_b - h_1^*) = -\frac{p^*(h_b - h_1^*)}{\tau_{dc}}. \tag{31}$$

It can be shown that (see e.g. Haltiner, 1971, p189)

$$p^*\frac{\partial}{\partial t}(h_b - h_n^*) \;=\; p^*\frac{\partial}{\partial t}(h_b - (1+\gamma_n)\, s_n), \, (n = 1, 3, b), \tag{32}$$

where

$$\gamma_n = \frac{L}{c_p}\left(\frac{\partial q_n^*}{\partial T}\right)_{T_n} . \tag{33}$$

Then Eq. (31) can be written as

$$\alpha_b p^* \frac{\partial}{\partial t}\left[h_b - (1+\gamma_1)\ s_1\right] = \frac{-\alpha_b p^*(h_b - h_1^*)}{\tau_{dc}}. \tag{34}$$

Since $h_b = s_b + Lq_b$, Eqs. (26), (27) and (29), can be used to eliminate the time derivatives in Eq. (34) and the resulting equation provides an expression for the mass flux M_{c4}:

$$M_{c4} = \frac{-\alpha_b p^*(h_b - h_1^*)/\tau_{dc}}{(\chi h_{db} + (1-\chi)h_4 - h_b - \eta(\alpha_b/\alpha_1)(s_1 - s_2)(1+\gamma_1))}. \tag{35}$$

Following Arakawa, τ_{dc} is set equal to 1 h. This closure on the cloud-base mass flux is essentially the same as that used in the current version of the European Centre for Medium Range Weather Forecasts' Integrated Forecasting System (Gregory *et al.* 2000). Indeed, Eq. (35) is analogous to Eq. (6) of Gregory *et al.* since $(h_b - h_1^*)$ is a measure of the degree of convective instability between the boundary layer and upper layer and is therefore related to the convective available potential energy in our model. Note that both updrafts and downdrafts contribute to the stabilization of their environment as expressed by Eq. (35).

3.5 The modified 1995-Emanuel scheme

An alternative to the Arakawa closure is that implemented by Emanuel (1995a), who made the assumption that the boundary-layer is in quasi-equilibrium (Raymond, 1995). Based on this assumption one can derive a prognostic equation for the saturation moist entropy at the top of the subcloud layer (the subcloud layer is taken to be identical to the boundary layer). Emanuel characterizes the thermal structure of the free troposphere by assuming that the (reversible) saturation moist entropy is constant along an absolute angular momentum surface emanating from the boundary layer, equal to its value at the top of this layer. In other words, the free troposphere is assumed to be slantwise neutral * to moist convection. Emanuel's model is axisymmetric and the implementation of the foregoing assumption is elegantly facilitated by choosing potential radius as radial coordinate. The use of potential radius coordinates obviates the need to explicitly include an outflow layer in the upper troposphere. In the present three-dimensional model, the use of potential radius is impractical. Accordingly we use Emanuel's method to determine the cloud-base mass flux, but Arakawa's formulation to determine the convective heating and moistening. The latter are not treated separately in Emanuel's formulation so that a separate water budget, and for example the precipitation rate, cannot be determined.

---

* Neutral with respect to a *reversible* moist adiabat.

Strict boundary-layer equilibrium would require that the sea surface entropy flux is exactly balanced by the flux of low entropy air brought down into the boundary layer by subsidence in precipitation-free air, by precipitation-cooled downdrafts and by the horizontal advection of entropy. Then, the local rate-of- change of boundary-layer entropy is zero. In our model we assume that the *local* rate-of-change of *moist static energy* in the boundary layer is zero. The total rate-of-change of this quantity is obtained by taking $L\times$ Eq. (26) + Eq. (29) and including the surface flux and horizontal advection terms, whereupon

$$\alpha_b p^* \frac{D_h h_b}{Dt} = (F_{SH} + LF_q) + M_{d4}\,(h_{d4} - h_b) + (M_{c4} - M_{d4} - \overline{M}_4)(h_4 - h_b), \qquad (36)$$

where $D_h/Dt = \partial/\partial t + \mathbf{u_b}\cdot\nabla$ denotes the horizontal part of the material derivative, and $\mathbf{u_b} = (u_b, v_b)$. The equilibrium updraft mass flux, M^*_{c4}, is determined from Eq. (36) by assuming that $\partial h_b/\partial t \equiv 0$, whereupon

$$M^*_{c4} = \frac{(F_{SH} + LF_q) - \alpha_b p^* \boldsymbol{u_b}\cdot\nabla h_b - \overline{M}_4\,(h_4 - h_b)}{h_b - \chi h_{d4} - (1\ - \chi)h_4}. \qquad (37)$$

Following Emanuel *op. cit.*, we assume that the instability associated with the latent and sensible heat fluxes from the sea surface is released over a finite time-scale τ, which is taken here to be the same as τ_{dc}. The actual mass flux M_{c4} is determined by the equation

$$\frac{D_h M_{c4}}{Dt} = \frac{M^*_{c4} - M_{c4}}{\tau_{dc}} \qquad (38)$$

after which M_{c2} is obtained from Eq. (20) and M_e is obtained from Eq. (22). The sensitivity study of the mass flux formulation in the Emanuel scheme is carried out in the section 6.7.

3.6 The modified 1969-Ooyama scheme

We examine also a closure similar to the one used by Ooyama (1969), in which the (net) cloud-base mass flux is equal to the resolved-scale mass flux at the top of the boundary layer, i.e.

$$M_{c4} = -p^*\overline{\dot{\sigma}}_4/[g(1-\chi)]. \qquad (39)$$

A consequence is that there is no subgrid-scale subsidence into the boundary layer except that associated with precipitation-cooled downdrafts (i.e. $M_{e4} \equiv 0$).

Chapter 4. The control experiments

The results of four control experiments are carried out on an f-plane to compare the effects of different parameterization schemes on the vortex evolution. These experiments are listed in Table 2. The results are compared with that of Chapter 5 and 6, in which we analyse the three important physical processes and also carry out the sensitivity studies to the model parameters. All calculations begin with the initial conditions given in section 2.5.

TABLE 2. List of control experiments

Experiment	**Cumulus convection scheme**
1	No convection scheme - grid-scale precipitation only
2	Modified Arakawa scheme
3	Modified Emanuel scheme
4	Modified Ooyama scheme

4.1 Overview of vortex evolution

Figure 10 shows time series of the minimum surface pressure and maximum (total) wind speed in the lowest layer for the four experiments listed in Table 2. In broad terms, the three calculations that include a deep cumulus parameterization scheme show a similar pattern of evolution:

- a gestation period during which the vortex gradually intensifies and the central pressure slowly falls,
- a period of rapid intensification and deepening, and,
- a mature stage in which the intensity fluctuates, possible accompanied by a slow mean increase or decline.

This behaviour is similar to that in other models and the phenomenon of rapid deepening is well known from observations. According to Pielke and Landsea (1998) it occurs during the formation of most typhoons and all Atlantic hurricanes with wind speeds exceeding 50 ms^{-1} (about 20 % of the total). Willoughby (1999) notes that the onset of rapid deepening is currently unpredictable.

As might be expected, the details of vortex evolution vary with the particular parameterization scheme. In the calculation with *only* the explicit release of latent heat,

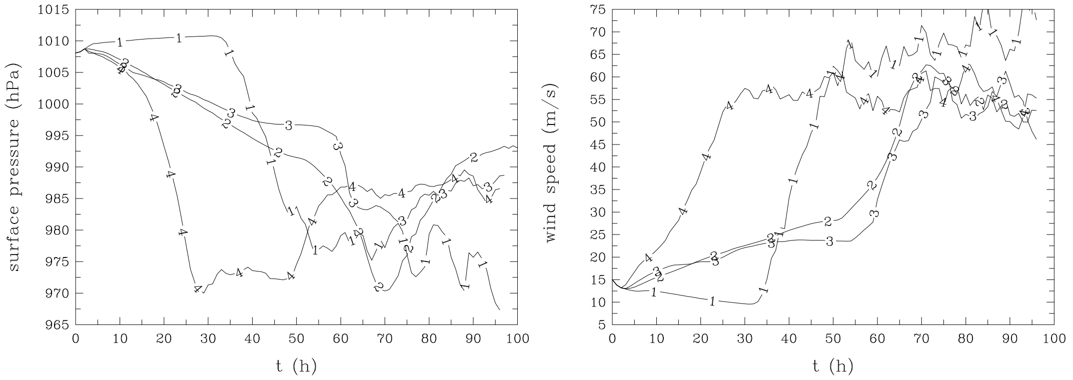

(a)

(b)

Figure 10. Variation of (a) minimum surface pressure in mb, and (b) maximum total wind speed in ms^{-1} in the lowest layer as a function of time. Numbers on curves refer to experiment numbers in the Table 2.

the gestation period is replaced by a period of slow decay associated with frictionally-induced divergence in the lower troposphere (layer-3). The period of rapid deepening coincides with the occurrence of saturation on the grid-scale at level-3. The associated latent heat release creates positive buoyancy in the inner core region. This buoyancy leads to convergence in the lower troposphere, dominating the divergence that would be induced by friction in this region in the absence of significant buoyancy (see e.g. see section 2 of Smith, 2000).

The inclusion of a parameterization scheme for deep cumulus convection leads also to warming and buoyancy-driven convergence in the lower-troposphere. Again this convergence exceeds the frictionally-induced divergence and accounts for the slow intensification during the gestation period. However, it is significant that even in the three calculations with a parameterization of deep convection, the period of rapid deepening coincides with the explicit release of latent heat in the inner core region (see section 4.2 below). At this stage the vertical temperature profile in an annular region surrounding the core rapidly becomes pseudo-moist adiabatic. Then the condition for parameterized deep convection is no longer satisfied so that the parameterized convection shuts off in this region.

A striking difference between the calculations using different convection schemes is the length of the gestation period: with the Ooyama scheme, this period is quite short with rapid intensification occurring after only about half a day, whereas with the Arakawa and Emanuel schemes it occurs about two days later. Perhaps surprisingly, despite the heating produced by parameterized convection, rapid intensification occurs about a day earlier in the case with only explicit moist processes than with the Arakawa or Emanuel parameterization schemes. The reasons for these differences are discussed below. The maximum intensity is similar in all three cases with parameterized convection, but is about 20% smaller than in the calculation with explicit moist processes only, at least for the 96 h duration of the calculations. In all cases the maximum wind speed in the lowest layer exceeds 60 ms^{-1}. Suffice it to say that the maximum tangential wind speed in the boundary layer in the mature stage in Expt. 1 is 60 ms^{-1} and in Expts. 2 - 4 it is about 50 ms^{-1} in each case. These values compare with the value 52 ms^{-1} estimated for the maximum potential intensity using the MPI theory worked out by Emanuel (1995b). In those calculations, we chose the options to exclude the effect of dissipative heating as we do not include this effect in our model, except in the calculation described in section 6.4 and calculate the convective available potential energy of the initial sounding on the assumption of pseudoadiabatic ascent. Emanuel (1995b) formulated the MPI theory to estimate the upper bound on tropical cyclone intensity using sea surface temperature and atmospheric thermodynamic profiles of the initial soundings. The details of this theory is described in Appendix E. The reason why the maximum wind speed is slightly higher in the experiment without a convection parameterization scheme is that the convective mass fluxes reduce the moisture static energy in the boundary layer by transferring the air with lower moist static energy from the middle layer .

4.2 Details of vortex evolution

Many aspects of the vortex evolution can be succinctly illustrated by time-radius plots of selected azimuthally-averaged model quantities.

Figure 11 shows time-radius plots of the tangential and radial wind components, azimuthally averaged about the domain centre at levels-1 and -3, in the calculation with only the explicit release of latent heat. Figure 12 shows similar plots of the perturbation potential temperature (relative to its ambient value) and relative humidity at level-3, as well as the vertical p-velocity * (ω) at level-4 in this calculation. For about 33 h the initial vortex slowly decays and the radius of maximum tangential wind speed steadily increases (Fig. 11a,b) as a result of frictionally-induced radial divergence above the boundary layer (Fig. 11c,d). However, during this period, the specific humidity and relative humidity increase in the boundary layer as a result of the strong surface moisture flux, which increases with wind speed and decreasing surface pressure, and also above the boundary layer in the core region as a result of the vertical advection of moisture by the secondary circulation, i.e. the azimuthal-mean circulation in the vertical plane. After about 30 h the air at level-3 saturates in the core region (Fig. 12b) and the subsequent latent heat release produces a net positive buoyancy that leads to a brief period of strong convergence at level-3 as seen in Fig. 11d. A part of

* $\omega = Dp/Dt = p^{*}\dot{\sigma} + \sigma(\frac{\partial p^{*}}{\partial t} + u\frac{\partial p^{*}}{\partial x} + v\frac{\partial p^{*}}{\partial y})$

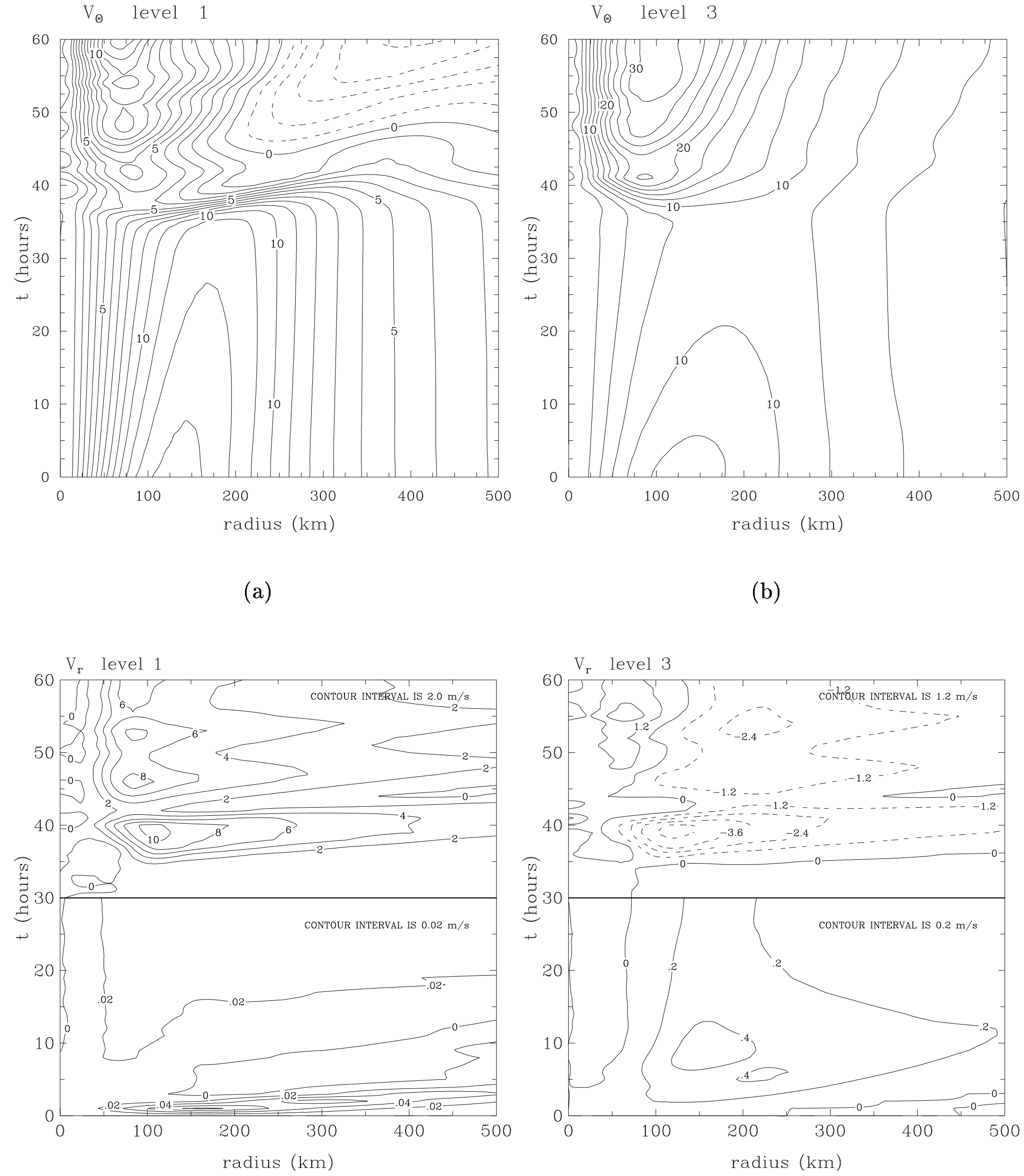

(a) (b)

(c) (d)

Figure 11. Time-radius plots of the tangential (v_θ) and radial (v_r) wind components in ms^{-1}, azimuthally-averaged about the domain centre at levels-1 and -3, in the calculation with only the explicit release of latent heat (Expt. 1). (a) v_θ at the level-1, contour interval is 2 ms^{-1}, (b) v_θ at the level-3, contour interval is 2.5 ms^{-1}, (c) is v_r at level-1, and (d) is v_r at level-3. Dashed lines correspond with negative values. A horizontal line delineates the regions with different contour intervals.

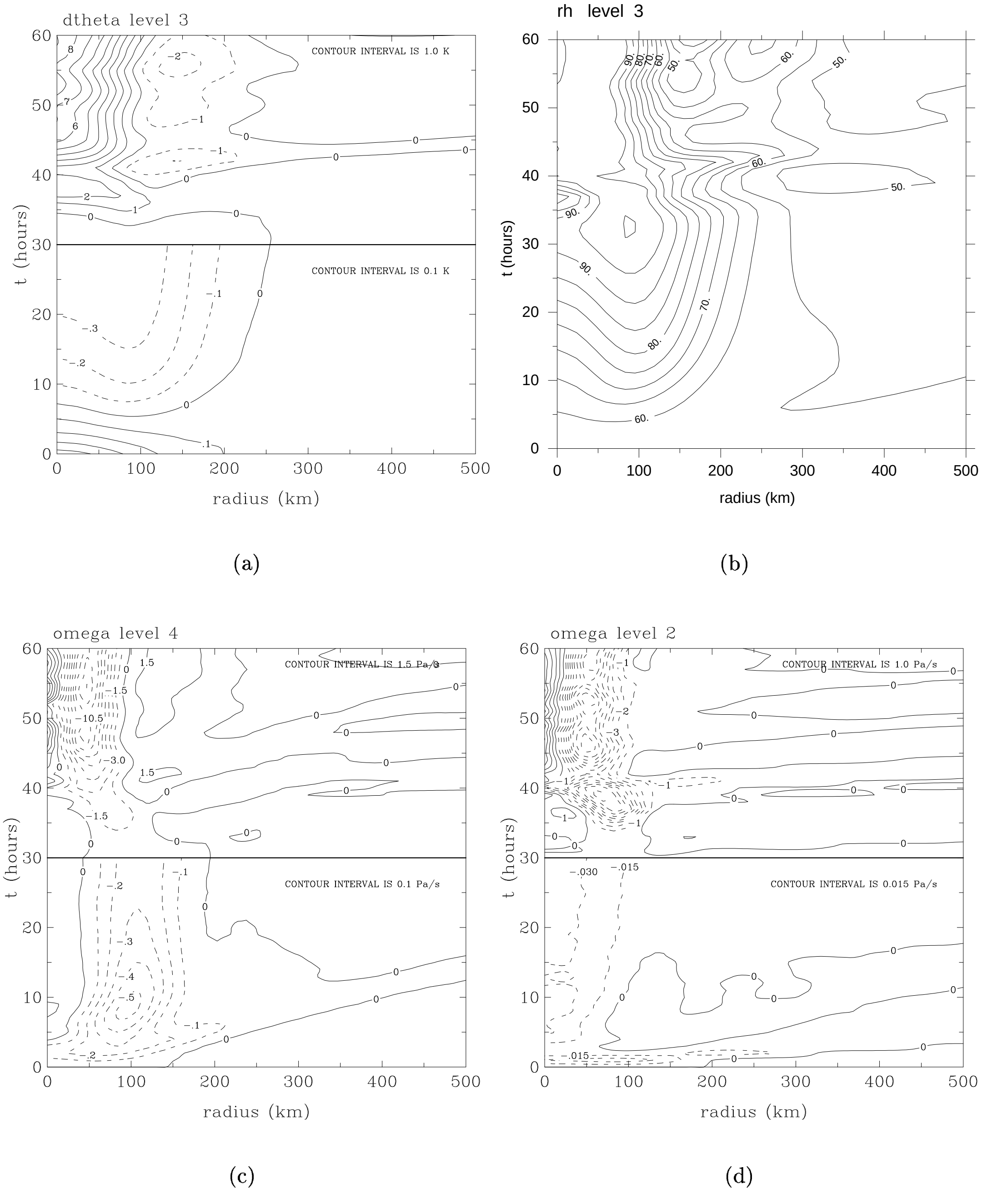

(a)

(b)

(c)

(d)

Figure 12. Legend as for Fig. 11 except for (a) perturbation potential temperature in deg. K at level-3, (b) relative humidity at level-3 (contour interval 5%), (c) vertical p-velocity in Pas^{-1} at levels-4, and (d) level-2. The contour intervals in (a), (c) and (d) are smaller for $t < 30$ h than for $t \geq 30$ h as indicated in respective panels.

the buoyancy distribution is in thermal-wind balance, associated with the decay in the tangential circulation with height. This inflow is accompanied by strong upflow in an annular region surrounding the core at level-4 (Fig. 12c) and level-2 (Fig.12d), and strong outflow at level-1 (Fig. 11c). The existence of positive buoyancy is indicated by the perturbation potential temperature distribution shown in Fig. 12a. The pulse in the secondary circulation commences at about 32 h and lasts only a few hours, essentially during the early stages of rapid deepening. Subsequently the inflow declines at level-3 and the inflow maximum slowly extends to larger radii as the vortex itself expands (Fig.11b,d). With the intensification of the vortex, after about 30 h, the vertical velocity fields at level-4 (Fig. 12c) and level-2 (Fig.12d) show a region of subsidence along the rotation axis, indicative of an "eye", together with a surrounding annular region of strong ascent, the model analogue of eyewall convection. There is an adjacent annular region of subsidence at level-4, beyond about 90 km in radius, which dries the air in the middle layer (as indicated in Fig. 12b) and in the boundary layer. The region of cooling between about 100 and 200 km radius seen in Fig. 12a is associated with the ascending motion at these radii at level-2.

Salient features of the flow evolution in Expt. 2, which incorporates the modified Arakawa parameterization of deep convection, are exemplified by the time-radius plots shown in Figs. 13 and 14. The plots of the tangential and radial wind components, the perturbation potential temperature and the relative humidity at level-3 are shown in Fig. 13, while Fig. 14 shows the corresponding isolines of convective and explicit precipitation, the calculations of which are detailed in Appendix D and in section 3.2, respectively. The cooling associated with the boundary-layer-forced ascent and moistening due to strong surface moisture fluxes at early times lead rapidly to deep convective instability in the core region and, in contrast to Expt. 1, the ensuing subgrid-scale convection progressively warms this region before it saturates on the grid scale (compare the perturbation potential temperature plot in Fig. 13c with that in Fig. 12a). This warming accounts for the slow intensification during the gestation period described in section 4.1 above. The increase in relative humidity by the mean secondary circulation is opposed by drying associated with the intra-cloud subsidence that accompanies parameterized deep convection (c/f the relative humidity plots in Figs. 12b and 13d). The drying, which occurs at all levels including the boundary layer, delays the onset of grid-scale saturation and thereby the period of rapid development. The amount of drying outside the core region is too large in the mature stage and this appears to be attributable to the coarse vertical resolution.

In the early stages of evolution the precipitation is wholly associated with the convection scheme (Fig. 14a), but as noted earlier, when grid-scale saturation occurs, the parameterization scheme shuts down and the period of rapid deepening begins. Subsequently precipitation occurs predominantly on the grid-scale (Fig. 14b). This result is similar to a finding of Baik *et al.* (1990a), who used the Betts-Miller parameterization scheme in an axisymmetric model with eleven levels in the vertical. Figures 1 and 2 in their paper show at least three periods of rapid intensification, each coinciding with a sharp increase in grid-scale precipitation and a decline in subgrid-scale precipitation.

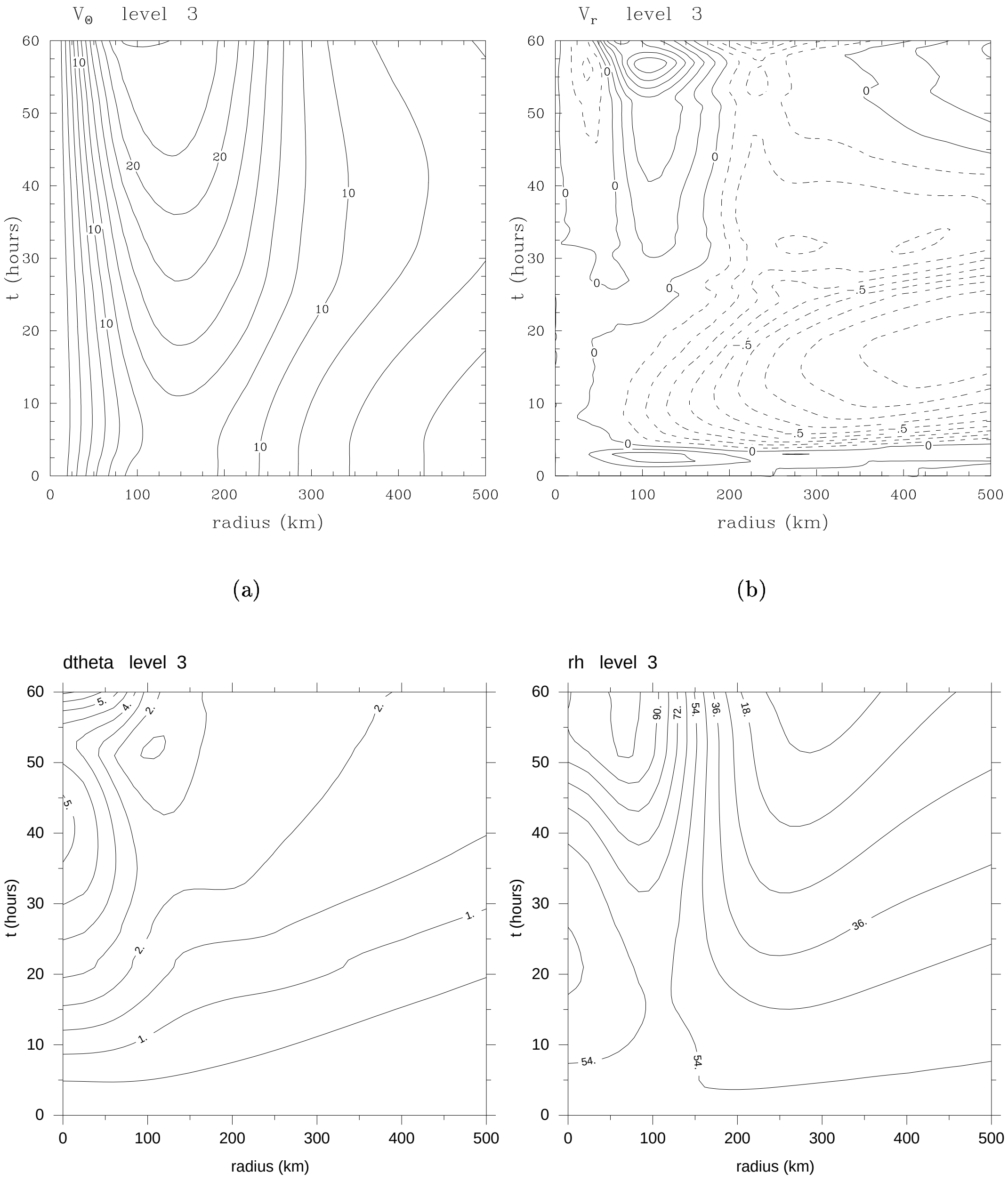

(a) (b)

(c) (d)

Figure 13. Legend as for Fig. 11, except for (a) the tangential wind speed (contour interval 2 ms^{-1}), (b) the radial wind speed (contour interval 0.1 ms^{-1}), (c) the perturbation potential temperature (contour interval 0.5 K), and (d) the relative humidity (contour interval 9%), all at level-3 in Expt. 2, which uses the modified Arakawa parameterization for deep convection.

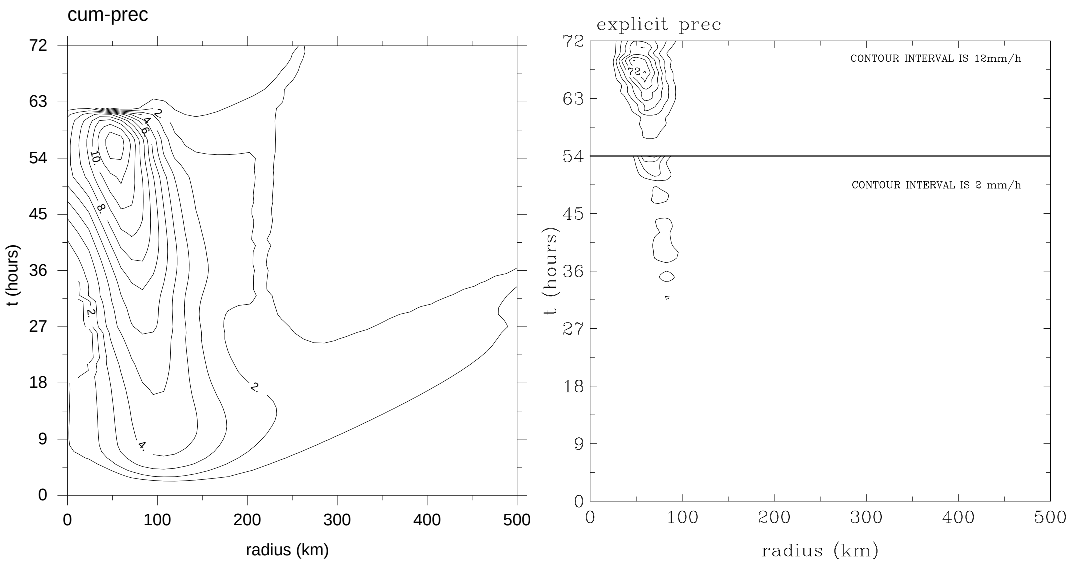

(a) (b)

Figure 14. Legend as for Fig. 11 except for (a) the convective precipitation (contour interval 1 mm h^{-1}), (b) the explicit precipitation (contour interval 2 mm h^{-1} for $t < 54$ h and 12 mm h^{-1} for $t \geq 54$ h), in Expt. 2.

For the relaxation times chosen, the vortex evolution in Expt. 3, which uses the Emanuel parameterization scheme, is very similar to that for the Arakawa scheme and the maximum wind speed attained is almost the same (Fig. 10b).

In Expt. 4, which uses Ooyama's scheme, vortex development is even more rapid than in the case with only explicit latent-heat release. In this experiment, M_{c4} is much larger than in other two schemes and the radial distribution is radically different from Expts. 2 and 3, with deep convection confined to the inner-core region. This is illustrated in Fig. 15, which shows the time-radius plots of M_{c4} for the three calculations that include a parameterization of subgrid-scale deep convection. The larger mass-flux implies larger subsidence heating and therefore larger buoyancy whereupon the convergence in layer-3 is stronger than in Expts. 1 - 3. Moreover, since the convective heating is confined to the core region, where there is boundary-layer convergence, the local radial buoyancy gradient is much larger than in Expts. 2 and 3 and leads to a stronger secondary circulation in the core region. Of course, the larger subsidence in Expt. 4 leads to stronger drying in layer-3, which if acting alone would delay grid-scale saturation in that layer. As it turns out, there are regions of boundary-layer convergence and upflow out of the boundary layer where the condition for subgrid-scale deep convection, $h_b > max(h_3^*, h_1^*)$, is not fulfilled. In these regions, moist boundary-layer air is transported upwards and quickly leads to grid-scale saturation and rapid deepening. In addition, since *subsidence into the boundary layer is not allowed in regions of precipitation-free air in Ooyama's scheme* (i.e. $M_{e4} \equiv 0$), there is less drying than in the

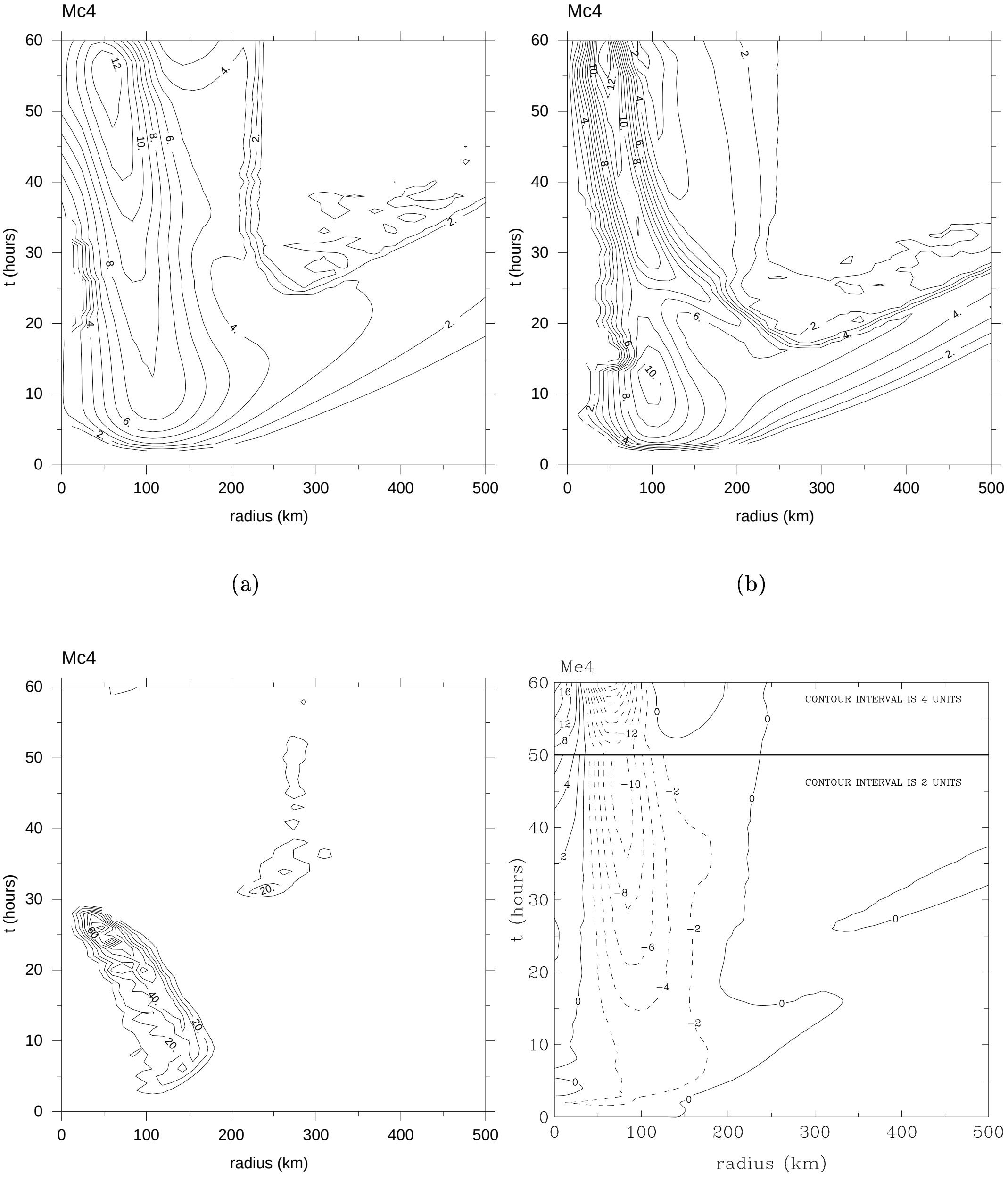

(a)

(b)

(c)

(d)

Figure 15. Legend as for Fig. 11, except for the convective updraft mass fluxes at level-4 (in units [10^{-2}kg $m^{-2}s^{-1}$). (a) Expt. 2 which uses the modified Arakawa convection scheme (contour interval 1 unit), (b) Expt. 3, which uses the modified Emanuel parameterization for deep convection (contour interval 1 units), (c) Expt. 4 which uses the modified Ooyama convection scheme (contour interval 10 units), and (d) the clear air mass flux, M_{e4}, at level-4 in Expt. 2 (contour interval 2 units for $t < 50$ h and 4 units for $t \geq 50$ h).

other schemes and the growth in boundary layer moisture from surface fluxes is therefore more rapid. As a result saturation occurs in the boundary layer after only about 8 h and the latent heat released generates buoyancy and enhances the resolved-scale secondary circulation in this case.

The radial distribution of cloud-base mass flux is similar in the calculations with the Arakawa and Emanuel schemes; in these deep convection progressively extends to over 500 km in radius until about 25 h, after which it contracts to the core region (c/f Figs 15a and 15b). The extension outwards accompanies the outward extension of stronger wind speeds, which enhance surface moisture fluxes, and the subsequent retreat is attributable to increased rates of subsidence into the boundary layer, which reduces the moist static energy of the boundary layer to a level where the conditions for deep convection are no longer fulfilled. The requirement of boundary-layer convergence to activate deep convection in the Ooyama scheme precludes this outward extension of deep convection to larger radii, even though the atmosphere becomes unstable at these radii in the sense that $h_b > max(h_3^*, h_1^*)$. This shortcoming of the Ooyama closure was pointed out by Emanuel (1989, p3451).

In comparing the three convection schemes it should be borne in mind that both the Arakawa and Emanuel schemes have adjustable time scales, τ_{dc}. In Arakawa's scheme, M_{c4} is inversely proportional to τ_{dc} whereas in Emanuel's scheme the dependence of M_{c4} on τ_{dc} is less direct and weaker. It is significant that in both these schemes, M_{c4} is calculated independently of the large-scale boundary- layer convergence. Nevertheless the net heating produced by parameterized convection *does* depend partly on the boundary-layer convergence as the latter determines $\overline{M}_4$ and therefore the rate of subsidence (or ascent) in clear air, M_{e4}, through the top of the boundary layer. For example, Fig. 15d shows the time-radius plots of M_{e4} for Expt. 2. Note that this quantity is always negative in an annular region between about 50 km and 150 km radius, i.e. there is always ascent in precipitation-free air in this region. This ascent tends to cool the lower troposphere and is a prerequisite for this layer to moisten. However, it is not sufficient as subsidence may still occur at level-2 and this has a warming and drying tendency, which may dominate the cooling and moistening tendency from ascent at level-4. For example, in the relative humidity plot for Expt. 2 shown in Fig. 10d, at radii around 100 km, net drying occurs until 16 h, after which time the lower troposphere begins to moisten.

4.3 Summary

The calculations lead us to hypothesize that the period of rapid development in tropical cyclones is accompanied by a change in the character of deep convection in the inner core region from buoyantly-driven, predominantly upright convection to slantwise * forced moist ascent. This change in character is presumably what many previous authors consider to be an "organization of convection" by the growing vortex. For example, Ooyama (1969, p374) remarks on "the intensification and maintenance mechanism (of tropical cyclones) as a cooperative process between the organized moist convection and the cyclone-scale vortex, a cooperative process between the primary and secondary circulation". Our findings are entirely consistent with this view.

It is interesting also to compare our findings with those of Emanuel (1995a), who conjectures that "the near saturation of a mesoscale column of the troposphere at the cyclone core is a necessary condition for (tropical cyclones) intensification". His argument is that "only when the troposphere is nearly saturated are the downdrafts that normally accompany deep convection suppressed; this allows surface fluxes to actually increase the entropy of the subcloud layer and, through moist adiabatic adjustment, the temperature of the troposphere." In his model the rate of humidification of the lower troposphere is prescribed in terms of the convective mass flux at cloud-base, the entropy difference between the lower troposphere and the boundary layer, and a measure of the relative humidity of the lower troposphere. In our model, on the other hand, intensification begins as soon as the boundary layer becomes unstable to deep convection, which happens within an hour or two. Slow intensification occurs despite the presence of precipitation-cooled downdrafts, but rapid intensification occurs only when a mesoscale column of the troposphere near the cyclone core becomes saturated. In the absence of shallow convection, humidification may occur only when the resolved-scale boundary-layer convergence exceeds that which can be accommodated in the updrafts of parameterized convection so that ascent from the boundary layer occurs in clear air. This moisture transport must also be sufficient to oppose the drying effect of subsidence from the upper troposphere.

Despite the crude explicit representation of moist processes in the present model, the calculations do raise the question as to what extent it is appropriate to represent moist processes in tropical cyclones in a way that precludes the occurrence of saturation on the grid scale. For example, the model developed by Emanuel (1989) effectively allows this possibility (neglecting, of course, the difference between a reversible and pseudo-adiabat), but the more recent scheme (Emanuel, 1995a) appears to preclude it.

The present findings may be compared also with those of Wada (1979), who investigated tropical cyclone evolution in a five-layer axi-symmetric, primitive-equation model using the Arakawa-Schubert cumulus parameterization scheme. The scheme represents

---

* Although the vertical resolution in the present model is inadequate to properly represent slantwise ascent, it is noted that the region of ascent at level 2 in Expt. 1 is generally broader than that at level 4 and in any case, slantwise ascent is consistent with observations (Jorgensen, 1984).

three types of clouds extending the top of a surface-based mixed layer to heights of 5, 9 and 13 km. She refers to these as L(ow)-, M(edium)-, and H(igh)-clouds, respectively. As in our model, she uses a horizontal grid spacing (at least in the inner region) of 20 km, and the Jordan environmental sounding. Her model domain size is 2500 × 2500 km and she uses a relatively weak initial vortex (maximum tangential wind speed approximately 8 ms^{-1} at a radius of about 130 km). Her model includes also an explicit representation of latent heat release. Wada finds the same three stages of evolution as described in section 4.1. At the initial instant, no H-clouds exist, but she notes that for the first few hours, M- and L- clouds appear within a radius of 100 km where there is frictionally-induced large-scale upward motion (and large surface moisture fluxes) and these subsequently spread out to radii up to 300 km during the gestation period (presumably as the vortex intensifies and therefore surface moisture fluxes destabilize the atmosphere to convection). The period of rapid intensification in her calculation is accompanied by strong convective activity of H- and M-clouds near the storm centre. Unfortunately she does not give details of the explicit release of latent heat, but she does note (on p515) that moistening occurs inside a radius of 200 km where large-scale upward motion occurs. Even so, any grid-scale saturation occurs at most in the upper troposphere (see panels D in Figs. 8 and 9 of her paper. Indeed the grid-scale relative humidity in the lower troposphere is only on the order of 50%, even in the innermost 100 km, during the period of rapid intensification and falls even lower during the mature stage. The drying is clearly associated with the intra-cloud subsidence in regions of strong convection and this evidently precludes grid- scale saturation in the lower troposphere. One may surmise that parameters in Wada's model are such that the frictionally-induced ascent in the core region is always less than the M- and H-clouds are able to accept (i.e., in our notation, M_{e4} is always positive). Finally recall that the Arakawa-Schubert convection scheme used in Wada's model makes the same small fractional area of cloud assumption as in ours.

Chapter 5. The role of three important physical processes

The aim of this section is to use the model to explore the role of three physical processes on tropical cyclone intensification, namely shallow convection, precipitation-cooled downdrafts and cumulus momentum transport. Three sets of experiments are carried out as detailed in Table(3). The first set of experiments (An) is designed to investigate the effects of shallow convection on vortex intensification; the second set (Bn) explores the consequences of omitting precipitation-cooled downdrafts from the control calculations; the third set (Cn) investigates the effects of vertical momentum transport by deep cumulus convection. The suffix n refers to the representation of moist processes chosen for the experiment (see caption to Table (3).

TABLE 3. List of sensitivity experiments described in this paper. The suffix n refers to the representation of moist processes. The values 1 - 3 refer to the closure on the cloud-base mass flux used for deep convection: 1 - modified Arakawa closure; 2 - modified Emanuel closure; 3 - modified Ooyama closure.

Experiment	**Sensitivity experiment**
An	Inclusion of shallow convection
Bn	Exclusion of downdrafts
Cn	Inclusion of vertical momentum transport by parameterized convection

5.1 Inclusion of shallow convection

Shallow convection in the tropical atmosphere plays an important role in bringing dry air (with low entropy and low moist static energy) from aloft into the boundary layer and in transporting moist boundary layer air (with high entropy and high moist static energy) into the lower troposphere (see e.g. Betts, 1975). Its representation in the model is based on the method suggested by Arakawa (1969), but with modifications in certain important details. The condition for the occurrence of shallow convection proposed by Arakawa (1969) is that $h_1^* > h_b > h_3^*$, so that shallow convection cannot occur in the same grid column as deep convection. Guided by the observation that deep clouds and shallow clouds frequently occur in close proximity, my model permits parameterized deep clouds and shallow clouds to coexist. Thus whether or not a grid column is stable to deep convection, it is considered to be unstable to shallow convection if $h_b > h_3^*$. In this case, a convective mass flux M_{sc4} carries boundary-layer air into the middle layer and compensating subsidence in clear air carries lower tropospheric air into the boundary layer at the same rate. It follows that shallow convection does not contribute to the grid-averaged mass flux, $\overline{M_4}$, defined in Chapter 3. Shallow convection is effectively suppressed at locations where grid-scale saturation occurs because $h_b \simeq h_3^*$ at these locations.

As in the case of deep convection, shallow cumulus clouds are assumed to occupy a small fractional area of the grid box so that the clear-air static energy (moist or dry) and specific humidity can continue to be used to approximate the corresponding grid-averaged quantities. It is assumed that shallow convection does not precipitate so that all liquid water produced by clouds re-evaporates above the boundary layer. With the foregoing considerations in mind, the prognostic equations for shallow convection are obtained in a similar way to those for deep convection. The tendencies of dry static energy, s_n, and specific humidity, q_n, (n = 3, b) associated with shallow convection are governed by the equations:

$$\alpha_3 p^* \frac{\partial q_3}{\partial t} = M_{sc4}\left(q_b - q_3\right), \tag{40}$$

$$\alpha_b p^* \frac{\partial q_b}{\partial t} = M_{sc4}\left(q_3 - q_b\right), \tag{41}$$

$$\alpha_3 p^* \frac{\partial s_3}{\partial t} = M_{sc4}\left(s_b - s_3\right), \tag{42}$$

$$\alpha_b p^* \frac{\partial s_b}{\partial t} = M_{sc4}\left(s_3 - s_b\right). \tag{43}$$

where $\alpha_n = \Delta\sigma_n/g$, and $\Delta\sigma_n$, (n = 3, b) are the depths of layers 3 and b in terms of σ. These tendencies are used to calculate the increments in dry static energy, Δs_n, and those in specific humidity during a time step. Then the heating/cooling contributions from shallow convection to Q_θ in the thermodynamic equation (Eq. 9) are obtained by setting $Q_{\theta n} = \Delta s_n/(c_p \pi_n)$, where π_n is the Exner function at the appropriate σ-level (n = 3, b) and c_p is the specific heat of air. The contributions to Q_q in the moisture equation (Eq. 10) are obtained in a similar way. By considering that shallow convection simply exchanges the moist static energy between middle layer and boundary layer, the equation is represented by the difference between these two layers instead of difference between the boundary layer and layer 4, as suggested by Arakawa (1969).

The closure assumption that determines M_{sc4} is obtained in a similar way to Arakawa's method for deep convection. In this case it is assumed that shallow convection drives the moist static energy of the middle layer towards that of the boundary layer on a specified time scale, τ_{sc}, at a rate proportional to the degree of instability as measured by $h_b - h_3^*$. In analogy with Eq. (31), the condition that determines M_{sc4} is

$$\frac{\partial}{\partial t}(h_b - h_3) = \frac{-(h_b - h_3^*)}{\tau_{sc}}. \tag{44}$$

The implementation of this condition is similar to that for deep convection (see section 3.4). The remaining problem is to select an appropriate value for τ_{sc}, which one might guess to be on the order of a few hours, bearing in mind that the middle layer in our model is relatively deep (about 6.4 km). Because it is difficult to assign a suitable value from available observations *, it is instructive to investigate the effects of shallow convection for a range of values of τ_{sc} and to assess the realism of these values in terms of the realism of the calculations. For reasons discussed in the subsection (e) , it is not possible to combine the foregoing representation of shallow convection with the Emanuel closure; thus shallow convection is examined here only for the Arakawa and Ooyama closures.

(*a*) *Expt. A1 - Arakawa closure*

Figure 16 shows time-series of the maximum tangential wind speed in the boundary layer for values of τ_{sc} = 4 h, 6 h, 8 h, 10 h, and 12 h and for the control calculation. As shown below, these values span a range over which the effects of shallow convection are exaggerated (i.e. τ_{sc} = 4 h) to one in which they are moderate. It can be seen that shallow convection reduces the rate of vortex intensification during the gestation period for all values of τ_{sc}, but the reduction is larger as τ_{sc} decreases. However, the length of the gestation period depends on τ_{sc} in a less uniform manner. When $\tau_{sc} = 4$ h, rapid intensification occurs about 20 h earlier than in the control calculation, but as τ_{sc} increases, so does the gestation period until τ_{sc} reaches a value of about 12 h, when rapid intensification occurs about 40 h later than in the control calculation. As τ_{sc} increases further, the gestation period declines towards that of the control calculation; for example, when τ_{sc} = 16 h, the delay is only 35 h (not shown). The reasons for these changes are examined below.

The direct effects of shallow convection, in the model and in reality, are to moisten and cool the lower troposphere and to warm and dry the boundary layer. In doing so shallow convection increases the moist static energy of the lower troposphere and lowers that of the boundary layer. However, as pointed out by Emanuel (1989, p3455), *the transport of air with low moist static energy from the lower troposphere to the boundary layer by shallow convection stabilizes the atmosphere not only to shallow convection, itself, but also to deep convection.* The stabilization in the vortex core region reduces the deep convective mass flux in that region and therefore the rate of heating and drying in the troposphere. This reduction in heating together with the cooling associated with shallow convection in the lower troposphere diminishes the

---

* It is typical of simple convection schemes that one ends up with unknown parameters of this type; for example, Emanuel (1989) arbitrarily chooses a cloud fraction for shallow convection to close the problem, while Emanuel (1995a) chooses an *ad hoc* parameter to represent the moistening by shallow convection in terms of the mass flux for deep convection.

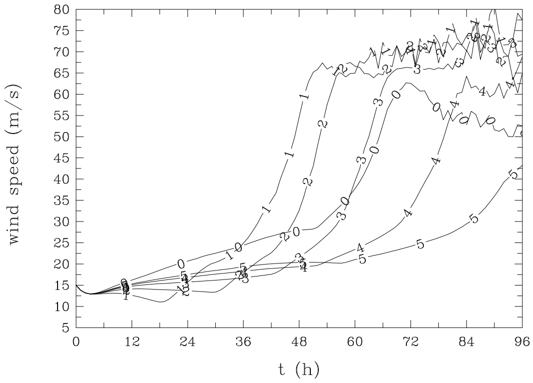

Figure 16. Evolution of maximum tangential wind speed in the boundary layer in Expt. A1 with different adjustment time scales for shallow convection, τ_{sc}. Numbers on the curves refer to: (0) control calculation; (1) $\tau_{sc} = 4$ h; (2) $\tau_{sc} = 6$ h; (3) $\tau_{sc} = 8$ h; (4) $\tau_{sc} = 10$ h; and (5) $\tau_{sc} = 12$ h.

buoyancy * in the vortex core and thereby acts as a brake on vortex intensification. This explains the lower intensification rate during the gestation period indicated in Fig. 16, which decreases with τ_{sc}. Nevertheless, the additional moistening of the troposphere by shallow convection and the reduction in drying by deep convection might be sufficient to enable the vortex core to saturate earlier on the grid scale (an effect that is precluded in Emanuel's (1989) and (1995a) models). At this point, rapid intensification would commence as in the control calculation. These two competing effects help to explain the different development indicated in Fig. 16, which would suggest that shallow convection leads to earlier grid-scale saturation for τ_{sc} less than about 8 h. This is confirmed by examination of the relative humidity fields (figures not shown). For longer time scales, the reduced secondary circulation is the dominant effect and grid-scale saturation is delayed.

A further effect of shallow convection is to stabilize the outer part of the vortex, thereby reducing the radial extent of deep convection. This reduction enhances the broader-scale radial buoyancy gradient in the troposphere and contributes to a strengthening of the secondary circulation of the vortex, opposing the aforementioned tendency of the reduced heating locally in the core region.

Some of the foregoing effects are indicated in Fig. 17, which compares time-radius plots of the azimuthal-average of various quantities in Expt. A1 (for $\tau_{sc} = 10$ h) with those of the control calculation. Arguments are presented in the next section in support of the choice of this value for $\tau_{sc} = 10$ h. Panels (a) and (b) compare the perturbation potential temperature in layer 3 for the two experiments (i.e. the difference between the potential temperature at some radius and that at some large radius) and panels (c) and (d) compare the corresponding relative humidities. The first two panels confirm the *net* cooling effect of shallow convection during the gestation period (up to 50 h), especially in the inner core region. As explained above, the cooler temperatures in Expt. A1 are partly due to shallow convection itself and partly due to the reduced instability to deep convection, which is evident in the weaker cloud-base mass flux of deep convection up to 50 h (compare panels (a) and (b) in Fig. 18). The cooler temperatures and higher absolute moisture in Expt. A1 lead to higher relative humidities in layer 3 as is seen by comparing panels (c) and (d) of Fig. 17. However the rate of increase is less in Expt. A1 than in the control experiment on account of the weaker secondary circulation. The weaker secondary circulation, itself, is a result of the reduced buoyancy in the core when shallow convection is included (c/f panels (a) and (b) of Fig. 17.).

---

* Buoyancy is proportional to the density difference between a point in a fluid and that at some reference density. The reference density is often taken as the density of the environment at the same level, but in a rapidly-rotating vortex it is more accurate to compare densities on the same isobaric surface.

In the control calculation, which does not include shallow convection, the atmosphere becomes conditionally unstable to deep convection over a progressively broader region that extends to over 500 km, whereas in Expt. A1, the extent of vigorous deep convection (as characterized, for example, by the contours with 4 units and higher) is a little more confined in radius. The rapid retreat of the region of deep convection in the control calculation after about a day is a result of enhanced broad-scale subsidence outside the vortex core as the vortex rapidly intensifies, which stabilizes the atmosphere to deep convection.

(*b*) *The choice of* τ_{sc}

A careful examination of the results of the calculation with $\tau_{sc} = 4$ h indicates that the calculation is not very realistic (figures not shown). For one thing the cooling of layer 3 by shallow convection is so strong that it totally negates the heating due to deep convection and there is negative buoyancy in layer 3 in the core region during the gestation period. Moreover the relative humidity in the boundary layer falls below 40% inside a radius of 250 km from the axis. The vortex doesn't intensify in this case until grid-scale saturation occurs in layer 3 at about 20 h. This extreme behaviour declines with increasing values of τ_{sc} and is not apparent for $\tau_{sc} = 10$ h. In the latter case, for example, there is positive buoyancy in layer 3 in the core region during the gestation period (Fig. 17b). In particular, the boundary layer humidity structure is more realistic in this calculation than in the control calculation as can be seen by comparing the time-radius plots of the azimuthally-averaged relative humidity in the boundary layer the two calculation. The extreme drying that occurs in the control calculation between about 100 km and 200 km in radius is considerably reduced in Expt. A1 and the boundary layer no longer saturates at an early stage inside 100 km radius as in the control calculation.

As τ_{sc} increases beyond about 8 h, the moistening of the middle troposphere by shallow convection is overshadowed by the reduction in the strength of the secondary

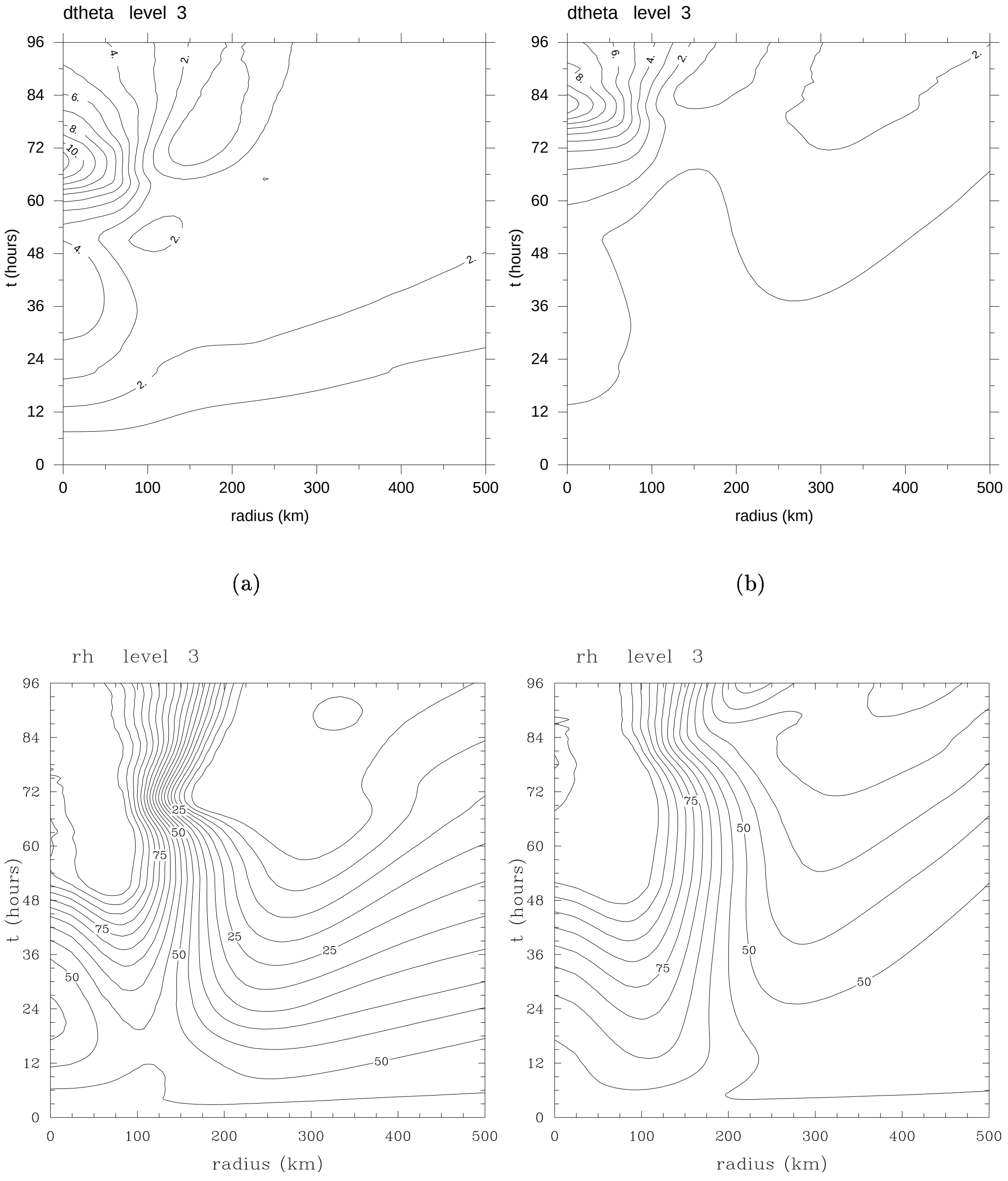

(a) (b)

(c) (d)

Figure 17. Time-radius plots of the azimuthally-averaged potential temperature deviation [in deg. K] in the middle layer in (a) the control calculation, and (b) in Expt. A1 with shallow convection when τ_{sc} is 10 h. Panels (c) and (d) show the corresponding plots of relative humidity [in %].

circulation, which reduces the rate of moistening in the inner core by grid-scale ascent. As a result, the gestation period is prolonged by a delay in the time of grid-scale saturation. As τ_{sc} increases beyond about 14 h, the shallow convective mass flux becomes too weak to have a significant effect on the transport of moist static energy between the boundary layer and layer 3, and the evolution of the vortex approaches that of the

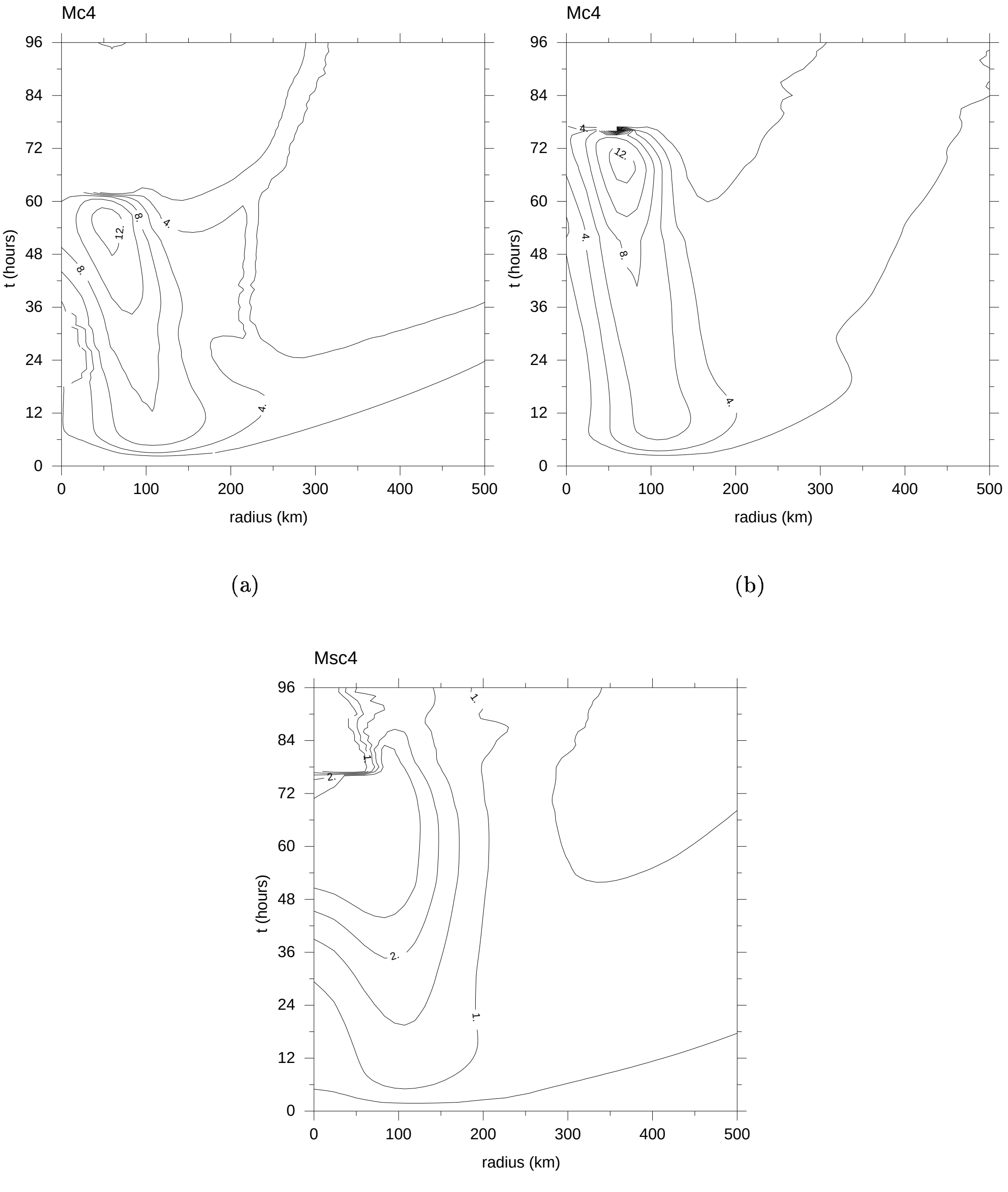

(a)

(b)

(c)

Figure 18. Time-radius plots of the azimuthally-averaged mass flux of deep convection at level 4 in units 10^{-2} kgm^{-2}s^{-1} in (a) the control calculation and (b) in Expt. A1. with shallow convection when τ_{sc} is 10 h. The mass flux of shallow convection in units 10^{-2} kgm^{-2}s^{-1} in the latter experiment is shown in panel (c).

control case. This behaviour is exemplified by the calculation for $\tau_{sc} = 16$ h, in which the period of rapid intensification occurs 5 h sooner than in the case with $\tau_{sc} = 12$ h, i.e. closer to the control case.

On the basis of the foregoing results, it has concluded that a value for τ_{sc} of about

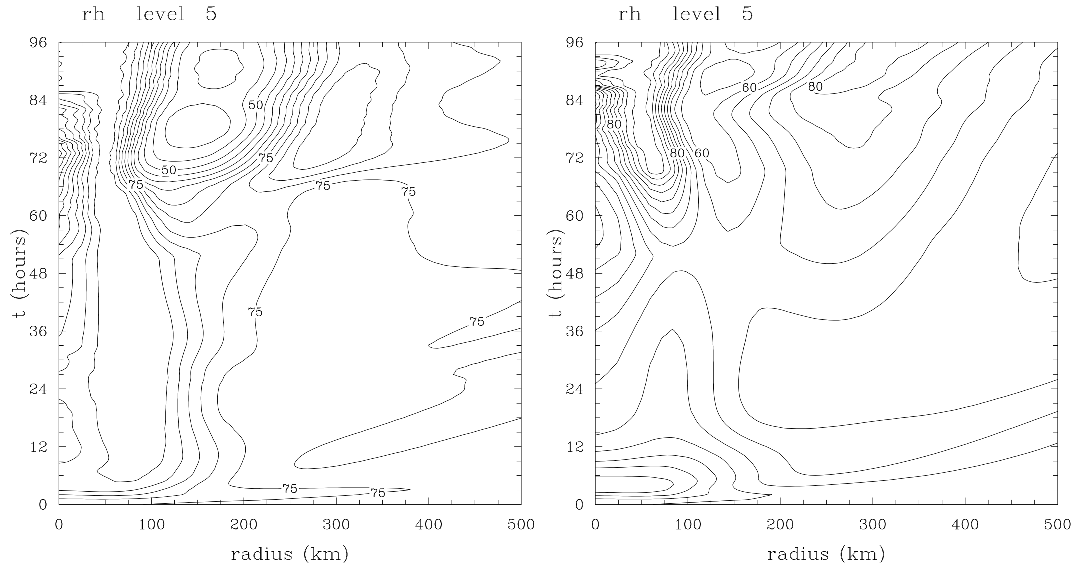

(a) (b)

Figure 19. Time-radius plots of the azimuthally-averaged relative humidity [in %] in the boundary layer in (a) the control calculation, and (b) in Expt. A1 with shallow convection when τ_{sc} is 10 h.

10 h - 12 h is the most realistic choice for the present model.

(*c*) *Expt. A3 - Ooyama closure*

With the Ooyama closure for $\tau_{sc} = 10$ h, shallow convection has no perceptible effect on the vortex intensification rate (as measured by the maximum tangential wind speed in the boundary layer) for the first day of integration. After this time the period of rapid intensification is almost complete (figure not shown). Thereafter, in the mature stage, both this and the control calculation show fluctuations in intensity with time. In Expt. A3, the fluctuations have larger amplitude, but the mean intensity is about 10 ms^{-1} more than in the control calculation (about 67 ms^{-1} compared with 57 ms^{-1}). For $\tau_{sc} = 4$ h, the onset of rapid intensification is reduced by about 16 h, but there is little difference in the mean intensity in the mature stage compared with $\tau_{sc} = 10$ h. While the calculations using the Arakawa closure with $\tau_{sc} = 4$ h show that the cooling associated with shallow convection outweighs the warming due to deep convection during the gestation period, this is not the case with the Ooyama closure as the deep convective mass flux at cloud-base is much stronger than that of Arakawa scheme, which is described in the section 4.2, and as a result, the heating by deep convection dominates the cooling. Indeed, the warm core is only weakened a little by shallow convection and this delays the onset of rapid intensification.

(*d*) *Summary*

In summary it has shown that, qualitatively, shallow convection reduces the degree of instability, not only to itself, but also to deep convection, thereby reducing the mass flux and hence the heating rate of deep convection. The diminished buoyancy leads to a weaker secondary circulation and reduces the rate of vortex intensification at early times. The quantitative effects of shallow convection depend both on the assumed time scale τ_{sc} and on convection scheme chosen to represent deep convection. Based on the effects of shallow convection on the boundary layer moisture and temperature, values of τ_{sc} on the order of 10 h appear to be most realistic.

(*e*) *Comparison with other studies*

It is of interest to compare the representation of shallow convection in this paper and the foregoing results with ones of other simple tropical cyclone models including those of Wada (1979), Emanuel (1989, 1995a) and Baik *et al.* (1990a,b), all of which are axisymmetric. Wada's model has five layers in the vertical and uses the Arakawa-Schubert parameterization of convection (Arakawa and Schubert, 1974). The model incorporates three types of convective cloud, all originating from the lowest (subcloud) layer, with tops at 5 km, 9 km and 13 km. These are designated L(ow)-, M(edium) and H(igh)-type, respectively, and all types may coexist. In the Arakawa-Schubert scheme, all cloud types are represented as entraining plumes, whereas in this formulation for shallow convection, the clouds and the mixtures of air that form as they evaporate are regarded as eddies in a mixing layer that includes the subcloud layer and the cloud layer. Emanuel (1997) shows that all evaporated mixtures of former clouds are negatively buoyant. In the simulation described by Wada *op. cit.*, convection is composed entirely of L- and M- clouds for about the first 30 h of integration. Thereafter, H-type clouds develop in the inner core region (radii less than 100 km) and progressively extend outwards. At the same time, the L- and M-type clouds steadily contract to the core region and soon after the period of rapid development, after 104 h of integration, they have more or less disappeared (see Figs. 3 and 10 of Wada's paper). In our model, shallow convection continues to occur outside the vortex core, even during the mature stage (see Fig. 18c), as happens also in reality.

Baik *et al.* (1990a,b) used the Betts-Miller parameterization for convection (Betts, 1986) in a model with 15 vertical layers. In their calculations, deep and shallow convection *are not permitted to coexist* in a grid column and the cloud top height is determined by a buoyancy criterion. They found that during the development stage, deep convection occurs mainly within a radius of 400 km from the vortex centre, while shallow convection occurs mainly outside this region. In contrast, in the mature stage, parameterized deep convection is suppressed and shallow convection becomes ubiquitous. However, like Wada *op. cit.*, they do not explore the role of shallow convection, itself.

The formulation of shallow convection in my model is similar to that of Emanuel (1989), but with the following differences:

- The vertical transfer in Emanuel's model is along angular momentum surfaces rather than upright;
- Instead of an assumed time scale, Emanuel's closure to determine M_{sc4} is based upon a simple updraft calculation that requires an arbitrary assumption about the fractional cloud cover of shallow convection (which he sets equal to 0.5);
- The mass fluxes of shallow (and deep) convection are proportional to the buoyancy (along angular momentum surfaces) of lifted subcloud-layer air, and hence to $(h_b - h_3^*)^{1/2}$ instead of $(h_b - h_3^*)$ as is the case here.

Emanuel's control calculation shows that when a weak vortex is placed in contact with the sea surface, the enhanced fluxes together with adiabatic cooling induced by the frictionally-induced secondary circulation destabilize the atmosphere. The initial shallow convective clouds import low entropy air into the subcloud layer, and because the saturation entropy through the depth of the troposphere is assumed to mimic the subcloud-layer entropy, the vortex core cools and the vortex decays. Emanuel argues that only when the anomalous surface fluxes are strong enough, and/or the middle troposphere is humid enough does the subcloud layer entropy increase, and with it the temperature of the core and the amplitude of the cyclone. He notes that once amplification begins, these clouds continue to dominate the convection outside the eyewall, keeping the boundary layer entropy relatively low, otherwise the vortex will expand and weaken. The cooling influence of shallow convection in Emanuel's model is reminiscent of that described above for values of $\tau_{sc} < 8$ h, but it is not possible to directly compare the time scale here with Emanuel's because of the differences in the formulation. However, we recall that the separate moistening effect of shallow convection that leads to earlier saturation on the grid scale in my model is not represented in Emanuel's model.

In Emanuel's (1995a) model, the closure on the cloud-base mass flux for deep convection is based on the assumption of boundary layer quasi-equilibrium, which balances the surface flux of moist static energy with the horizontal advection of this quantity and its decrease associated with subsidence in precipitation-cooled downdrafts and in clear air. The closure does not permit a partitioning of the cloud-base mass flux between shallow and deep convection without introducing an additional unknown parameter. For this reason, Emanuel *op. cit.* defines a somewhat *ad hoc* moistening function that partitions the detrainment of moisture into the upper and lower troposphere, based on the relative humidity of the lower troposphere. Because of the incompatibility of this formulation with my deep cloud model, I have studied shallow convection here only for the modified Arakawa-scheme and Ooyama schemes for deep convection.

(*f*) *Limitations of the shallow convection scheme*

The treatment of shallow convection in a model with such limited vertical resolution as mine or Emanuel's can be at best a first approximation to reality. Shallow convection in the tropics is mostly confined to the lowest few kilometers, although regions do occur where convection extends through deeper layers, without reaching the upper troposphere. Since the lower troposphere in my model is 6.4 km deep compared with a boundary layer depth of about 1 km, it follows that moist static energy transported into this layer from the boundary layer may be spread too thinly. Conversely, the moist static energy transported from the middle layer to the boundary layer may be too concentrated. The same remarks applies to Emanuel's (1989) model, which has a middle tropospheric layer of comparable depth to mine. Obviously a more complete treatment would require a model with improved vertical resolution, but the present calculations do isolate effects that might not be so apparent in such a model, and ones that could be tested with it.

5.2 Exclusion of precipitation-driven downdrafts

When the lower troposphere is relative dry, downdrafts associated with the evaporation of precipitation from deep convection moisten and cool the boundary layer (Betts, 1976). Two processes are involved, evaporation and downward transport. Evapouration of falling precipitation into the unsaturated sub-cloud layer is a heat sink and moisture source and brings the layer closer to saturation at constant equivalent potential temperature (or moist static energy). The cooling produces negative buoyancy, which together with the drag * of falling precipitation generates the downdraft. The downdraft transports potentially warmer and drier air into the sub-cloud layer. The two processes oppose each other in the sense that evaporation cools and moistens while downward transport warms and dries. Betts points out any combination can result, but the observations he reports suggest that the sub-cloud layer becomes cooler and drier after the precipitation and downdrafts. The coolness implies that there is sufficient evaporation into subsiding air to offset the adiabatic warming and the dryness is a consequence of the fact that even the saturation mixing ratio of subsiding air is still lower than that of the boundary layer.

To understand the role of downdrafts in my model, and the role that they might

---

* Note that only the thermodynamic effects of downdrafts are represented here; the dynamical effects are implicit in the specification of the proportionality coefficient relating M_{d4} to M_{c4}.

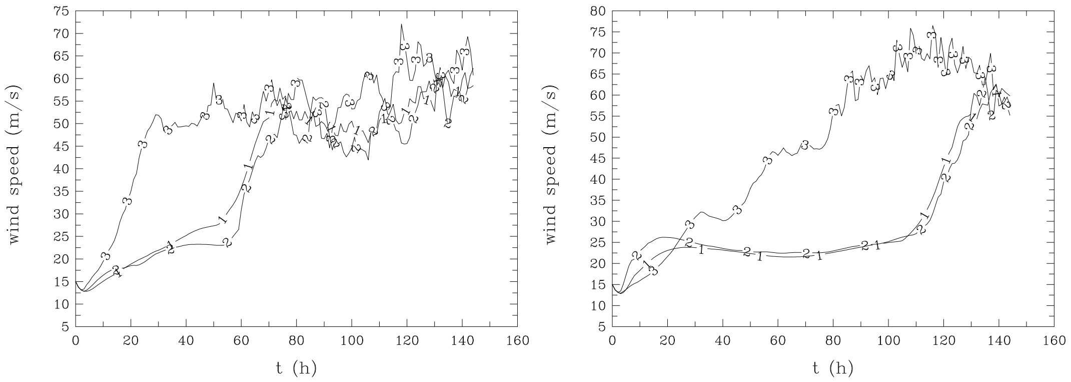

(a) (b)

Figure 20. Evolution of maximum tangential wind speed in the boundary layer [in ms^{-1}] in (a) the control calculations, and (b) in Expts. B1, B2 and B3.

play in reality, Expts. B1, B2 and B3 are carried out in which downdrafts are excluded. Figure 20 compares time series of maximum tangential wind speed in those calculations with that in the corresponding control calculation. It can be seen that one effect of downdrafts is to delay the onset of rapid intensification. With the Arakawa and Emanuel closures, this onset is delayed by about 60 h in each case. With the Ooyama scheme, intensification occurs in a series of bursts and the mean intensification rate is considerably reduced. The reason for the different behaviour in the absence of downdrafts is examined below.

In the formulation of the convection schemes, which is described in section 3.3, precipitation-driven downdrafts are assumed to be saturated and to originate from level 3. Since the moist static energy of an air parcel is unchanged by the evaporation of precipitation into it, downdrafts reduce the moist static energy of the boundary layer at a rate proportional to $h_b - h_3$. In contrast, subsidence into the boundary layer in clear air reduces the moist static energy of the boundary layer at a rate proportional to $h_b - h_4$, where h_4 is the interpolated value of moist static energy at the top of the boundary layer (see section 3.2). Since $h_3 < h_4$, the boundary layer moist static energy is diminished more when downdrafts are present. Thus downdrafts reduce the degree of convective instability and hence the cloud base mass flux, M_{c4}, which has a major impact the vortex evolution as discussed below. The three closure schemes are carried on in turn.

(a) Expt. B1 - Arakawa closure

Figure 21 shows a comparison of time-radius plots of azimuthally-averaged values of M_{c4} and the clear-air mass flux, M_{e4}, at the top of the boundary layer in calculations using the Arakawa closure, with and without downdrafts. Note the more rapid increase in M_{c4} during the first day of integration in the case without downdrafts (Fig. 21). However, for about the next day and a half, M_{c4} decreases in this case, whereas in the case *with* downdrafts, it increases steadily until grid-scale saturation occurs in the inner core, just prior to the period of rapid deepening. The decrease in M_{c4} between 24 h and 60 h in the case without downdrafts can be attributed to the reduction in convective instability measured by $h_b - h_1^*$ (the plots of this quantity are not shown as the patterns are very similar to those of M_{c4}). Although h_b is larger in the absence of downdrafts, the larger convective mass flux leads in this case to larger values of h_1^*. The net result is a reduction of the convective instability in the inner core, which puts a temporary brake on the rate-of-increase in M_{c4} and the vortex fills slightly (Fig. 21). After 60 h, M_{c4} begins a further period of increase as surface fluxes continue to moisten and destabilize the boundary layer.

The differing behaviour of the calculations with and without downdrafts may be understood in terms of a competition between the compensating subsidence associated with deep convection, which dries the middle troposphere, and the resolved-scale secondary circulation, which tends to moistens it. Moist boundary layer air enters layer 3 directly when $M_{e4} = M_{c4} - M_{d4} - \overline{M_4} < 0$, but for the moistening of layer 3 to occur, the magnitude of M_{e4} must be sufficient for the moisture transport to oppose the drying effects of subsidence in clear air from layer 1. During the first day of integration, the more intense vortex in the case without downdrafts is accompanied by larger frictional convergence, and thereby a larger resolved-scale mass flux $\overline{M_4}$, but also by a larger cloud-base mass flux M_{c4}. Our calculation shows that, after one day, the *net* effect is a decline in the magnitude of M_{e4} (compare panels (c) and (d) of Fig. 21). In other words, the magnitude of the ascent in clear air at level 4 increases less rapidly in the case without downdrafts and eventually becomes less than that in the case with downdrafts. The larger ascent in the case with downdrafts coupled with the larger boundary layer relative humidity leads to grid-scale saturation earlier in layer 3 than when downdrafts are absent. As a result, the vortex in the calculation with downdrafts steadily intensifies and the period of rapid intensification occurs much earlier than in Expt. B1. This behaviour would have been difficult to anticipate without doing the calculations.

(b) Expt. B2 - Emanuel's closure

A similar pattern of evolution occurs in Expt. B2. However, we should note that the influence of downdrafts is different in the present model from that in Emanuel's

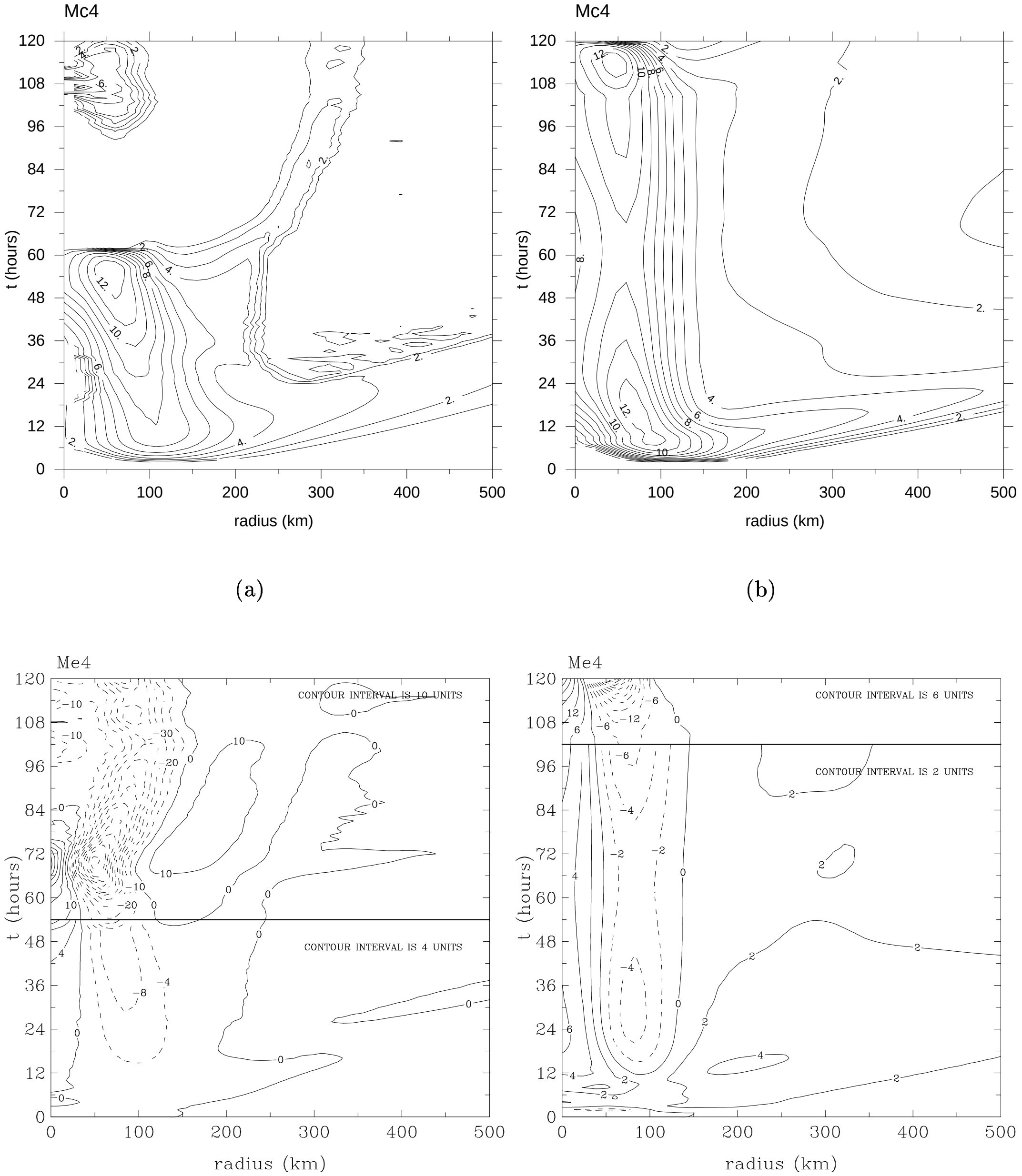

(a) (b)

(c) (d)

Figure 21. Time-radius plots of the cloud base mass flux for (a) the control calculation, and (b) Expt. B1, respectively. Panels (c) and (d) show the vertical mass flux in clear air at the top of the boundary layer for these calculations. Units 10^{-2} kgm^{-2}s^{-1} in all panels.

(1995a) model and may be slightly more realistic. In the latter, moist entropy is the sole thermodynamic variable and specific humidity and temperature are not predicted separately. As a result, the effects described here associated with saturation on the grid-scale cannot occur. Moreover, the moist entropy of downdraft air is the same in Emanuel's calculation as that of subsiding clear air; i.e. these have the same source level. Accordingly, the downdrafts have exactly the same effect on the subcloud entropy tendency as subsidence in the clear air: if the downdraft mass flux were reduced, the subsidence in clear air would increase to exactly compensate.

(c) Expt. B3 - Ooyama's closure

The closure in the modified Ooyama scheme sets the (net) cloud-base mass flux equal to the grid-scale mass convergence in the subcloud layer at grid points where the model atmosphere is unstable to deep convection, i.e., where $h_b > h_1^* > h_3^*$ (see Chapter 3). As a result there can be no subsidence or ascent in clear air, into or out of the subcloud layer in such regions (i.e. $M_{c4} = -p^*\overline{\sigma}_4/[g(1-\chi)]$ and $M_{e4} = 0$). Thus it is not possible for an entire grid column to become saturated in grid columns that are unstable to deep convection; it is possible only when forced ascent carries subcloud layer into the column when the latter is stable to deep convection. Suppressing downdrafts in the Ooyama scheme (i.e. setting $\chi = 0$ in the above expression for M_{c4}) significantly reduces the cloud base mass flux, M_{c4}, and therefore the rates of convective heating and buoyancy production in the vortex core. As a result the rate of vortex intensification is diminished, but the gestation period becomes ill-defined (see Fig. 20b). In this case, saturation in the vortex core region is delayed by about 60 h compared with the control calculation.

5.3 Vertical momentum transport

Experiment C1 is designed to explore the effects of allowing deep convective clouds to transfer momentum vertically. In this experiment, which uses the Arakawa closure, the subgrid-scale, deep-convective mass fluxes exchange momentum vertically between layers in addition to that transferred by the resolved-scale vertical circulation, $\overline{M_n}$. The formulation of parameterized momentum transfer is essentially the same as that for moist static energy as described in section 3.2. Momentum is transferred directly in deep convective updrafts from the boundary layer to the upper layer, where it detrains at a rate $M_{c4}(u_b, v_b)$, and momentum that is entrained into the updraft from the middle layer detrains in the upper layer at a rate $M_e(u_3, v_3)$. Convective-induced subsidence in clear air transfers momentum between layers at the rate $M_{cn}(u_n, v_n)$, where u_n, v_n are the velocity components at the interface level n. However the *net* momentum transfer in clear air depends on the sign of $\overline{M_n} - M_{cn}$, $(n = 2, 4)$. If this quantity is negative, ascent occurs in clear air and the momentum transfer through level n is upwards; otherwise the net transfer is downward. The equations governing the subgrid-scale transfer of vertical momentum in analogy with Eqs. 24-29 of section 3.2 are:

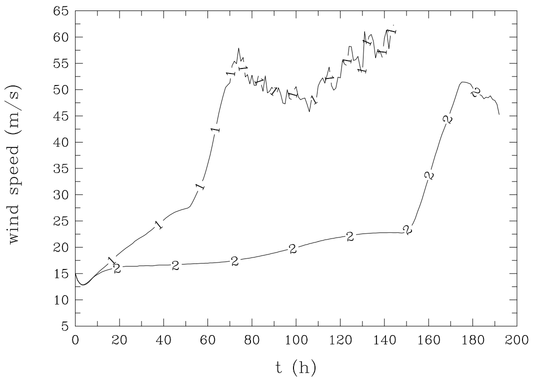

Figure 22. Evolution of maximum tangential wind speed in the boundary layer in ms^{-1} in the control calculation (curve labeled 1), and the Expt. C1 (curve labeled 2)

$$\alpha_1 p^* \frac{\partial u_1}{\partial t} = -M_{c2}u_2 + (M_{c2} - M_{c4})u_3 + M_{c4}u_b, \tag{45}$$

$$\alpha_3 p^* \frac{\partial u_3}{\partial t} = M_{c2}u_2 - (M_{c2} - M_{c4})u_3 - M_{c4}u_4, \tag{46}$$

$$\alpha_b p^* \frac{\partial u_b}{\partial t} = M_{c4}(u_4 - u_b), \tag{47}$$

$$\alpha_1 p^* \frac{\partial v_1}{\partial t} = -M_{c2}v_2 + (M_{c2} - M_{c4})v_3 + M_{c4}v_b, \tag{48}$$

$$\alpha_3 p^* \frac{\partial v_3}{\partial t} = M_{c2}v_2 - (M_{c2} - M_{c4})v_3 - M_{c4}v_4, \tag{49}$$

$$\alpha_b p^* \frac{\partial v_b}{\partial t} = M_{c4}(v_4 - v_b), \tag{50}$$

In the discussion that follows it is appropriate to consider the radial and azimuthal components of the vertical momentum transfer.

Figure 22 compares the evolution of the maximum tangential wind speed in the boundary layer in Expt. C1 with that in the control calculation. It is clear that parameterized momentum transport has a dramatic effect on vortex evolution by suppressing development for several days: after a short period of intensification the vortex in Expt. C1 stagnates and not until about 80 h does it begin to slowly intensify. Rapid intensification occurs eventually after 150 h. The reasons for the slow growth of the vortex in this case are evident in Fig. 23. Panels (a) and (b) compare time-radius plots of the azimuthally-averaged radial wind speed component in the boundary layer in the control calculation with that in Expt. C1, while panels (c) and (d) show similar plots of the radial and tangential wind components in layer 3 in Expt. C1. At early times the boundary layer inflow is a little weaker in Expt. C1 than in the control calculation and after about 10 h of integration the maximum inflow in both calculations begins to decline. In the control calculation the decline is arrested after a further 6 h and the inflow begins to increase as the vortex intensifies, but in Expt. C1 the increase begins later and is much slower. The reduced inflow in this case can be attributed to downward flux of *radial* momentum from the middle layer carried by the parameterized convective mass flux, directly because $u_3 < u_5$ (compare panels (b) and (c)), and indirectly because the downward advection of higher tangential momentum into the boundary layer from layer 3 increases the centrifugal force in the boundary layer, which tends to decelerate the inflow.

The compensating subsidence in the cloud-free air also transports the upper-level momentum to the middle layer, which leads to a decline of both the radial inflow and the tangential wind speed in layer 3 (Fig. 23 c, d). Indeed the radial inflow in this layer declines steadily at all radii after about 12 h, but it begins to slowly increase again beyond 200 km radius after about 36 h, and even later at smaller radii where the largest tangential wind speeds occur (see Fig. 23d). Panel (d) of Fig. 23 indicates a very slow growth in the tangential velocity component in layer 3 after about 6 h.

The cloud updraft carries inward-directed radial momentum and low-level cyclonic momentum upwards to the top layer. Acting alone, the former transfer would tend to weaken the outflow, whereas additional centrifugal force from the latter would strengthen it. It turns out the outflow is actually weaker than in the control calculation (plots not shown) indicating that the transfer of radial momentum is the dominant effect.

In summary, the overall effect of cumulus momentum transport is to significantly weaken the secondary circulation of the vortex and thereby to delay grid-scale saturation in the core, and the onset of rapid intensification. When grid-scale saturation occurs, the mass flux of parameterized deep convection rapidly declines and vertical momentum transport is accomplished by the resolved secondary circulation.

The result of including vertical momentum transfer in calculations using the Emanuel and Ooyama closures (Expts. C2 and C3) are similar to those described above in that the gestation period is significantly lengthened. With the Emanuel closure, rapid intensification does not begin until 190 h of integration, compared with 60 h in the control calculation. With the Ooyama closure, there is only slow intensification to about 85 h and accelerated growth thereafter, but no period of growth that one could describe as rapid compared with the control experiment.

As noted earlier, the assumption that horizontal momentum is conserved in convective-scale updrafts and downdrafts is an oversimplification and it may lead to an overes-

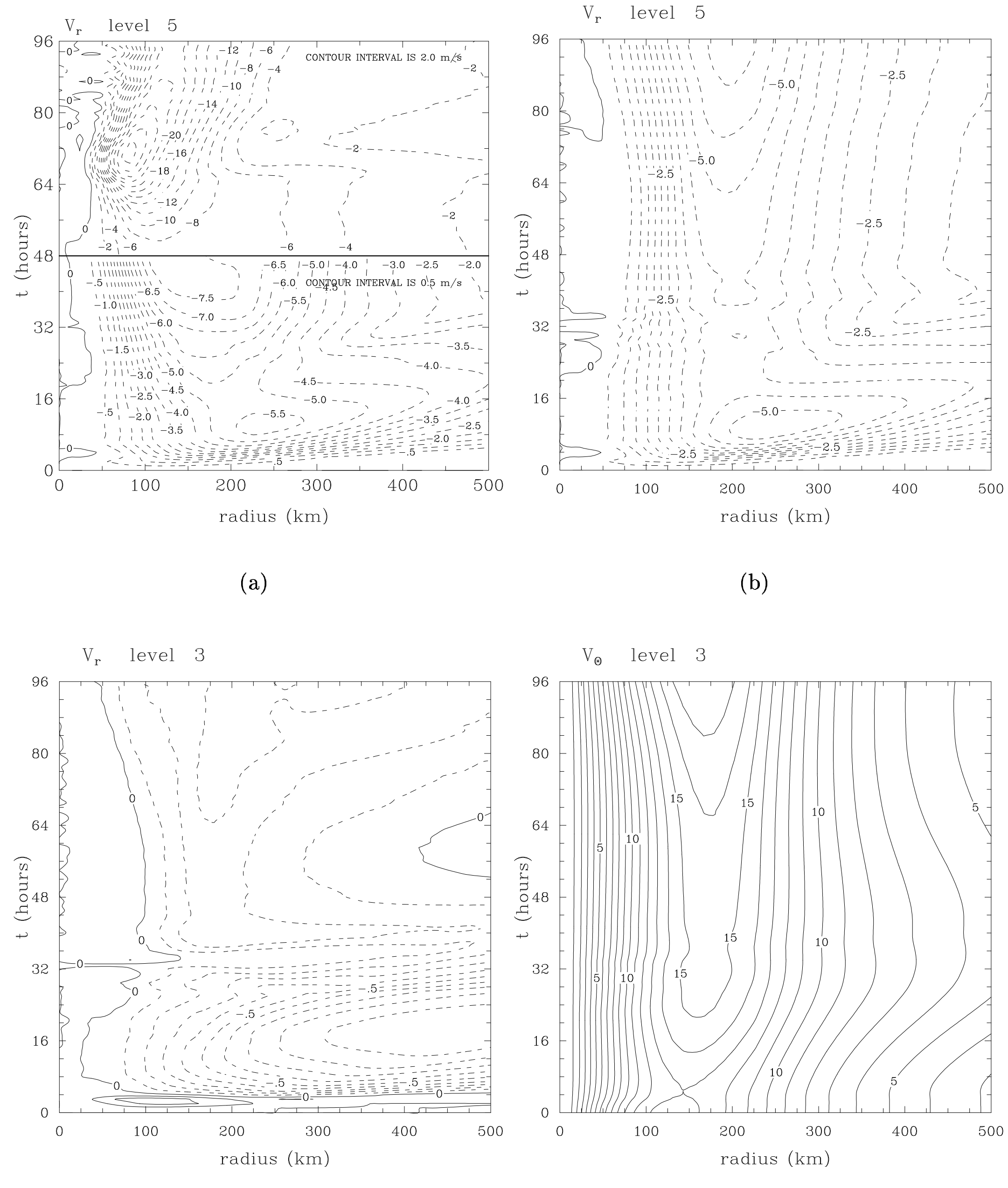

Figure 23. Time-radius plots of azimuthally-averaged wind fields: radial wind component (a) in the boundary layer in the control calculation, and (b) in the Expt. C1; (c) radial wind component and (d) tangential wind component in layer 3 in Expt. C1. Units are ms^{-1}.

timate of the effects of convective momentum transport. In the present model, the omission of this transport is less of an issue in the later stages of vortex evolution when, at least in the core region, momentum transport is mainly accomplished by the resolved secondary circulation.

5.4 Summary

This section has sought to isolate and elucidate the effects of three important physical processes on tropical-cyclone intensification using the three-dimensional tropical cyclone model described in Chapter. 2. Two of these processes (shallow convection and vertical momentum transport by deep convection) were notable omissions in the original model.

The role of shallow convection is examined using a representation suggested by Arakawa in which the convection is assumed to remove the convective instability between the boundary layer and the lower troposphere on a specified time scale. Calculations were carried out using either the modified Arakawa or Ooyama closure for deep convection. The inclusion of shallow convection leads to several competing effects on vortex evolution, the net effect being dependent on the assumed time scale for this process. These effects are listed below:

- The direct effect of shallow convection is to moisten and cool the lower troposphere and to warm and dry the boundary layer. In particular, the moist static energy of the boundary layer is reduced, as is the degree of instability between the two layers.
- An important effect of shallow convection is that it diminishes the instability to deep convection. Accordingly it reduces the mass flux of deep convection, and hence the rate of deep convective heating and buoyancy generation.
- The lower buoyancy associated with the cooling by shallow convection and reduced deep convective heating leads to a weaker secondary circulation and a reduced rate of vortex intensification during the gestation period.
- Unless the direct moistening is very strong, the weaker secondary circulation delays saturation on the grid scale and prolongs the gestation period.
- The drying of the boundary layer reduces the tendency of the boundary layer to saturate as happens in the control calculation, making the model more realistic.

In our representation of precipitation-cooled downdrafts, the downdrafts lower the moist static energy of the boundary layer more than subsidence outside downdrafts. As a result, they reduce the instability to deep convection, as does shallow convection. The effects of downdrafts on vortex intensification depend on the closure scheme used for deep convection. For the Arakawa and Emanuel closures, the rate of deepening during the early gestation period is larger when downdrafts are not included. This behaviour is as expected. However, downdrafts delay the time of rapid vortex intensification by about two and a half days in each case, a result that would not have been anticipated. Apparently, downdrafts allow a steady increase of the deep convective mass flux and hence the secondary circulation, whereas in the case where downdrafts are excluded, the more rapid initial build up is arrested and temporarily reversed by a subsequent stabilization to deep convection as the upper troposphere warms. It turns out that the deep convective mass flux and hence the secondary circulation in the case with downdrafts eventually exceed those in the calculation without downdrafts and grid-scale saturation is achieved earlier in this case. A similar delay in rapid intensification occurs also for the Ooyama scheme (about a day and a half), but the exclusion of downdrafts in this case leads directly to a smaller deep convective mass flux and therefore to a slower intensification rate.

In the early stages of vortex evolution, the vertical transport of horizontal momentum by deep convection weakens both the primary and secondary circulation of the vortex and significantly reduces the rate of vortex intensification. The omission of this transport is less of an issue in the later stages of evolution when, at least in the core region, momentum transport is mainly accomplished by the resolved secondary circulation.

The results of this study highlight the sensitivity of tropical cyclone intensification, especially the timing of rapid intensification, to the representation of three particular physical processes. These sensitivities are undoubtedly present in numerical models used to forecast tropical cyclones, but the complexities of forecast models makes it difficult to isolate the role of such processes in cyclone intensification. The insights provided by minimal models of the type described here, especially the interplay between the representations of deep and shallow convection, may be helpful in the future development and assessment of forecast models.

Chapter 6. Sensitivity study on the model parameters

In this chapter, we examine the sensitivity of the calculations in control case to various parameters as detailed in Table (4). The set of experiments (G-M) concerns the inclusion or omission of physical effects or changes in external parameters .

TABLE 4. List of sensitivity experiments described in this chapter. The suffix n refers to the representation of moist processes. The values 1 - 3 refer to the closure on the cloud-base mass flux used for deep convection: 1 - modified Arakawa closure; 2 - modified Emanuel closure; 3 - modified Ooyama closure. The value 4 refers to the use only of the explicit scheme for latent heat release.

Experiment	**Sensitivity experiment**
Gn	Sensitivity to the horizontal resolution
Hn	Sensitivity to the sea surface energy exchange coefficient
In	Sensitivity to the sea surface temperature
Jn	Inclusion of dissipative heating
Kn	Weak initial vortex
Ln	Sensitivity test to the convective time scale
Mn	Sensitivity to the mass flux formulation in Emanuel's scheme

6.1 Sensitivity to the horizontal resolution

Panel (a) of Fig. 24 shows the time evolution of minimum surface pressure in Expt. G1 with horizontal grid spacings of 10 km, 20 km (the control calculation) and 30 km. With a grid spacing of 10 km, the vortex begins to rapidly intensify 20 h earlier than with a spacing of 20 km, but with a 30 km grid spacing it has not begun to intensify, even after 96 h of integration. A similar finding was reported by Baik *et al.* (1990b) and is to be expected. There are two effects to consider. First, a relatively coarse horizontal resolution may prevent inward-moving air parcels attaining radii as small as they might otherwise do if the resolution were unlimited. Since intensification is a result of at least partial angular momentum conservation associated with the inflow, the vortex intensity would be therefore too weak. Increasing the resolution should allow air parcels to penetrate inwards, closer to the radius they would attain if the resolution were unlimited. This would lead to a stronger vortex. That this is the case is indicated in panels (b) and (c) of Fig. 24, which show time-radius plots of the azimuthally-averaged tangential wind speed in layer-3 for the calculations with a grid spacing of 20 km and 10 km, respectively. When the horizontal resolution is 10 km, the maximum tangential wind speed occurs at about 60 km from center at 48 h, and when it is 20 km, the maximum wind speed occurs at about 100 km from the center at 67 h. The second effect of decreasing the horizontal resolution is that grid-scale saturation can be achieved earlier and this accounts for the earlier onset of rapid intensification with a grid spacing of 10 km. We obtain a similar result using the Emanuel scheme (Expt. G2), but with the Ooyama scheme (Expt. G3), the vortex with the 30 km resolution *does* intensify within the 96 h of integration, although the period of rapid intensification is delayed by about 20 h.

6.2 Sea surface energy exchange coefficient

In my model, the turbulent flux of momentum to the sea surface and the fluxes of sensible heat and water vapour from the surface are represented by bulk aerodynamic formulae in the form

$$\begin{aligned}(F_u, F_v) &= -\rho C_d \left|\mathbf{u_b}\right| (u_b, v_b)\\ F_q &= \rho C_h \left|\mathbf{u_b}\right| (q_s^* - q_b)\\ F_{SH} &= \rho c_p C_h \left|\mathbf{u_b}\right| (T_s - T_b),\end{aligned} \tag{51}$$

where the subscript "b" denotes the value at the middle of the boundary layer, $\mathbf{u_b} = (u_b, v_b)$, T_s and q_s^* are the sea surface temperature (taken to be 28°C) and saturation specific humidity at this temperature, respectively; ρ is the near-surface air density; C_D is the surface drag coefficient; and C_h is the bulk transfer coefficient for heat and moisture. In section 2.4 we calculate C_D from the formula used by Shapiro (1992) and assume that $C_D = C_h$. In this section, the sensitivity of vortex intensification to the ratio of C_h/C_D is investigated, keeping C_D fixed with the same value as in section 2.4.

Figure 25 compares the maximum tangential wind speed attained in the boundary layer and the minimum surface pressure in calculations using the Arakawa scheme for three values of the ratio of C_h/C_D: 0.5, 1 and 1.5. When $C_h/C_D = 0.5$, the vortex intensifies only slightly after 96 h of integration, at which time the minimum surface pressure is 1003 mb and the maximum tangential wind speed is 20 ms^{-1}. When $C_h/C_D = 1$, the vortex begins to rapidly intensify after about 60 h of integration, and the minimum surface pressure and maximum tangential wind speed reach 970 mb and 55 ms^{-1}, respectively. With C_h/C_D=1.5, rapid intensification begins after 40 h of integration, and the minimum surface pressure and the maximum tangential wind speed reach 955 mb and 75 ms^{-1}, respectively. Increasing C_h increases the radial gradient of moist static energy in the boundary layer, and increasing C_D leads to increased frictional drag. Thus increasing the ratio of C_h/C_D leads to earlier and stronger vortex development, while decreasing it has the opposite effect. The sensitivity to the ratio of C_h/C_D is similar in Expts. H2 and H3, which use the other closures for M_{c4}. This behaviour is

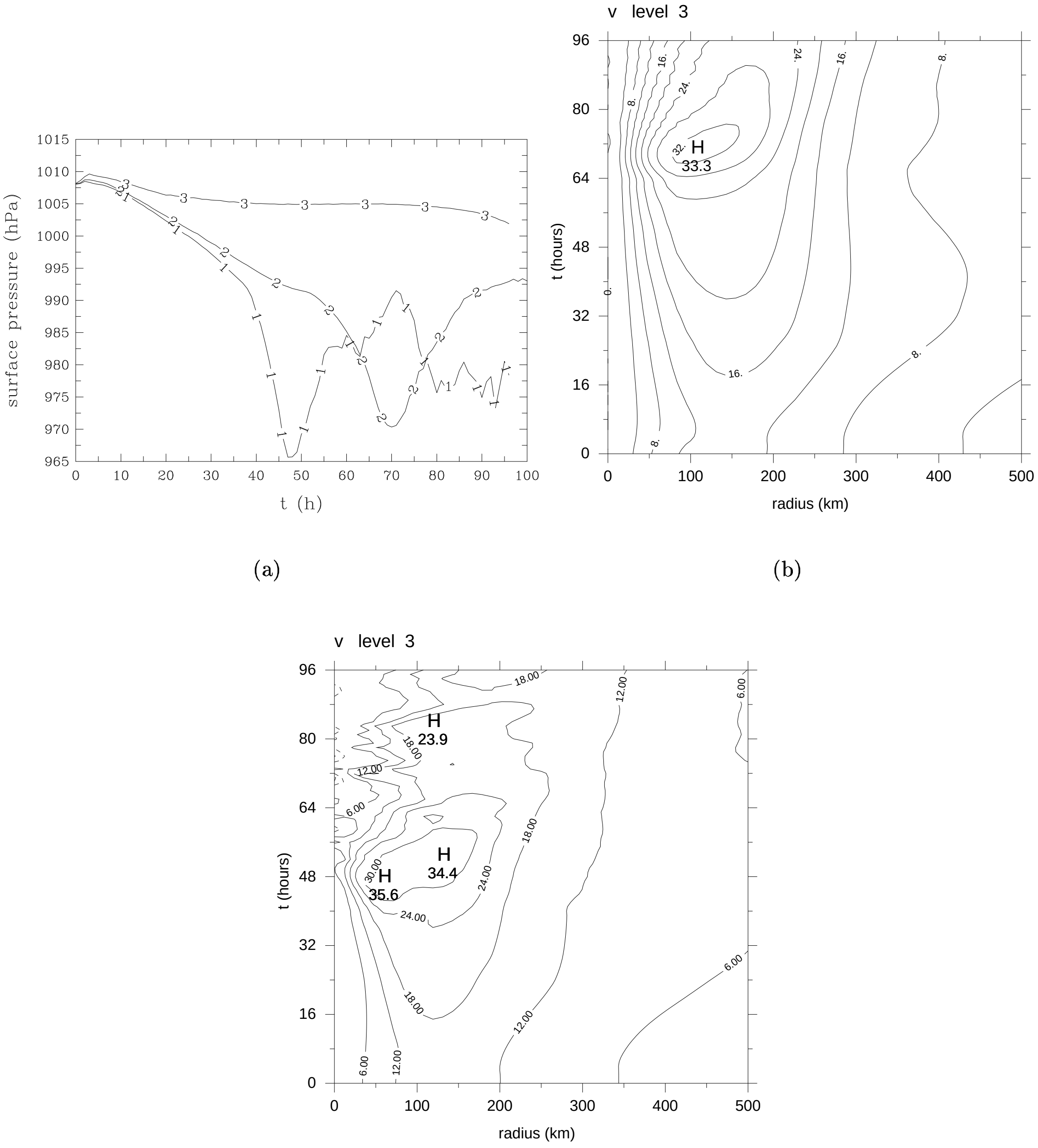

(a)

(b)

(c)

Figure 24. Evolution of (a) the minimum surface pressure [in mb] in Expt. G1. Numbers 1 - 3 on the curves refer to grid spacings of 10 km, 20 km and 30 km, respectively. Panels (b) and (c) show the azimuthally-averaged tangential wind speed at level-3 [in ms^{-1}] for grid spacings of 20 km and 10 km, respectively, in this experiment.

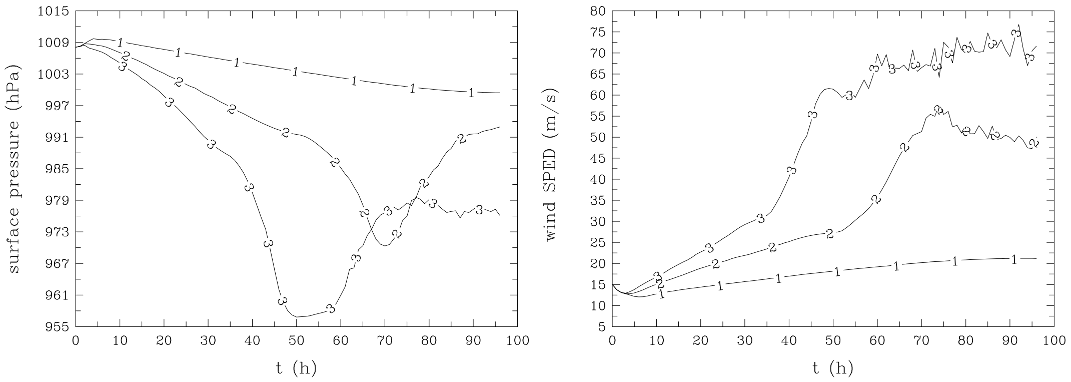

(a) (b)

Figure 25. Evolution of (a) minimum surface pressure [in mb], and (b) maximum tangential wind speed [in ms^{-1}] in the boundary layer for different ratios of C_k/C_D. Numbers on the curves denote: 1. $C_k/C_D = 0.5$; 2. $C_k/C_D = 1.0$; 3. $C_k/C_D = 1.5$.

similar to that found by Emanuel (1995b) as summarized in his Fig. 1.

The foregoing maximum intensities are broadly in agreement with those obtained using Emanuel's algorithm for estimating the maximum potential intensity (Emanuel, 1995b), which yields 38 ms^{-1}, 54 ms^{-1}, and 66 ms^{-1}, for $C_k/C_D = 0.5$, 1.0 and 1.5, respectively. For the case C_k/C_D=0.5, the vortex doesn't reach the mature stage in 96 h.

6.3 Sensitivity to the sea surface temperature

We examine now the dependence of vortex evolution on the sea surface temperature (SST) in calculations with the Arakawa closure for deep convection. Three calculations are carried out with fixed SSTs of 26^{o}C, 27^{o}C, 28^{o}C and 29^{o}C. Figure 26 shows time series of minimum surface pressure and maximum tangential wind speed in the boundary layer for these calculations together with those for the control calculation, which has an SST of 28^{o}C. Clearly the maximum wind speed increases and the minimum surface pressure decreases as the SST is increased, and also the gestation period is reduced with a higher SST. The behaviour is similar to that found by other authors (see e.g. Rotunno and Emanuel, 1987, Fig. 7; Baik *et al.* 1990b; Fig. 8) and is as one would expect, but it seems appropriate to place on record the magnitude of the differences in my model.

In the equilibrium stage, there is a balance between surface fluxes, entrainment at the top of the subcloud layer, and flux of low-entropy air from the lower and middle troposphere into the boundary layer by convective downdraughts. The equilibrium

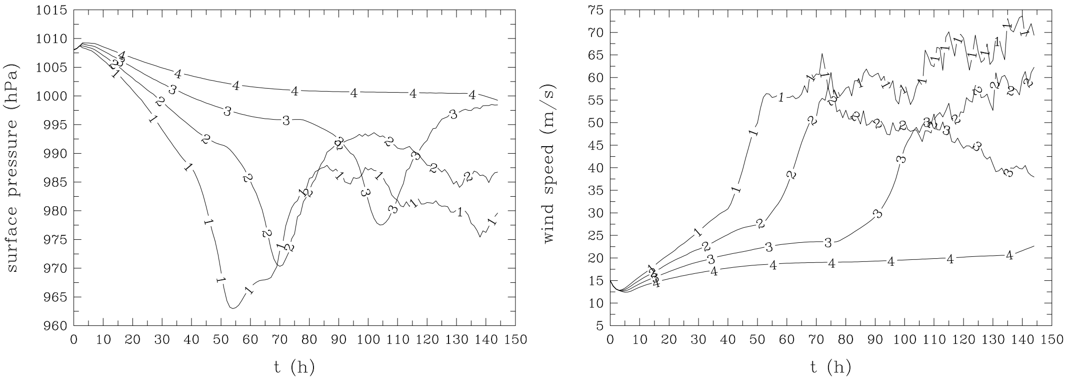

(a)

(b)

Figure 26. Evolution of (a) minimum surface pressure in mb, and (b) maximum tangential wind speed [in ms^{-1}] in the boundary layer for different sea surface temperatures, denoted by numbers on the curves: 1 (29^oC); 2 (28^oC); 3 (27^oC); 4 (26^oC).

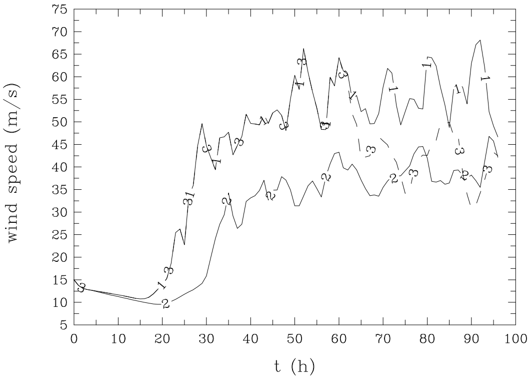

Figure 27. Maximum surface tangential wind speed [in ms^{-1}] , the number on the curves refers : 1. and 2. the control experiment with constant sea surface temperature of 28^o and 26^o. (b) the experiment where the sea surface temperature is abruptly decreased from 28^o to 26^o after 60 h of integration.

subcloud entropy is a weighted average of the entropy associated with the sea surface temperature (SST), the entropy of air just above the top of the subcloud layer, and the entropy of downdraughts. Therefore, the equilibrium entropy will increase or decrease with increasing or decreasing SST. What will happen if the vortex moves to the cold water after attaining the equilibrium stage? To test this idea, I carried out an experiment in which after the vortex attains the mature stage, the sea surface temperature is decreased by 2^o. For accuracy, I increased the vertical resolution to five layers with the depth in σ as 2/9,2/9,2/9,2/9,1/9 respectively from the top to the surface. Also for simplicity, we only use the explicit moist process to test the vortex intensity when it moves to the cold water. Fig. 27 is the time evolution of maximum surface tangential wind in the experiment with the constant sea surface temperature, 26^oC, 28^oC, and the time evolution of maximum surface tangential wind in the experiment in which the surface temperature is decreased from 28^oC to 26^oC after integrating 60 h.

In the experiment with constant surface temperature of 28^{o}C, the vortex starts to intensify at about 30 h and reaches the mature stage at about 60 h with the maximum tangential wind speed of 55 ms^{-1}. As the sea surface temperature is 26^{o}C , the rapid intensification occurs at 30 h, and the maximum tangential wind speed is 38 ms^{-1}. In the experiment where the sea surface temperature is reduced to 26^{o}C after 60 h, the vortex decays after 60 h, and the maximum tangential wind speed in the boundary layer is around 40 ms^{-1}, which is very close to the maximum wind speed value in the experiment when the SST is set to be 26^{o}C. The sea surface temperature has an effect on the moist static energy in the boundary layer, which plays a key role on the vortex intensification. When the surface temperature is reduced, the moist static energy in the boundary layer decreases. The same is true in the troposphere where the moist static energy is approximately equal to that in the boundary layer in the equilibrium stage. Therefore the strength of the vortex warm core is reduced on the account of decreasing SST, and the maximum wind speed which the vortex can achieve is reduced. The results I obtain here are consistent with the Emanuel's MPI theory (Emanuel, 1995b), where with an SST of 28^o, the maximum tangential wind speed is 54 ms^{-1}, and with a SST of 26^o, it is 43 ms^{-1}. In the Emanuel's MPI theory, the maximum intensity of vortex is proportional to the temperature difference of the sea surface and the upper troposphere, therefore the maximum intensity of vortex increases with the increasing of the sea surface temperature.

6.4 Inclusion of dissipative heating

Bister and Emanuel (1998) have shown that the heating associated with frictional dissipation in the boundary layer can increase the maximum potential intensity of tropical cyclones. To explore the effect of dissipative heating in my model I have carried out Expt. J1 in which a term Q_{fric}, representing the rate-of-working against frictional forces in the boundary layer, is added to the right-hand-side of thermodynamic equation (Eq. 9), where it characterizes to the frictional generation of heat. Here

$$Q_{fric} = \frac{C_D \left|\mathbf{u_b^3}\right|}{c_p \pi_b z_b}, \tag{52}$$

where z_b is the depth of the boundary layer. The details of the dissipative heating are listed in Appendix F. The differences between Expt. J1, which includes the dissipative heating for the calculation with the Arakawa closure, and the corresponding control calculation, are indicated in Fig. 28, which compares the maximum tangential wind speed in the boundary layer for these two experiments. The differences are barely perceptible during the gestation period because of the weak vortex, but the inclusion of dissipative heating brings forward the onset time of rapid intensification by about 10 h and leads to a more rapid rate of intensification, although there is little significant

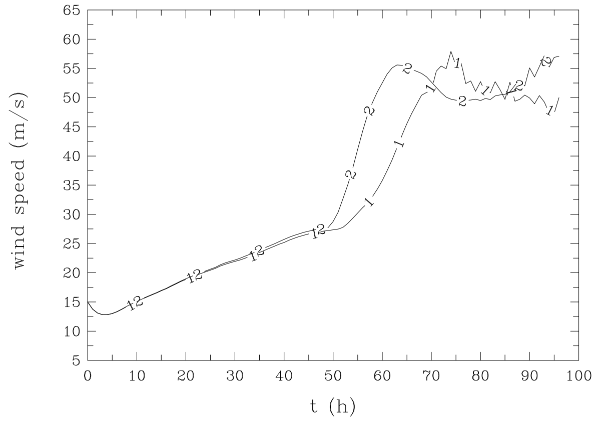

Figure 28. Evolution of maximum tangential wind speed in the boundary layer [in ms^{-1}] for the control calculation (curves labeled 1) and for Expt. J1 (curves labeled 2), which takes account of dissipative heating in the boundary layer.

difference in the maximum intensities attained in the two calculations.

6.5 Weak initial vortex

We examine two experiments (Expts. K1 and K4) in which the initial vortex has a maximum tangential wind speed of 10 ms^{-1} compared with 15 ms^{-1} in the control calculation. Expt. K1 includes the Arakawa closure, while Expt. K4 has only an explicit representation of deep convection. Figure 29 shows time series of the maximum tangential wind speed in the boundary layer in these experiments. As expected, the gestation period is lengthened considerably in each case, compared with the corresponding control calculation. Interestingly, the vortex in Expt. K4 *does* intensify after about four days of integration, indicating that the frictionally-induced convergence alone is sufficient to produce saturation in a column on a scale of 20 km given sufficient time. With the Arakawa closure, the vortex begins to slowly intensify, but after about two days it starts to decay. After a further two days intensification recommences, but the period of rapid intensification does not begin until the seventh day of integration. The first intensification period results from the buoyancy produced by deep convection in the inner region, as in the control case, but cooling associated with ascent in clear air in the core region gradually exceeds the warming effect and the core slowly cools. However, surface fluxes continue to destabilize the boundary layer and the heating by deep convection subsequently regains the upper hand and leads to the further period of steady development. Eventually, grid-scale saturation occurs in the core region and a period of rapid intensification begins, as in the control experiment.

6.6 Sensitivity to the convective time scale

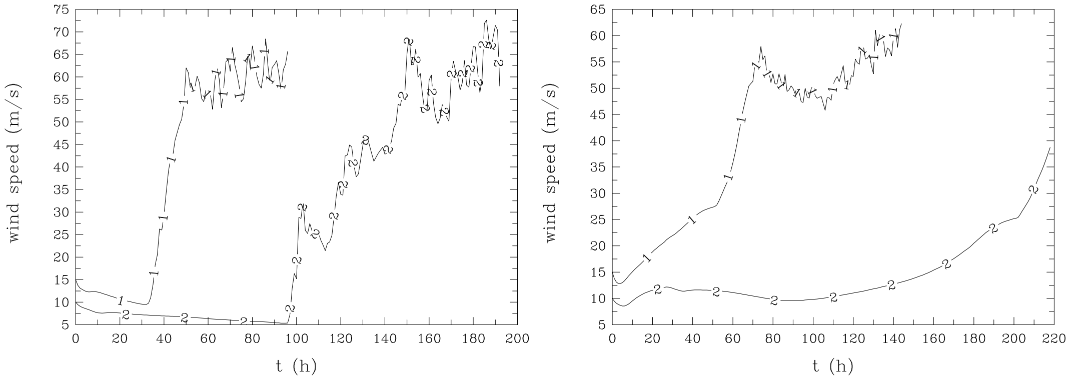

(a) (b)

Figure 29. Evolution of maximum tangential wind speed in the boundary layer [in ms^{-1}] (a) for the control calculation with explicit moisture process only (curves labeled 1) and for Expt. K4 (curves labeled 2), and (b) for the control calculation with Arakawa closure (curves labeled 1) and for Expt. K1 (curves labeled 2).

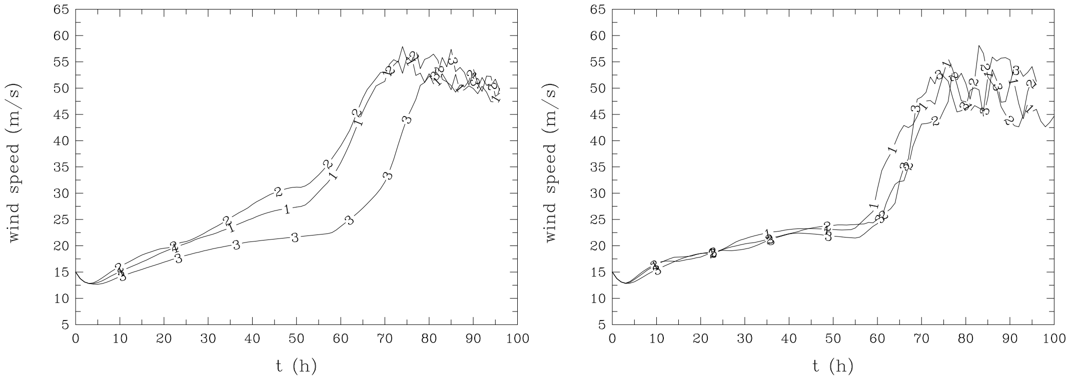

(a) (b)

Figure 30. Evolution of maximum tangential wind speed in the boundary layer [in m/s] in Expts L1 and L2. with Arakawa and Emanuel closure respectively. Numbers on the curves refer: 1. $\tau = 1$ h; 2. $\tau = 0.5$ h; 3. $\tau = 2$ h. (a) Arakawa scheme , (b) Emanuel scheme.

Figure 30 shows the time evolution of the minimum surface pressure using different time-scales for deep convection in the experiment with the Arakawa and Emanuel schemes respectively. It is clear that the Arakawa scheme is more sensitive to the time-scale for the deep convection than the Emanuel scheme. When the time-scale is 2 h, the rapid intensification of the vortex starts 10 h later than in the control calculation, and when time-scale is 0.5 h, the differences of the vortex time evolution are small.

In the Emanuel scheme, the difference in the vortex time evolution for different time scales of the convection scheme is very small because the mass flux above the boundary layer is mainly determined by the equilibrium mass flux M_{c4}^{*}. For this reason the vortex intensification is less sensitive to the time scale than in the Arakawa scheme.

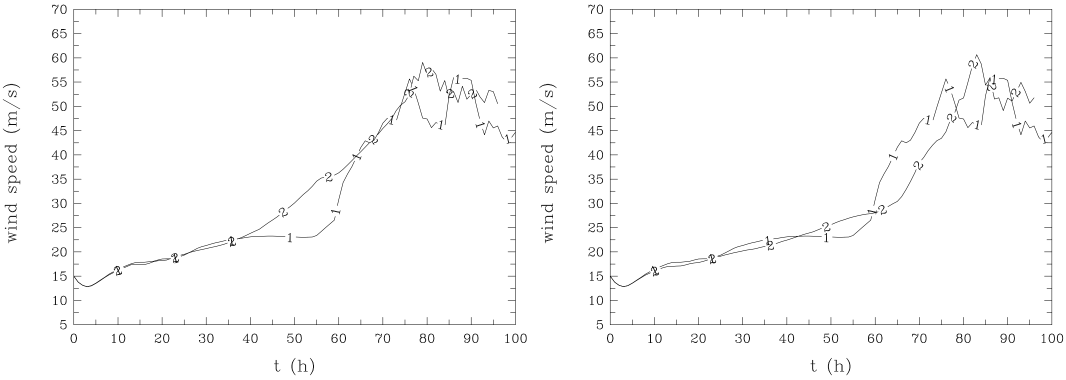

(a) (b)

Figure 31. Evolution of maximum tangential wind speed [in ms^{-1}] in the boundary layer in: (a) Expt. L2A, (b) Expt. L2B, (curves labeled 1) compared with the corresponding control experiments (curves labeled 2).

6.7 Sensitivity to variants of the mass flux formulation in the Emanuel scheme

(a) Expt. M2a. Horizontal entropy advection

In the Emanuel scheme, the equilibrium mass flux at cloud base is determined on the assumption that the downward flux of moist static energy into the subcloud layer balances the local surface flux and the local radial advection of this quantity (see section 3.5, Eq. 36). Here Expt. M2a was carried out to investigate the consequence of excluding the radial advection of moist static energy in this calculation. Figure 31a compares the maximum tangential wind speed in the boundary layer for this experiment with that in the control case, in which the radial advection is included. The differences are small for the first 40 h of integration, but become more noticeable beyond this time. When radial advection omitted, the maximum wind speed curve is smoother and the maximum wind speed is slightly higher, presumably on account of the reduced boundary layer moisture brought about by radial advection in the control case.

(b) Expt. M2b. Horizontal mass flux advection

In Emanuel's (1995a) paper, the actual cloud base mass flux is relaxed to the equilibrium mass flux by

$$\frac{dM_{c4}}{dt} = \frac{M^*_{c4} - M_{c4}}{\tau_{dc}}, \tag{53}$$

where d/dt denotes the material derivative. Here we investigate the difference in vortex evolution when using a local relaxation (Expt. M2b):

$$\frac{\partial M_{c4}}{\partial t} = \frac{M^*_{c4} - M_{c4}}{\tau_{dc}}. \tag{54}$$

Figure 31b compares the maximum tangential wind speed in the boundary layer for Expt. M2b with that in the control case, in which the relaxation is based on the material derivative. Evidently, the method of relaxation has little effect on the vortex evolution during the gestation period, but the use of a local relaxation slightly increases the convective mass flux (figures not shown) because the radial gradient of convective mass flux is negative. This increase leads to a little more drying in the boundary layer, thereby delaying grid-scale saturation and hence the onset of rapid intensification. The delay in the latter is about 6 h. The maximum intensity is about 5 ms^{-1} higher in Expt. M2b than in the control calculation. On the whole, the difference between the two calculations is small. Emanuel (1995a) pointed out that the results are smoother when one uses the material derivative. Therefore it is mainly on numerical grounds rather than a physical considerations to use Eq. 53.

6.8 Summary

Increasing the horizontal resolution of the model has two effects. Firstly it allows air parcels to penetrate further inwards, closer to the radius they would attain if the resolution were unlimited. Because of angular momentum conservation, this leads to a stronger vortex. Secondly, it allows grid-scale saturation to occur earlier, which leads to the earlier onset of rapid intensification. The vortex intensification rate increases significantly as the ratio of the surface energy exchange coefficient to the surface drag coefficient is increased from 0.5 to 1.5 and as the sea surface temperature increases from 26^o C to 29^o C. The inclusion of dissipative heating in the boundary layer makes little difference to vortex evolution during the gestation period, but brings forward the onset time of rapid intensification by about half a day and increases the intensification rate. However there is little difference in the maximum intensity attained. The length of the gestation period is sensitive to the initial vortex strength; reducing the strength from 15 ms^{-1} to 10 ms^{-1} lengthens the gestation period by several days to a week, depending on the treatment of moist processes. Vortex evolution in calculations using the Emanuel closure is less sensitive to the time scale of convection than the Arakawa scheme because the cloud base mass flux is determined mainly by the equilibrium mass flux.

Chapter 7. Effects of vertical differencing

7.1 L-grid, A-grid and CP-grid

The minimal three-layer tropical cyclone model described in the foregoing chapter uses the staggered vertical grid devised by Lorenz (1960), the so-called L-grid, which is widely used in general circulation and numerical weather prediction models. The L-grid has certain desirable attributes: for example, it enables the total energy, the mean potential temperature, and the variance of the potential temperature to be conserved under adiabatic and frictionless processes (Arakawa (1972); Arakawa and Lamb, 1977; Arakawa and Suarez, 1983). However, it has been shown to lead to a computational mode in the vertical distribution of potential temperature (Tokioka, 1978; Arakawa and Moorthi, 1988; Cullen and James 1994; Hollingsworth, 1995; Arakawa and Konor, 1996; henceforth referred to as AK). The same applies to the grid used by Anthes *et al.* (1971) and Anthes (1972), which has been widely used also (subsequently we refer to this grid as the A-grid). AK cautioned that the existence of the computational mode may be serious, especially in the models that include moist processes, since the computational mode can spuriously interact with the physical mode through inherently nonlinear condensation and associated processes. They showed further that the problem could be resolved by using the staggered grid proposed by Charney and Phillips (1953), which they call the CP-grid.

In the L-grid, the (potential) temperature, θ, horizontal velocity, $\mathbf{u}$, and geopotential height, Φ, are stored at the middle of layers, while the vertical velocity is defined at the interfaces between these layers (Fig. 32). AK show that the computational mode arises because of the extra freedom available in the temperature field and typically appears as an oscillation of θ that changes sign from one level to the next. The existence of this oscillation is caused by the fact that, with centered or approximately centered finite differencing, the thickness between two adjacent layers, $\Phi_k - \Phi_{k-1}$ depends on an average of θ between the two layers, i.e. $\theta_{k-1/2} = 0.5(\theta_k + \theta_{k-1})$. It is possible to have a zero vertical distribution of perturbation geopotential ϕ' for a nonzero vertical distribution of perturbation potential temperature θ'. Such a solution, with an alternating or zigzag temperature perturbation between layers, is uncoupled from the dynamical fields of the discrete system, although it may couple with moist processes by its effect on the saturation vapour pressure. AK pointed out that the existence of a computational mode is a property of any Lorenz-type grid in which the horizontal momentum and potential temperature are carried at the same levels.

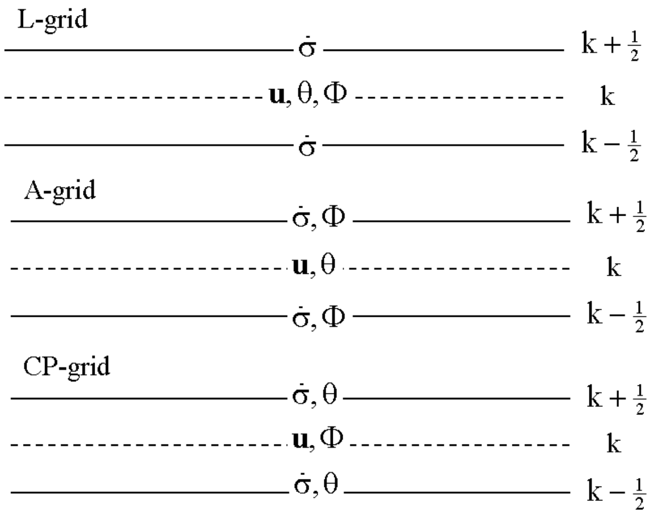

Figure 32. Configuration of σ-levels in the L grid, A-grid and CP-grid models.

Arakawa and Moorthi (1988) showed that use of the L-grid can also reduce the effective static stability and falsely satisfy the necessary condition for baroclinic instability near the lower and upper boundaries.

In the A-grid, Φ is defined at interface levels while the horizontal velocities and potential temperature are stored at the middle of layers. Tokioka (1978) advocated the use of this grid, thinking that the computational mode would be eliminated because the discrete hydrostatic equation does not involve average of potential temperature. However, Arakawa and Moorthi (1988) showed that this is not the case. They noted that for the pressure gradient term in the middle of layers, one still needs to obtain the geopotential height by averaging $\Phi_{k-1/2}$ and $\Phi_{k+1/2}$. The difference $\Phi_k - \Phi_{k-1}$ again depends on an average of θ_k and θ_{k-1} and the computational mode can still appear. Thus the the existence of a computational mode is a feature of any vertical grid in which $\mathbf{u}$ and θ are carried at the same levels, rather than a particular vertical-difference scheme.

AK designed a sigma-coordinate version of the vertical grid used by Charney and Phillips (1953), the structure of which is shown in the lower panel of Fig 32. In the CP-grid, temperature or potential temperature are carried at the interface levels with the vertical σ-velocity, $\dot{\sigma}$, while the horizontal velocity and the geopotential are calculated in the middle of layers as in the L-grid. AK showed that with this configuration the computational mode does not exist because heat can be transferred by the mass flux at the same level. Also the thickness between two adjacent model layers solely depends upon the potential temperature in between, thus precluding a zigzag temperature pattern in vertical. Arakawa and Moorthi (1988) found that with the CP grid, one can easily maintain important dynamical constraints on quasi-geostrophic flow, such as the conservation of quasi-geostrophic potential vorticity through horizontal advection and the resulting integral constraints. In contrast it is not straightforward to define quasi-geostrophic potential vorticity with the L-grid.

7.2 Governing Equations in the CP-grid model

The basic equations in the CP-grid are similar to those of L-grid, which are described in Chapter 2. The L-grid model is based on the three-dimensional hydrostatic primitive equations in sigma-coordinates (x, y, σ) on an f-plane or β-plane, where x and y are in the zonal and meridional directions, respectively, and

$$\sigma = \frac{p - p_{top}}{p_s - p_{top}} = \frac{p - p_{top}}{p^*}, \tag{55}$$

$p^* = p_s - p_{top}$, p_s and p_{top} are the surface and top pressures and p_{top} is a constant, taken here to be 100 mb. Then the upper and lower boundary conditions require that $\dot{\sigma} = 0$ at $\sigma = 0$ and $\sigma = 1$. The zonal and meridional momentum equations and the hydrostatic equation are the same as those in Chapter 2.
The thermodynamic and moisture equations are

$$c_p * \frac{\partial T}{\partial t} = -c_p \left(u\frac{\partial T}{\partial x} + v\frac{\partial T}{\partial y} \right) - c_p\dot{\sigma}\frac{\partial T}{\partial \sigma} + \alpha\omega + Q_\theta \tag{56}$$

and

$$\frac{\partial q}{\partial t} = - \left(u\frac{\partial q}{\partial x} + v\frac{\partial q}{\partial y} \right) - \dot{\sigma}\frac{\partial q}{\partial \sigma} + Q_q \tag{57}$$

where α is the specific volume, Q_θ is the diabatic heat source and Q_q is the moisture source, the last two of which include contributions from surface fluxes. The temperature T is related to θ by

$$T = \left(\frac{p}{p_o} \right)^\kappa \theta = \frac{(p^*\sigma + p_{top})^\kappa}{p_o^\kappa}\theta. \tag{58}$$

where $p_0 = 1000$ mb.

7.3 Vertical differencing in the CP-grid model

The vertically discrete equations are constructed to satisfy the four constraints advocated by Arakawa and Lamb (1977), namely:

- the vertically-integrated pressure gradient force generates no circulation along a contour of the surface topography;

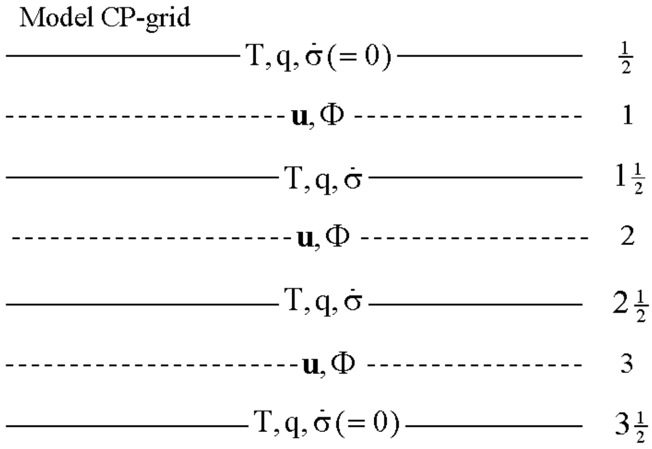

Figure 33. Configuration of σ-levels in the CP-grid model showing locations where the dependent variables are stored. The horizontal velocity, geopotential are calculated at levels 1, 2, and 3, and potential temperature, specific humidity, vertical velocity, $\dot{\sigma}$, are stored at levels $\frac{1}{2}$, $1+\frac{1}{2}$, $2+\frac{1}{2}$, and $3+\frac{1}{2}$

- the energy conversion terms in the thermodynamic and kinetic energy equations have the same form with opposite signs so that the total energy is conserved under adiabatic frictionless processes;
- the global mass integral of the potential temperature is conserved under adiabatic processes;
- the global mass integral of a function of the potential temperature, such as a square of logarithm of the potential temperature, is also conserved under adiabatic processes.

As in L-grid, the model is divided vertically into three unequally deep layers with σ-depths of 3/9, 5/9, 1/9, respectively, from the lowest layer to the top layer (see Fig. 33). Unlike the L-grid, where all the dependent variables, such as horizontal velocity, potential temperature, specific humidity and geopotential, are defined in the middle of each layer (full levels in the Fig. 32), and $\dot{\sigma}$ is staggered, the horizontal velocity, geopotential in the CP-grid are calculated at levels 1, 2, and 3, and potential temperature, specific humidity, and the vertical velocity, $\dot{\sigma}$, are stored at levels $\frac{1}{2}$, $1+\frac{1}{2}$, $2+\frac{1}{2}$, and $3+\frac{1}{2}$. The equations are expressed in finite-difference form in both the horizontal and vertical and integrated forward in time using the Adams-Bashforth third-order method. The discrete equations are based on the scheme formulated by AK and are detailed in the Appendix G.

7.4 Physical processes in the CP-grid and L-grid models

(a) Explicit moist processes

Explicit condensation is treated in a similar way to that in the L-grid model. If at any time the air becomes supersaturated at a grid point, the specific humidity is set equal to the saturation specific humidity and the excess water vapour is condensed to liquid water. This water is assumed to precipitate out while the latent heat released is added to the air. The latent heat raises the air temperature and thereby the saturation specific humidity, requiring a further adjustment of the amount of condensed water, and so on. Four iterations are sufficient in this experiment to determine the final amount of water condensed and latent heat released.

(b) Radiative cooling

A Newtonian cooling term, $-(\theta - \theta_{ref})/\tau_R$, is added to the right-hand-side of the thermodynamic equation to crudely represent the effect of radiative cooling. In this expression θ_{ref} is the initial potential temperature profile of the basic state and τ_R is a radiative time scale. Here τ_R is set to be 10 days, based on radiation calculations in Mapes and Zuidema (1996). This is in contrast to that which has been used in the control experiment, where like other authors (e.g Rotunno and Emanuel, 1987; Emanuel, 1989, 1995a) τ_R has been set to be 12 h. The implications of this change are discussed below.

(c) Surface turbulent fluxes

Following Anthes (1972), the surface drag, in vector notation, is written for the σ-system

$$p^*(F_u, F_v) = -g\frac{\partial \tau^2}{\partial \sigma} \tag{59}$$

where g is the acceleration due to gravity and τ^2 is the vector Reynolds stress. The quadratic stress law with the surface wind speed approximated by the speed at level-4 is employed for the stress at $\sigma = 1$. Therefore the surface drag is:

$$p^*(F_u, F_v) = \frac{-g\rho^* C_D |\mathbf{v_3}| \mathbf{v_3}}{\delta\sigma_3} \tag{60}$$

where $\mathbf{v}$ is the horizontal wind vector. The drag coefficient, C_D is defined to be 3×10^{-3}, and the surface density, ρ^*, is set to a standard value of 1.10 kg m^{-3}.

For the CP-grid, the sensible and latent heat fluxes at the air sea interface are given by

$$\begin{aligned} p^* F_q &= \frac{g C_E |\mathbf{v_3}| \rho^* (q^*_{sea} - q_{3\frac{1}{2}})}{0.5 \delta\sigma_3}, \\ p^* F_{SH} &= \frac{g c_p C_E |\mathbf{v_3}| \rho^* (T_{sea} - T_{3\frac{1}{2}})}{0.5 \delta\sigma_3} \end{aligned} \tag{61}$$

where F_q and F_{SH} are the latent and sensitive heat fluxes added per unit mass at level $3\frac{1}{2}$. The exchange coefficient, C_E, is assumed to be the same as C_D. q^*_{sea} and T_{sea} are the saturation sea surface mixing ratio and the sea surface temperature, which is taken to be 28°C. Because $T_{3\frac{1}{2}}$ represents the average temperature between level-3 and level-$3\frac{1}{2}$, the sensible and latent heat fluxes are averaged over half the depth of the boundary layer.

The sensible and latent heat fluxes for the L-grid model at the midlevel of the boundary layer are calculated from the formulae:

$$\begin{aligned} p^* F_q &= \frac{g C_E |\mathbf{v_3}| \rho^* (q^*_{sea} - q_3)}{\delta\sigma_3}, \\ p^* F_{SH} &= \frac{g c_p C_E |\mathbf{v_3}| \rho^* (T_{sea} - T_{surface})}{\delta\sigma_3}. \end{aligned} \tag{62}$$

As in Anthes (1972)'s formulation, the contributions from F_q and F_{SH} are used to increase the entropy in the boundary layer. It is assumed that the boundary layer is well mixed, so that the mixing ratio and potential temperature are uniform vertically within the boundary layer. Therefore q_3 is used to represent the surface layer mixing ratio, and $T_{surface}$ is calculated at a level 3.30 mb above the surface.

7.5 Comparison of results with the CP-grid and L-grid

We compare here the results of two calculations on the f-plane, one using the L-grid and the other using the CP-grid. The vertical differencing in the L-grid model is based on the method proposed by Arakawa and Suarez (1983) and is described in Chapter 2. For simplicity, the calculations use only the explicit representation of moist processes as described in Chapter 2.

Figure 34 compares the maximum wind speed in the boundary layer for the two calculations and would appear to indicate that vortex evolution in the two calculations

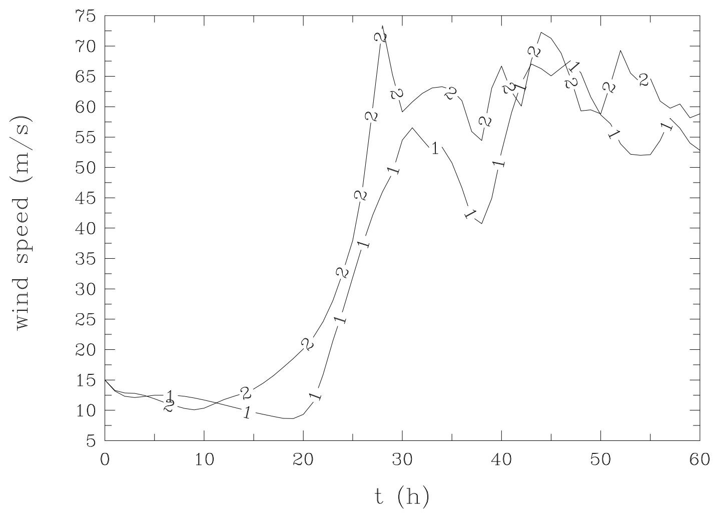

Figure 34. The maximum wind speed in the boundary layer in the calculations with the L-grid (curve labelled 1) and CP-grid (curve labelled 2).

is quite similar. With the CP-grid, the vortex begins to intensify about 10 h earlier than with the L-grid on account of the earlier saturation in the core region. In the mature stage, the maximum wind speed is about 5 m s^{-1} larger than with L-grid, but the fluctuations in intensity are larger in the latter case. The differences during the mature stage can be attributed to the difference in the asymmetries that develop in the two calculations (see section 7.5 (b) below). More detailed comparisons of the two calculations are discussed below.

The processes involved in the vortex evolution using the L-grid are discussed at length in Chapter 4., only the salient features are described here. During the gestation period, which lasts for about 24 h, the vortex slowly decays on account of the frictionally-induced divergence in the lower troposphere (middle layer) and the associated ascent leads to a cooling and moistening of the middle and upper layers in the core region. Eventually, saturation occurs on the grid-scale in the inner core region through the depth of the troposphere and the accompanying latent heat release creates positive buoyancy. In turn, the buoyancy leads to convergence in the middle layer, dominating the frictionally-induced divergence that would be induced by friction in this region in the absence of significant buoyancy. The period of rapid deepening, between 24 h and 30 h, begins with the occurrence of grid-scale saturation. A similar pattern of evolution occurs in the calculations with the CP-grid, but there are notable differences in the temperature fields that develop in the two calculations and in the asymmetries. We examine these differences in the next two subsections.

(a) Temperature field

Figure 35 compares time-radius plots of the azimuthally-averaged potential temperature deviation at the three model levels at which the temperature is predicted in the two calculations (note that these levels are a little different in the two grids). We consider first the calculation for the L-grid (left panels in Fig. 35). After 30 h, the vortex reaches a mature stage with a warm core in the upper and middle layers (positive potential temperature deviation). The highest temperature anomaly is about 16°C at 48 h in the top layer and about 6°C in the middle layer. After the vortex reaches maturity at about 30 h the warm anomaly in the top layer extends progressively outwards on account of radial advection in this layer: for example, the 8°C temperature contour reaches a radius of 350 km after 60 h. A striking feature of the calculation is that during the same period, a cold anomaly forms in the middle layer in an annular region from 100 km - 300 km, with a corresponding warm anomaly in the boundary layer. These anomalies spread outwards at about the same rate as the warm anomaly in the upper layer. Note also that the warming in the middle layer in the core region is accompanied by cooling in the boundary layer. This zigzag pattern in the potential temperature anomaly during the mature stage is reminiscent of the behaviour of the computational mode in temperature described by AK and it begins to develop when latent heat release occurs. Additional support for the hypothesis that these structures are a manifestation of the computational mode is provided by an examination of the corresponding vertical velocity fields.

The left panels of Fig. 36 show the evolution of the azimuthally-averaged vertical $\sigma-$velocity ($\dot{\sigma}$) at levels $1+\frac{1}{2}$ and $2+\frac{1}{2}$ for the L-grid calculation. Ascent in the core region (the innermost 100 km) increases rapidly after 24 h, and there is comparatively weak subsidence outside this region and along the axis, the latter indicating the attempt of the model vortex to form an eye-like feature, despite the relatively coarse radial grid-spacing of 20 km. The negative temperature tendency in the middle layer outside the core region is inconsistent with the subsidence that occurs there and is a strong indication that the computational mode is involved.

The temperature fields in the calculation with the CP-grid (right panels of Figs. 35) have a similar structure to those with the L-grid during the gestation period, but, as noted above, grid-scale saturation and vortex intensification occur 10 h earlier in this case. As the vortex starts to rapidly intensify, the warm potential temperature anomaly at all three levels remains mainly in the core region, within a radius of 150 km, and does not spread out in the top layer as it does with the L-grid. Moreover, there is no indication of any zigzag pattern in its vertical structure. The vertical velocity field in this case (left panels of Figs.35) is quite similar to that in L-grid, but now the temperature field is consistent with the vertical motion.

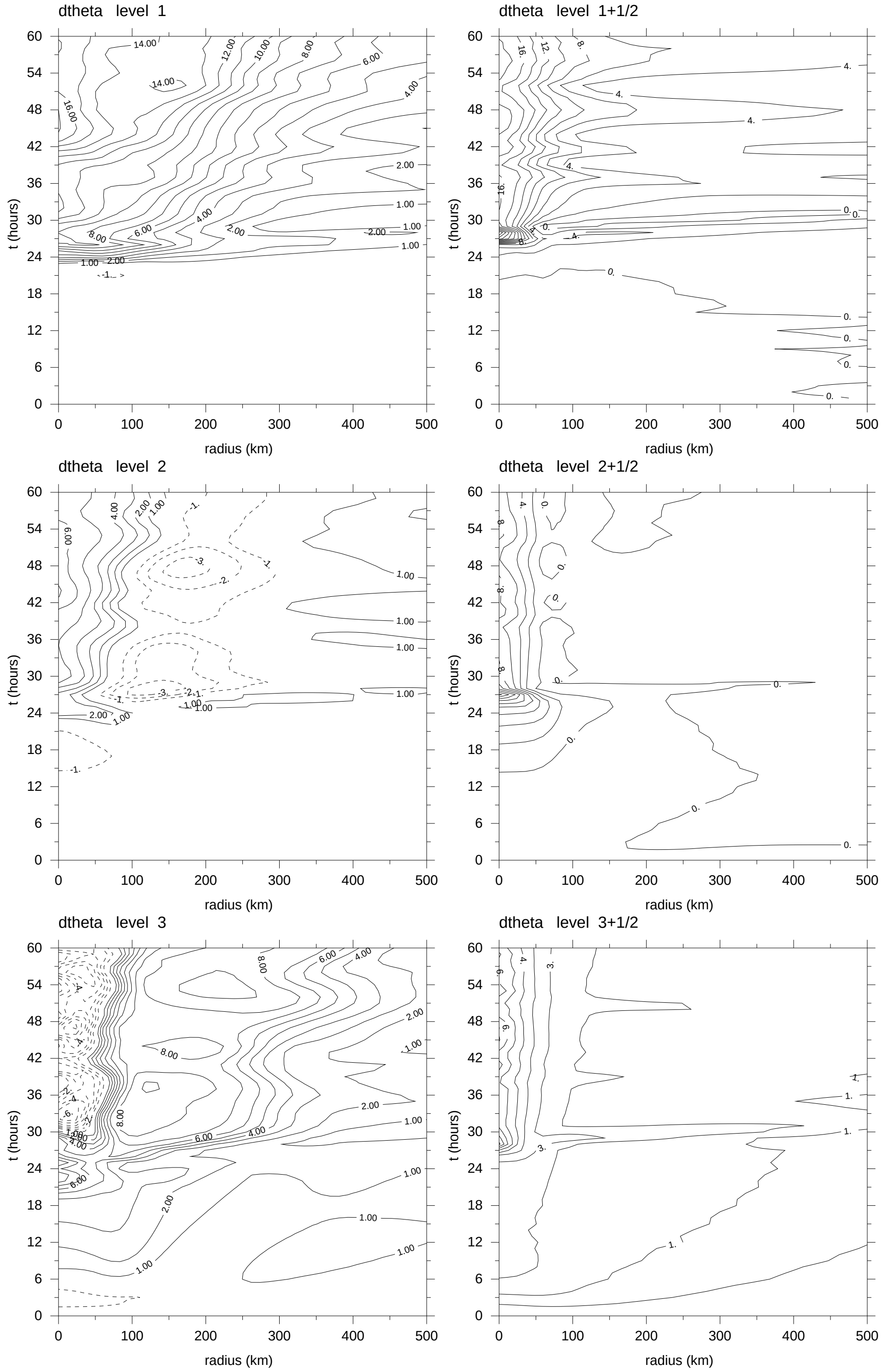

Figure 35. Potential temperature deviation in the top, middle and boundary layers (levels 1, 2 and 3, respectively) of the calculations with the L-grid (left panels, contour intervals are 1 ^{o}C)) and at levels $1\frac{1}{2}$, $2\frac{1}{2}$ and $3\frac{1}{2}$ in the calculations with the CP-grid (right panels, contour intervals are 2 ^{o}C for the levels $1\frac{1}{2}$, $2\frac{1}{2}$ and 1 ^{o}C for the level $3\frac{1}{2}$)

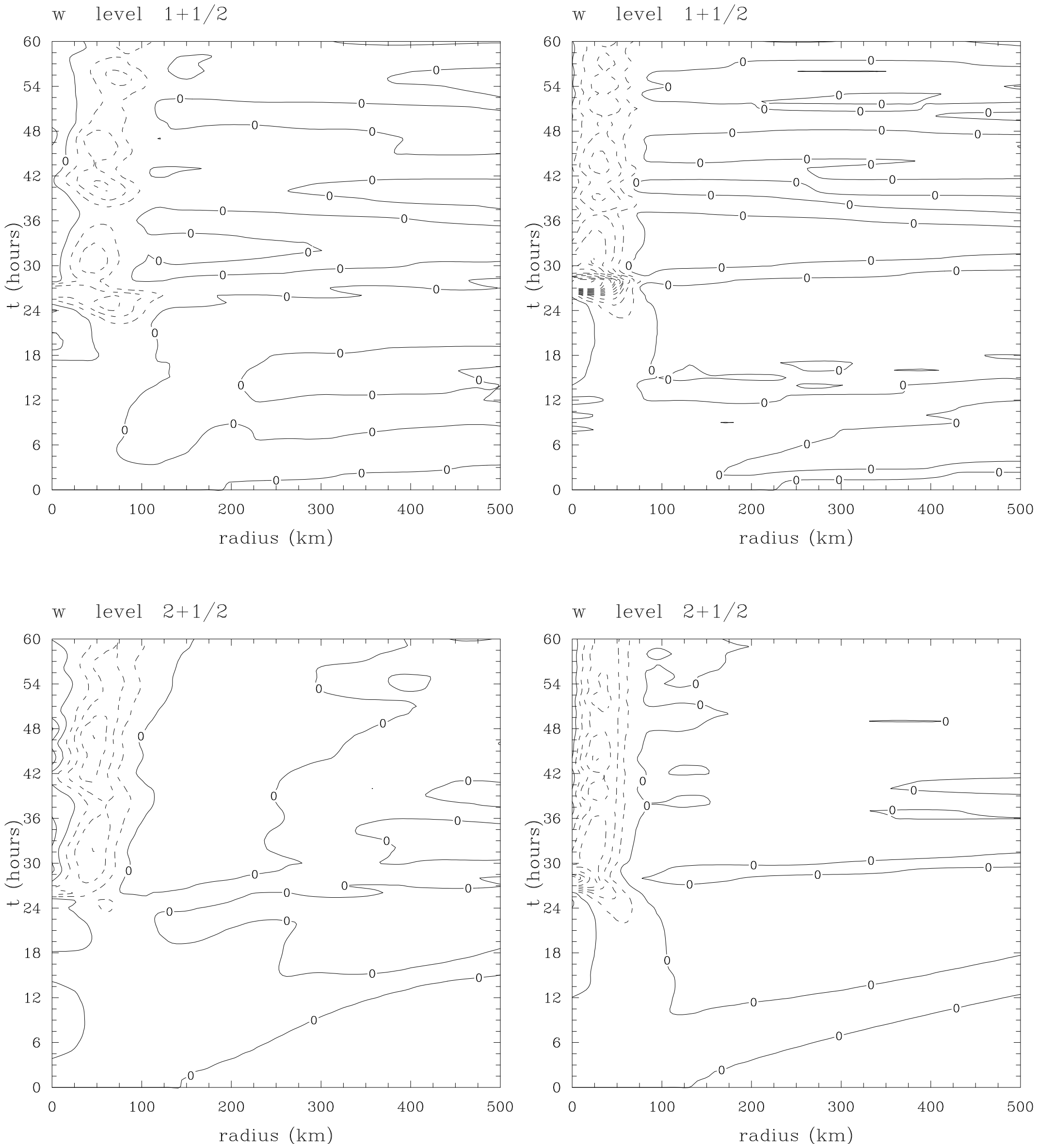

Figure 36. $\dot{\sigma}$ in the layers of 1+1/2 and 2+1/2. Contour interval is $4 * 10^{-5}/s$. The left panel is the calculation with L-Grid, and the right panel is that with CP-Grid.

Despite the evidence presented for the existence of a computational mode in the temperature field in the calculation with the L-grid, the effect of this mode is small until condensation and heat release occurs in the core region. Therefore the results presented here do not detract from the principal results obtained in Chapter 4-6, which focus mainly on the earlier periods of evolution. However, they have major implications for using the L-grid model (and its forerunners discussed earlier) for studies of the mature

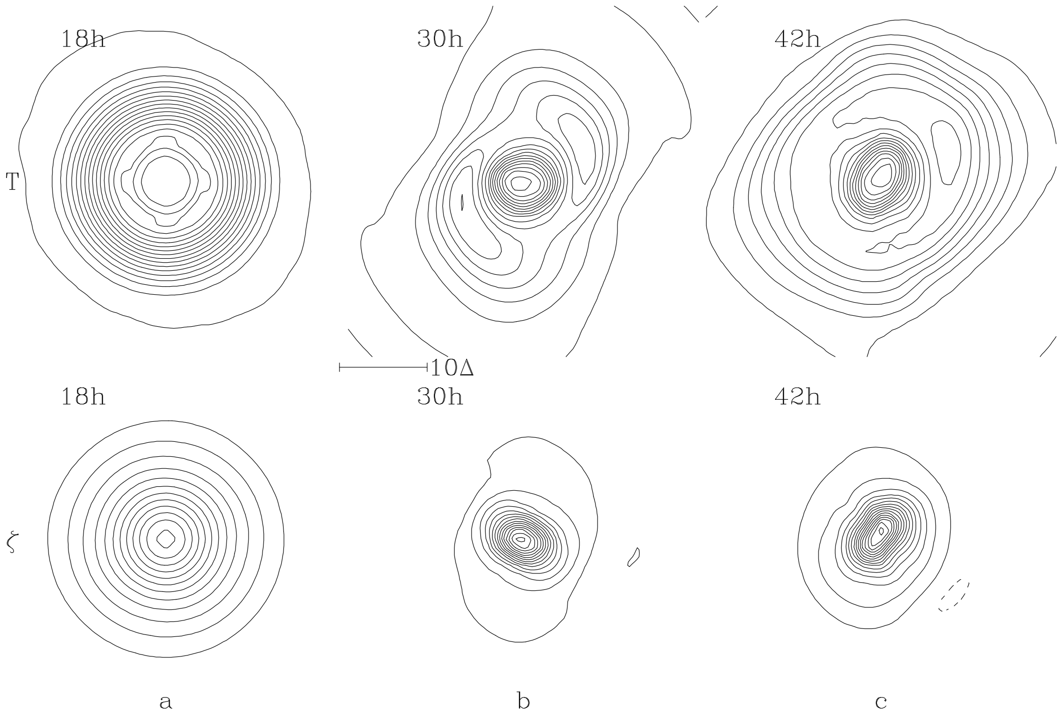

Figure 37. The temperature and vorticity structure in the middle layer at t = 18 h, 30 h, and 42 h in the calculation with the L-Grid. The contour intervals for the temperature field are 5.0* 10^{-2}, 5.0*10^{-1}, and 5.0*10^{-1} at t = 18 h, 30 h, and 42 h respectively. The contour intervals for the vorticity field are 2.0* 10^{-5}, 1.0*10^{-4}, and 1.0*10^{-4} at t = 18 h, 30 h, and 42 h respectively.

stage of a tropical cyclone.

(b) Development of asymmetries

Chapter 4. showed that the fluctuations in vortex intensity during the mature stage of development are associated with pronounced asymmetries of the vortex that begin to form when the vortex starts to rapidly intensify. A preliminary study of these asymmetries indicates that their structure depends, *inter alia*, on the particular convection scheme chosen for the calculations. I show here that the asymmetries are, indeed, strongly influenced by the choice of vertical grid, a finding that is likely to be true of the asymmetries in other calculations, such as those of Anthes (1972) and Kurihara and Tuleya (1974).

Figures 37 and 38 show the development of the asymmetries in the temperature and vorticity fields at the three chosen times in the middle layer for the calculations with the L-grid and CP-grid. One common feature in both calculations is the azimuthal

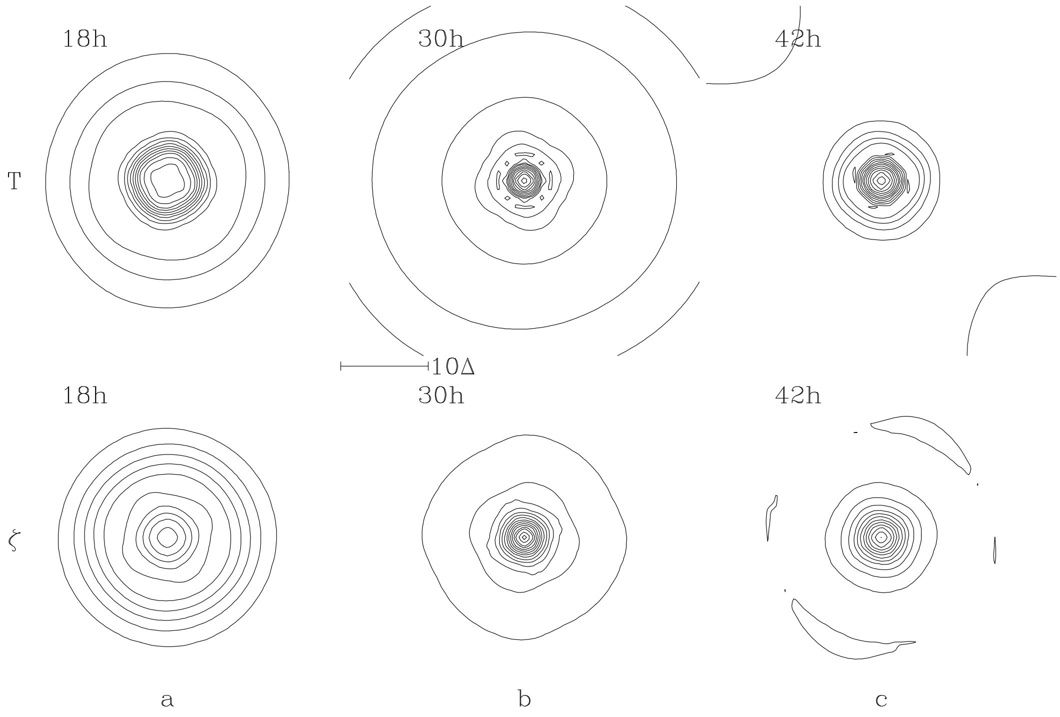

Figure 38. The temperature and vorticity structure at t = 18 h, 30 h and 42 h in the calculation with the CP-Grid. The contour intervals for the temperature field are $2.0*10^{-1}$, $5.0*10^{-1}$, and $5.0*10^{-1}$ at t = 18 h, 30 h, and 42 h respectively. The contour intervals for the vorticity field are $2.5*10^{-5}$, $2.5*10^{-4}$, and $2.0*10^{-4}$ at t = 18 h, 30 h, and 42 h respectively.

wavenumber-4 pattern about the vortex centre that begins to emerge prior to the period of rapid intensification. I hypothesize that the emergence of this asymmetry is associated with the representation of an axisymmetric flow on a square grid, a result supported by the calculations of Nguyen *et al* (2002). At 18 h in Fig. 37a, both the temperature field and vorticity field are quite symmetric about the domain centre, except inside a radius of about 100 km, where a wavenumber-4 pattern is evident. Figure 37b shows that there are obvious wavenumber-2 asymmetries in both temperature and vorticity field at 30 h in this calculation. It is clear that in the temperature field the wavenumber-2 asymmetry appear as two low centers outside of the warm core. I noted in section 7.5(a) that a cold temperature anomaly forms in the middle layer outside of the core region when the vortex starts to rapid intensify. Figure (37c) shows that the asymmetry at 42 h is similar to that at 30 h, but by this time the asymmetry has formed a wavenumber-1 component. A linear stability analysis of the initial wind profile by the method of Weber and Smith (1994) shows that it is barotropically unstable to a disturbances of azimuthal wavenumber-2, but the e-folding time scale of this mode is on the order of 66 h, while the wavenumber-2 asymmetry in the L-grid calculation starts at the same time when the vortex core saturates, which is about 24 h. Therefore it is possible that the zigzag pattern of the temperature field associated with the computational mode in the L-grid is responsible for inducing the wavenumber-2 asymmetry instead of the dynamic instability, and also the zigzag pattern of the temperature would contribute to communicating the wavenumber-2 asymmetry downwards to the lower layers. In contrast, with the CP-grid, the vortex is quite symmetric and a wavenumber-4 asymmetry predominates during the gestation and rapid intensification stages. In this calculation, the positive potential temperature anomalies remain essentially in the core region, and the amplitude of the wavenumber-2 component of asymmetry is much less than in the case of the L-grid.

Anthes (1972) and Kurihara and Tuleya (1974) studied also the development of asymmetries in calculations for an initially axisymmetric vortex on an f-plane in an environment at rest. Both these studies employed the A-grid described in section 2. As in the foregoing L-grid calculation, they found that azimuthal wavenumber-4 asymmetry is the main feature in the early stage of development and that wavenumber-2 asymmetries appear when the grid-scale latent heat release occurs. Anthes (1972) found that during the early (symmetric) stage, the variance of any quantity is small and that wavenumber-4 accounts for nearly all the variance. He attributed this asymmetry to artificial aspects of the irregular boundary in his model. At a later stage, with the rapid growth of the variance, wavenumbers-1 and -2 became dominant and accounted for most of the variance. Anthes (1972) showed that the mechanism for the growth of the eddies is the barotropic conversion of mean azimuthal kinetic energy to eddy kinetic energy. Kurihara and Tuleya (1974) found that baroclinic as well as barotropic energy conversion is an energy source for the asymmetries in their model. Both of Kurihara and Tuleya (1974) and Anthes (1972) investigated the spiral rain bands that form in the mature stage of their model tropical cyclones. These bands rotate cyclonically about the storm center while propagating outwards. Both authors considered these to be internal gravity waves modified by latent heat release, but both admitted that the mechanism for the spiral bands is unknown, noting that there does seem to be an interesting, although obscure, relationship between the bands and the asymmetries. Kurihara and Tuleya (1974) plotted the distribution of temperature at the mature stage, which shows that the front part of the band is relatively warm, while the rear part of the band is cold. The situations in the upper troposphere are opposite to that in the lower levels. Arakawa and Moorthi (1988, p1692) pointed out that the computational mode in temperature is still present with the A-grid, a fact that raises the possibility that the wavenumber-2 and wavenumber-1 asymmetries in Anthes and Kurihara *et al.* 's studies are associated with the computational mode in temperature.

(c) Radiative cooling effects

The excellent discussion of radiative effects in tropical cyclones by Anthes (1979) indicates that the radial extent of the secondary circulation of a mature tropical cyclone may be expected to be strongly influenced by radiative cooling in the surrounding clear-air environment. In their model, Rotunno and Emanuel (1987) assume a Newtonian relaxation rate, $\tau = 12$ h, which yields a cooling rate in the outer regions of approximately 2 K d^{-1}. They argue that this is enough to balance the gentle, but persistent subsidence in the outer regions of the vortex. The same value for τ was used by Emanuel (1989, 1995a). Rotunno and Emanuel note, however, that with this value, the cooling rate becomes unrealistically large in the central region where potential temperature becomes significantly larger than the reference value. Both Rotunno and Emanuel (1987) and Emanuel (1989) carried calculations with less radiative cooling and without it completely, and found that the vortex expands to a larger radius compared to the control runs.

Some authors would claim that this value of τ is too large, for example the study by Mapes and Zuidema (1996; see Fig. 15b) suggests that the time scale for Newtonian cooling is about 10 d, which is the time scale chosen by Arakawa and Moorthi (1988). For this reason we chose $\tau = 10$ d in this paper.

The left panels of Fig. 39 show the potential temperature deviation at level 1 and 2 in the calculation with the L-grid when τ is set to be 12 h (cf. Fig. 35, two upper left panels). It is clear that the radial spread of the temperature anomaly in the top layer is less than in the case where $\tau = 10$ d. For example, the 8^{o}C temperature anomaly contour is at about 150 km after 60 h of integration, compared with about 300 km in the calculation with $\tau = 10$ d. As a result, the cold temperature anomaly between the radius of 100 km-200 km in the middle layer is less than in the case where $\tau = 10$ d. Therefore the strong radiative damping suppresses the computational mode in the L-grid model. It should be noted that Rotunno and Emanuel (1987)'s model uses the L-grid as well. Therefore, it is possible that the radial expansion of the vortex in their calculation without radiation cooling is also associated with the computational mode in the temperature field, which makes it necessary to have a strong radiative cooling to keep the vortex from expanding.

In contrast, the time-scale for the radiative cooling has less effect on the vortex evolution in the CP-grid model. Like the left panels of Fig. 39, the right panels show the potential temperature deviation at the level $1+\frac{1}{2}$ and $2+\frac{1}{2}$ in the calculation with the CP-grid when τ is set to be 12 h. Comparing with Fig. 35 (two upper right panels), the warm core at the top layer is reduced by the stronger radiative cooling, and there

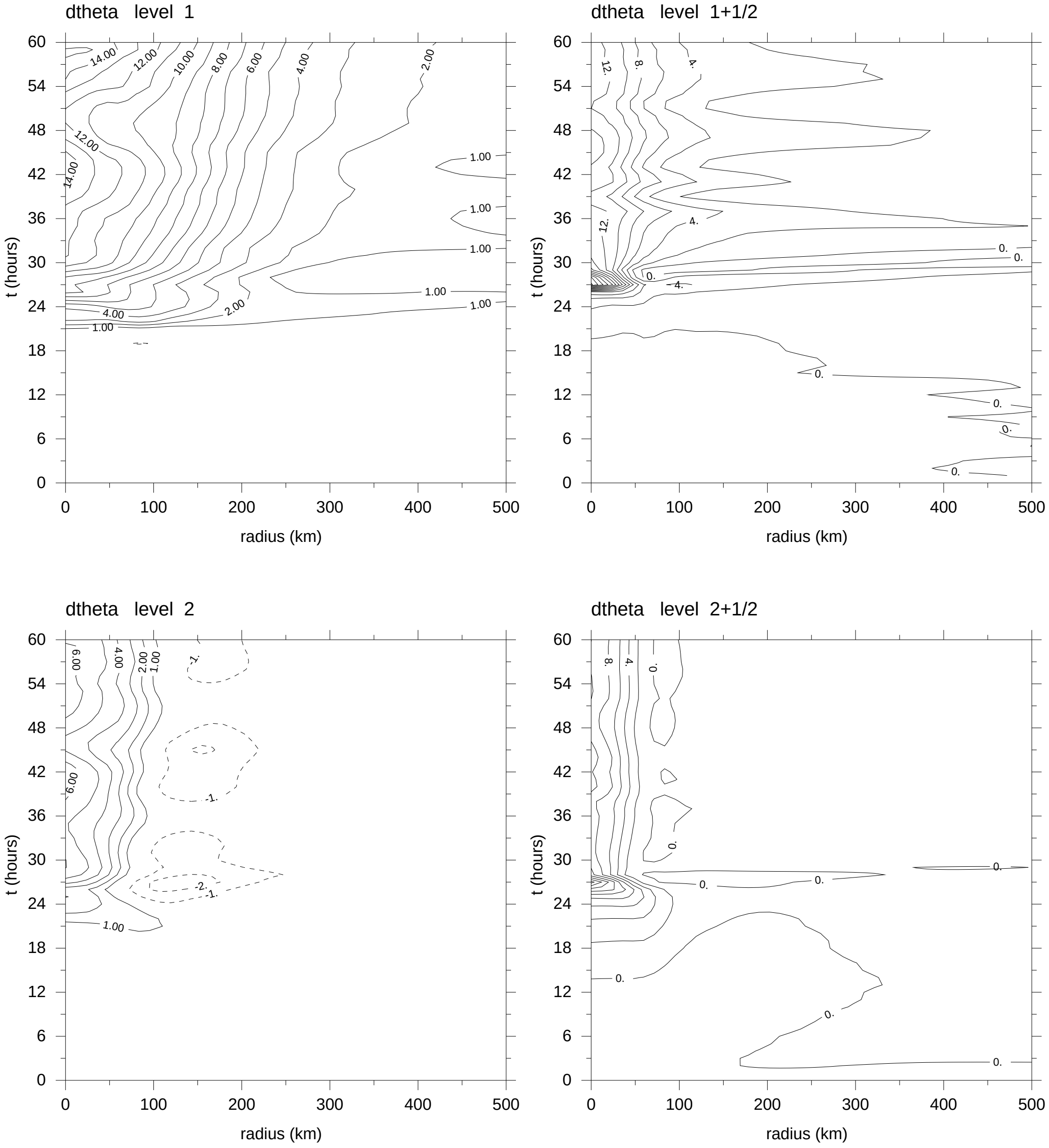

Figure 39. Potential temperature deviation at the level-1 and -2 for the calculation with L-Grid (left panel) level-1+1/2 and -2+1/2 for the calculation with L-Grid (right panel), and τ=12h (Compare with Fig. 35)

is no obvious difference in the radial spread of the temperature.

7.6 Summary

The minimal tropical cyclone model has been reformulated on a Charney-Phillips vertically-staggered grid and the results of calculations with a simple explicit representation of moist processes have been compared with those of the original model, which employs the Lorenz-grid. While there is not much difference between the two calculations during the early stages of evolution, the calculation on the L-grid shows evidence of the development of the computational mode in temperature when latent heat release occurs in the inner core of the developing vortex. The existence of this mode raises questions about aspects of the vortex structure during the mature stage of development as well as the structure of the asymmetries that develop during this stage. The same questions could be raised concerning the results of some earlier studies of the evolution of asymmetries in tropical cyclones where the models used employ a vertical-staggered grid that also permits a computational mode in temperature.

Use of the CP-grid with the conservative finite-difference scheme worked out by Arakawa and Konor (1996) appears to avoid the problems of the L- and A-grids and the asymmetries that form during the mature stage of development are more consistent with expectations in a flow on an f-plane emerging from axisymmetric initial conditions, assuming that dynamical instabilities are not involved. Weak azimuthal wavenumber-4 asymmetries are present during the gestation period in both models and appear to be related to the representation of a circular flow on a square grid as the initial vortex profile, at least, is barotropically stable to this wavenumber. In the L-grid model, an azimuthal wavenumber-2 pattern develops during the period of rapid intensification as the zigzag temperature pattern appears out of the core region and later, the asymmetry acquires wavenumber-1 components as has been seen in some of the earlier calculations. With the CP-grid, the warm core is much more confined and the wavenumbers-1 and -2 components that develop later in the integration are much weaker in amplitude.

Chapter 8. Model appraisal

The development of the present model has been motivated by the desire to isolate the minimum components required to produce a realistic hurricane-like vortex in a three-dimensional configuration with a fully-integrated (albeit highly simplified) representation of moist physics. The benefits of such a model are that it may be simple enough to provide insights into some aspects of the complex interactions that occur between moist convection and the larger-scale vortex circulation in a variety of situations. Inevitably, simplicity is achieved at the expense of accuracy in the quantification of some processes. The hope is that the levels of inaccuracy do not affect the broad conclusions that are drawn from the model, but the extent to which this is the case may only be fully checked by a comparison with results of similar calculations using more complex models. Some specific limitations of the current model are considered below.

(i) The representation of explicit latent heat release as a pseudo-adiabatic process is an extreme oversimplification and will overestimate the buoyancy in the inner-core convection during the rapidly-developing stage through its neglect of water loading and mixing with the environment, except for the mixing due to model diffusion. However, the fact that the peak intensity of the model vortex is reasonable implies that the buoyancy distribution produced by the explicit release of latent heat is also within a range that is reasonable.

(ii) It might be argued that, on account of the nonlinear variation of specific humidity with pressure (or σ) in the tropical atmosphere, the vertical advection of water vapour may be subject to large error in a model with only three vertical layers as used here. This may be an issue during the relatively short period of time that a grid column takes to saturate, but when saturation is achieved, all that matters is that the thermodynamic profile within the column is close to a moist adiabat with $h_b = h_3^* = h_1^*$. This state is achieved by the present scheme.

(iii) The time at which grid-scale saturation occurs can be expected to be a function of the horizontal and vertical resolution. Indeed, a calculation with only explicit moisture process in which the grid spacing was halved to 10 km reduced the onset time of rapid deepening by about 12 h. The dependence on horizontal resolution in particular must be a concern of *all* models that incorporate both explicit and implicit representations of moist physics and especially those which are designed with a view to forecasting tropical-cyclone intensity change. A similar experiment with five vertical layers in which only the explicit moisture process is included showed also a reduction in the time of grid-scale saturation and the onset of rapid deepening by about 10 h. An in-depth discussion of the issues involved in representing moist processes on the mesoscale is the subject of review papers by Molinari and Dudek (1992) and Kuo *et al.* (1997).

(v) Convective downdrafts are generally unsaturated and lower the moist static energy of the boundary layer (Betts, 1976, p1019). Thus the downdrafts in this paper are too moist and too cold, but their qualitative effect on the moist static energy of the boundary layer would not change if a degree of sub-saturation were allowed.

(vi) All the convection schemes considered here are based on a steady state cloud model that transports boundary-layer air to the upper troposphere. In reality, as convective systems mature, they develop a different mean structure in which there is mesoscale subsidence in the lower troposphere and mesoscale ascent in the upper troposphere. In a more complete theory, this change in structure ought to be taken into account (see e.g. Betts, 1997).

(vii) The convection schemes assume that convective updrafts occupy only a small fraction of a grid column, whereas explicit convection occurs only when an entire grid cell is saturated. The gap between these two extreme situations needs to be filled. This might be done, for example, by introducing a prognostic equation for the fractional area of cloud in a grid box.

(viii) It might be a little more realistic to initialize the calculations with a baroclinic vortex somewhat weaker than the one used here, although many authors have chosen an initial vortex similar in strength to mine as this enhances the surface energy fluxes and thereby reduces the gestation period (and hence the computational time).

Chapter 9. Summary and conclusions

We have developed a minimal three-dimensional numerical model for a tropical cyclone in which dynamical and thermodynamical processes are closely interlinked through explicit and parameterized representations of moist processes. Like most other models, the present one is capable of simulating the development of a mature hurricane-like vortex from an existing vortex of tropical depression intensity in a maritime environment where the sea-surface temperature is high. In my case, the environment is slightly *stable* to deep cumulus convection at the initial instant.

Vortex intensification is characterized by a gestation period of between half a day and two and a half days, depending on which cumulus parameterization scheme is implemented, followed by a period of rapid intensification lasting on the order of twelve hours. Intensification occurs irrespective of the implementation of a cumulus parameterization scheme and in all calculations, the period of rapid deepening begins when grid-scale saturation occurs in the inner core region. With the modified Arakawa or Emanuel parameterization schemes, in which the cloud-base mass flux of deep convection is not related to the boundary-layer convergence, the period of rapid intensification begins later than in the cases with explicit convection only, or with the modified Ooyama scheme. While deep convection produces enhanced buoyancy in the inner region in the early stages of development, the associated intra-cloud downdrafts not only warm, but also dry the boundary layer and middle troposphere. The drying delays the time at which saturation occurs on the grid scale and opposes the convective destabilization of the boundary layer caused principally by surface moisture fluxes in regions of strong boundary-layer wind speeds. With the Ooyama scheme, some boundary-layer convergence occurs in a region where the atmosphere is conditionally stable and the associated moistening of the lower troposphere leads rapidly to saturation on the grid scale. As a result, the period of rapid intensification begins earlier than in the case with explicit convection only.

In the model, as in reality, shallow convection transports air with low moist static energy from the lower troposphere to the boundary layer, stabilizing the atmosphere not only to itself, but also to deep convection. Also it moistens and cools the lower troposphere. For realistic parameter values, the stabilization in the vortex core region is the primary effect: it reduces the deep convective mass flux and therefore the rate of heating and drying in the troposphere. This reduced heating, together with the direct cooling of the lower troposphere by shallow convection, diminishes the buoyancy in the vortex core and thereby the vortex intensification rate.

The effects of precipitation-cooled downdrafts depend on the closure scheme chosen for deep convection. In the two closures in which the deep cloud mass flux depends on the degree of convective instability, the downdrafts do not change the total mass flux of air that subsides into the boundary layer, but they carry air with a lower moist static energy into this layer than does subsidence outside downdrafts. As a result they decrease the rate of intensification during the early development stage. Nevertheless, by reducing the deep convective mass flux and the drying effect of compensating subsidence, they enable grid-scale saturation, and therefore rapid intensification, to occur earlier than in calculations where they are excluded. In the closure in which the deep cloud mass flux depends on the mass convergence in the boundary layer, downdrafts reduce the gestation period and *increase* the intensification rate.

Convective momentum transport as represented in the model weakens both the primary and secondary circulations of the vortex. However it does not significantly reduce the maximum intensity attained after the period of rapid development. The weakening of the secondary circulation impedes vortex development and significantly prolongs the gestation period.

Increasing the horizontal resolution of the model has two effects. Firstly it allows air parcels to penetrate further inwards, closer to the radius they would attain if the resolution were unlimited. Because of angular momentum conservation, this leads to a stronger vortex. Secondly, it allows grid-scale saturation to occur earlier, which leads to the earlier onset of rapid intensification. The vortex intensification rate increases significantly as the ratio of the surface energy exchange coefficient to the surface drag coefficient is increased from 0.5 to 1.5 and as the sea surface temperature increases from 26^o C to 29^o C. The inclusion of dissipative heating in the boundary layer makes little difference to vortex evolution during the gestation period, but brings forward the onset time of rapid intensification by about half a day and increases the intensification rate. However there is little difference in the maximum intensity attained. The length of the gestation period is sensitive to the initial vortex strength; reducing the strength from 15 ms^{-1} to 10 ms^{-1} lengthens the gestation period by several days to a week, depending on the treatment of moist processes. Vortex evolution in calculations using the Emanuel closure is less sensitive to the time scale convection than the Arakawa scheme because the cloud base mass flux is determined mainly by the equilibrium mass flux.

The minimal three-layer tropical cyclone model has been reformulated with a Charney-Phillips grid (CP-grid) in the vertical instead of the Lorenz grid (L-grid) that was used in the original model. Arakawa and Konor have shown that the popular L-grid supports a computational mode in the temperature field that can lead to inaccuracies, especially when moist processes are involved. Here we have compared calculations of the minimal model using the L-grid and CP-grid. We presented evidence that the computational mode is excited in the L-grid model during the period of rapid vortex intensification, which occurs when grid-scale latent heat release occurs in the core region. Thus it would appear that the solution in the mature stage of evolution is contaminated by this mode. We have shown also that the vortex asymmetries that develop during the mature stage are sensitive to the choice of vertical grid and argue that those that occur in the CP-grid formulation are more realistic. It is possible that the computational mode is a spurious feature of many earlier studies of asymmetries in tropical cyclone models in which moist processes are represented.

Appendix A

The initial sounding data

TABLE 5. The initial pressure (p), temperature (T), specific humidity (q), and geopotential height (Φ) in the middle of each layer and at the boundaries between layers in the far field.

σ	p (mb)	q (g/kg)	T (°K)	$\Phi(m^2 s^{-1})$
$\sigma_1 = 1/6$	252.5	0.01	230.4	106549
$\sigma_2 = 1/3$	405.0	0.15	256.1	73557
$\sigma_3 = 11/18$	659.2	4.82	278.9	36066
$\sigma_4 = 8/9$	913.3	13.6	293.8	9098
$\sigma_b = 17/18$	964.2	13.9	297.0	4461

Appendix B

Some details of the numerical method

The Adams-Bashforth third-order scheme is used with a time step of 15 min, i.e.,

$$U^{(n+1)} = U^{(n)} + (\tfrac{23}{12}F^{(n)} - \tfrac{16}{12}F^{(n-1)} + \tfrac{5}{12}F^{(n-2)})\Delta t,$$

where the $F^{(n)}$ are the tendencies of $U^{(n)}$. Horizontal (x, y)-plane derivatives are evaluated on a nonstaggered grid. Second-order finite differences are used in all runs. The standard advection scheme uses third-order upwinding based on standard third-order approximations for the derivatives, which involve 4 grid points with 2 in the upwind direction and 1 in the downwind direction.

We adopt the method of Arakawa and Suarez (1983) for treating the vertical difference scheme and the hydrostatic equation. For convenience, we use half- integer subscripts $\frac{1}{2}$, $1+\frac{1}{2}$, $2+\frac{1}{2}$, $3+\frac{1}{2}$ to represent the top level ($\sigma = 0$), the two interface levels and the bottom level ($\sigma = 1$). The increment in σ is given by

$$\Delta\sigma_k = \sigma_{k+1/2} - \sigma_{k-1/2}.$$

For any variable A that is carried at the k th-level, the flux form can be written:

$$\frac{\partial(p^* A_k)}{dt} + \nabla \cdot (p^* A_k V_k) + \frac{1}{\Delta\sigma_k}\left[(p^*\dot{\sigma})_{k+1/2}\hat{A}_{k+1/2} - (p^*\dot{\sigma})_{k-1/2}\hat{A}_{k-1/2}\right] = 0.$$

This form guarantees that the global average of A will be conserved as a result of advection. This equation can be rewritten in advection form using the continuity equation, which is consistent with the flux form and gives the expression:

$$(\frac{\partial}{\partial t} + V_k \cdot \nabla)A_k + \frac{1}{\Delta\sigma_k p^*}\left[(p^*\dot{\sigma})_{k+1/2}(\hat{A}_{k+1/2} - A_k) + (p^*\dot{\sigma})_{k-1/2}(A_k - \hat{A}_{k-1/2})\right] = 0.$$

In the case of wind speed and specific humidity we define A at the interface levels as

$$\hat{A}_{k+1/2} = (A_k + A_{k+1})/2.$$

In the case of potential temperature, we define

$$\hat{\theta}_{k+1/2} = \frac{(\hat{P}_{k+1/2} - P_k)\theta_k + (P_{k+1} - \hat{P}_{k+1/2})\theta_{k+1}}{P_{k+1} - P_k},$$

$$\hat{P}_{k+1/2} = (\hat{p}_{k+1/2}/p_0)^\kappa,$$

and

$$P_k = \frac{1}{1+k}\left[\frac{\hat{P}_{k+1/2}\,\hat{p}_{k+1/2} - \hat{P}_{k-1/2}\,\hat{p}_{k-1/2}}{\hat{p}_{k+1/2} - \hat{p}_{k-1/2}}\right],$$

which guarantees that θ is conserved (Arakawa and Suarez, 1983). The interface value for the dry static energy is obtained in the same way as for θ.

The hydrostatic equation is:

$$\begin{aligned} \varphi_L - \varphi_s &= c_p\theta_L(P_s - P_L), \\ \varphi_k - \varphi_{k+1} &= c_p\hat{\theta}_{k+1/2}(P_{k+1} - P_k). \end{aligned}$$

Note the different form for the lowest level.

Appendix C

Conservation equation for part or all of a grid cell

The formulation of the equations for subgrid-scale processes in cloud-free air in the convection scheme is aided by considering the conservation equation for some quantity ϕ. For example, the quantity ϕ might be the dry static energy, $s = c_pT + gz$, the specific humidity, q, the moist static energy, $h = s + Lq$, or a horizontal velocity component. We write the equation in flux form expressed in $\sigma-$coordinates. It is sufficient to consider the two-dimensional situation in the x-σ plane. The equation for ϕ is

$$\frac{\partial}{\partial t}(p^*\phi) + \frac{\partial}{\partial x}(p^*u\phi) + \frac{\partial}{\partial \sigma}(p^*\dot{\sigma}\phi) = p^*S_\phi, \qquad \text{(C.1)}$$

where S_ϕ is the mean rate-of-generation of ϕ. We define a horizontal average over a cloud-free air interval $\Delta x_{cf} = x_2 - x_1$, denoted by an overbar, and a vertical average over an interval $\Delta\sigma = \sigma_B - \sigma_A > 0$, denoted by $<(\ )>$, i.e.,

$$\overline{(\;)} = \frac{1}{\Delta x_{cf}} \int_0^{\Delta x_{cf}} (\;)\,dx, \qquad and \qquad <(\;)> = \frac{1}{\Delta\sigma} \int_{\sigma_A}^{\sigma_B} (\;)\,d\sigma. \tag{C.2}$$

In Fig. 8 , for example, $x_1 = \mu\Delta x$ and $x_2 = \Delta x$. Applying these integrals in succession to Eq. (C.1) and noting that they commute gives

$$\frac{\partial}{\partial t} < \overline{p^*\phi} > = -\frac{1}{\Delta x_{cf}} [< p^* u \phi >]_{x_1}^{x_2} - \frac{1}{\Delta\sigma}\left[\overline{p^*\dot{\sigma}\phi}\right]_{\sigma_A}^{\sigma_B} + < \overline{p^* S_\phi} > . \tag{C.3}$$

Putting $\phi = 1$ and $S_\phi = 0$ gives the mass continuity equation for the volume element $\Delta x_{cf}\Delta\sigma$:

$$\frac{\partial}{\partial t} < \overline{p^*} > = -\frac{1}{\Delta x_{cf}} [< p^* u >]_{x_1}^{x_2} - \frac{1}{\Delta\sigma}\left[\overline{p^*\dot{\sigma}}\right]_{\sigma_A}^{\sigma_B} . \tag{C.4}$$

We assume that $\overline{\dot{\sigma}\phi} = \overline{\dot{\sigma}}\,\overline{\phi}$, $< u\phi > = < u >< \phi >$ and that p^* is horizontally uniform over the interval Δx_{cf}. Thus subgrid-scale fluxes are assumed to be zero in the cloud-free air region within a grid box. Then, denoting the volume average of this element by $\widehat{(\;)} = < \overline{(\;)} >$ and subtracting $\hat{\phi}$ times Eq. (C.4) from Eq. (C.3) gives

$$p^*\frac{\partial\hat{\phi}}{\partial t} = -\frac{1}{\Delta x_{cf}}\left[p^* < u > (< \phi > - \hat{\phi})\right]_{x1}^{x2} - \frac{1}{\Delta\sigma}\left[p^*\overline{\dot{\sigma}}(\overline{\phi} - \hat{\phi})\right]_{\sigma_A}^{\sigma_B} + p^*\hat{S}_\phi. \tag{C.5}$$

In terms of the vertical mass flux per unit area defined in section 3.2, Eq. (C.5) takes the form

$$\alpha p^*\frac{\partial\hat{\phi}}{\partial t} = -\frac{1}{\Delta x_{cf}}\left[\alpha p^* < u > (< \phi > - \hat{\phi})\right]_{x1}^{x2} - \left[M(\overline{\phi} - \hat{\phi})\right]_{\sigma_A}^{\sigma_B} + \alpha p^*\hat{S}_\phi, \tag{C.6}$$

where $\alpha = (\sigma_B - \sigma_A)/g > 0$.

The term on the left-hand-side of Eq.(C.6) is the rate-of-change of the volume average of $\hat{\phi}$. The first two terms on the right-hand-side characterize the change in $\hat{\phi}$ associated with the mean horizontal flux of $\hat{\phi} - \phi_{boundary}$ through the sides of the element and the net vertical flux of $\hat{\phi} - \phi_{boundary}$ through the base $(\sigma = \sigma_B)$ and top $(\sigma = \sigma_A)$ of the element, where $\phi_{boundary}$ is the value of ϕ at the boundary. Note that these flux terms are zero when the flow is directed out of the volume element. The last term of Eq. (C.6) characterizes the mean source of $\hat{\phi}$ within the element.

In section 3.2, Eq. (C.6) is used to determine the time rate-of-change of s and q in the cloud-free regions of cells in a grid column that are deemed to contain deep convective cloud.

APPENDIX D

Calculation of the cumulus precipitation

Addition of Eqs. (24), (25) and (26) gives

$$p^* \frac{\partial}{\partial t}(\alpha_1 q_1 + \alpha_3 q_3 + \alpha_b q_b) = (M_{c2} q_{c1} - M_e q_3 - M_{c4} q_b) - \overline{M_2}(q_1 - q_3) - \overline{M_4}(q_3 - q_b). \tag{D.1}$$

The first term on the right-hand side is the rate of loss of water vapour to the deep convective clouds in a grid box. Because the clouds are assumed to be steady, this rate of water loss, minus that consumed in moistening precipitation-driven downdrafts is equal to the convective precipitation rate:

$$-M_{c2} q_{c1} + M_e q_3 + M_{c4} q_b - M_{d4}(q_{d4} - q_3). \tag{D.2}$$

The second and third terms on the right-hand-side of Eq. (D.1) represent the net moisture convergence into a column by the large-scale motion, but these do not represent the explicit precipitation as the net moisture in a column can change.

APPENDIX E

Maximum Potential Intensity (MPI)

The upper bound on tropical cyclone intensity is calculated using sea surface temperature and atmospheric thermodynamic profiles. The technique represents a generalization of an open-cycle heat engine. Following is the lists of the assumption of this calculation.

- The work done against friction in the tropical cyclone outflow is ignored.
- It is assumed that at maximum intensity, the anticyclone at the storm top is fully developed (zero absolute vorticity).
- The gradient wind may be approximated by the cyclostrophic wind at the radius of maximum winds.

For an axisymmetric vortex in gradient and hydrostatic balance, and for which the temperature lapse rate is moist adiabatic alone angular momentum surface, the thermal wind equation may be written (Emanuel, 1986)

$$\frac{1}{r_b^2} = \frac{1}{r_t^2} - 2c_p(T_s - T_0)\frac{1}{f^2 R^3}\frac{\partial(\log \theta_e^*)}{\partial R} \tag{E.1}$$

where r_b and r_t are the (physical) radii of angular momentum surfaces at the top of the boundary layer and at the tropopause, respectively, c_p is the heat capacity at constant pressure, T_s and T_0 are the surface temperature and temperature at the tropopause, respectively, θ_e^* is the saturation equivalent potential temperature, and R is the potential radius.

In a mature tropical cyclone, the anticyclone is well developed at the tropopause and so angular momentum surfaces flare out to very larger radius. Therefore the Eq. (E.1) may be approximated by assuming that r_t is infinitive:

$$\frac{1}{r_b^2} = -2c_p(T_s - T_0)\frac{1}{f^2R^3}\frac{\partial(ln\theta_e^*)}{\partial R} \tag{E.2}$$

In the boundary layer under the eyewall, we assume that, in the steady state, the radial advection of angular momentum and equivalent potential temperature are balanced by their sink and source at the sea surface:

$$-\frac{f}{2}\frac{\partial\psi_b}{\partial h}\frac{\partial R^2}{\partial r} = r\frac{\partial\tau_v}{\partial p} \qquad \overset{\int_{p_b}^{p_o}}{\rightarrow} \qquad -\frac{f}{2}\psi_b\frac{\partial R^2}{\partial r} = r\tau_{v0} \tag{E.3}$$

and

$$-c_p\frac{\partial\psi_b}{\partial h}\frac{\partial ln\theta_e}{\partial r} = \frac{1}{T_s}[\frac{\partial\tau_k}{\partial p} + \frac{1}{g}D] \qquad \overset{\int_{p_b}^{p_o}}{\rightarrow} \qquad -c_p\psi_b\frac{\partial ln\theta_e}{\partial r} = \frac{1}{T_s}[\tau_k + \frac{1}{g}\int_{p_b}^{p_o} Ddp] \tag{E.4}$$

where ψ is the mass streamfunction in the $r - p$ plane, τ_v is the vertical turbulent flux of azimuthal momentum, τ_k is the turbulent enthalpy flux, D is the dissipative heating rate and ψ_b is the mass streamfunction at the top of the boundary layer. It is assumed that $\psi = 0$ at the sea surface and R and θ_e are constant with altitude in the boundary layer.

The surface fluxes are given by the bulk aerodynamic formulae,

$$\tau_{v0} = -\rho C_D|\mathbf{V}|V, \tag{E.5}$$

$$\tau_{k0} = \rho C_k|\mathbf{V}|(k^* - k), \tag{E.6}$$

where ρ is the air density near the surface, C_D and C_k are the exchange coefficients for momentum and enthalpy, $|\mathbf{V}|$ is the magnitude of the surface wind speed, and k^* and k are the saturation enthalpy of the sea surface and the actual enthalpy of the boundary layer air, respectively.

The frictional heating of the boundary layer is given by,

$$\int_{p_b}^{p_o} Ddp = \rho C_D|\mathbf{V}|^3 \tag{E.7}$$

Now divide Eq. (E.4) by Eq. (E.3) and use Eqs. (E. 5-E. 7) to yield

$$-\frac{1}{R}\frac{\partial ln\theta_e}{\partial R} = \frac{f}{c_pT_s}\frac{1}{rV}[\frac{C_k}{C_D}(k^* - k) + |\mathbf{V}|^2] \tag{E.8}$$

It is further assumed that in the eyewall region, θ_e in the boundary layer is equal to θ_e^* along angular momentum surface above the boundary layer, the condition of slantwise convective neutrality. Then Eq. (E.8) can be substituted into Eq. (E.2) to give

$$\frac{R^2}{r_b^2} = 2\frac{T_s - T_0}{T_s}\frac{1}{frV}[\frac{C_k}{C_D}(k^* - k) + |\mathbf{V}|^2] \tag{E.9}$$

In the eyewall region it is assumed that $|\mathbf{V}| >> fr$, therefore the equation of angular momentum conservation, $fR^2 = fr^2 + 2rV$, can be simplified as $fR^2 = 2rV$, so that Eq. (E.9) can be written as,

$$V^2 = \frac{T_s - T_0}{T_s}[\frac{C_k}{C_D}(k^* - k) + |\mathbf{V}|^2] \tag{E.10}$$

Finally, using the approximation that $|\mathbf{V}|$ =V, then Eq. (E.10) becomes

$$V^2 = \frac{T_s - T_0}{T_0}\frac{C_k}{C_D}(k^* - k) \tag{E.11}$$

In the steady state, the maximum wind speed is in the eye wall region so that the value of V which is solved by Eq. (E.11) under the eye wall is the maximum gradient wind speed, V_m, that the mature tropical cyclone can achieve. Replacing V with V_m, Eq. (E.11) becomes,

$$V_m^2 = \frac{T_s - T_0}{T_0}\frac{C_k}{C_D}(k^* - k) \tag{E.12}$$

where V_m is the maximum gradient wind speed.

At the constant pressure, the moist enthalpy (k) can be represented by entropy (s) as $k = T * s$. The entropy can be represented by equivalent potential temperature (θ_e) as $k = c_p ln\theta_e$, so that Eq. (E.12) has another two forms:

$$V_m^2 = \frac{(T_s - T_0)T_s}{T_0}\frac{C_k}{C_D}(s^* - s), \tag{E.13}$$

and

$$V_m^2 = c_p(T_s - T_0)\frac{T_s}{T_0}\frac{C_k}{C_D}(ln\theta_e^* - ln\theta_e), \tag{E.14}$$

where s_* and s are the saturated entropy in the sea surface and the actual entropy in the boundary layer; θ_e^* and θ_e are the equivalent potential temperature in the sea surface and the actual potential temperature in the boundary layer. Equation (E. 13) can also be represented as an integral,

$$V_m^2 = \frac{1}{T_0}\frac{C_k}{C_D}\int_{T_0}^{T_s}(s^* - s)dT \tag{E.15}$$

From Emanuel 1994, Eq.6.4.2,

$$CAPE = \int_{T_n}^{T_i}(s_{pp}^* - s_{pa}^*)dT \tag{E.16}$$

It is assumed that the atmosphere in the tropics is close to a reversible moist adiabatic, then $(s_{pp}^* - s_{pa}^*)_B$ is constant with height and Eq. (E.16) becomes,

$$CAPE = (s_{pp}^* - s_{pa}^*)_B(T_s - T_0). \tag{E.17}$$

Through Eq. (E.17), Eq. (E.15) can be written as,

$$\begin{aligned}
V_m^2 &= \frac{C_k}{C_D}\frac{T_s}{T_0}(s^* - s_a^* + s_a^* - s)(T_s - T_0)\\
&= \frac{C_k}{C_D}\frac{T_s}{T_0}[(s^* - s_a^*) - (s - s_a^*))](T_s - T_0)\\
&= \frac{C_k}{C_D}\frac{T_s}{T_0}[(s^* - s_a^*)(T_s - T_0) - (s - s_a^*)(T_s - T_0)]\\
&= \frac{C_k}{C_D}\frac{T_s}{T_0}[CAPE^* - CAPE]_m
\end{aligned}$$

where $CAPE^*$ is the convective available potential energy of air lifted from saturation at sea level in the environmental sounding, and CAPE is that of boundary layer air. Both quantities are evaluated near the radius of maximum wind.

Appendix F

Derivation of the dissipative heating

The internal energy, momentum and mass conservation equation that form the basis of atmospheric modeling can be written as:

$$C_v\frac{DT}{Dt} = -\frac{p}{\rho}\bigtriangledown\cdot\mathbf{u} - \frac{1}{\rho}\bigtriangledown\cdot\mathbf{F} + Q_{cnd} + Q_{dis}, \tag{F.1}$$

$$\frac{D\mathbf{u}}{Dt} + 2\Omega\times\mathbf{u} = -\frac{1}{\rho}\bigtriangledown p - \bigtriangledown\Phi + \frac{1}{\rho}\bigtriangledown\cdot\boldsymbol{\tau}, \tag{F.2}$$

$$\frac{\partial\rho}{\partial t} + \bigtriangledown\cdot(\rho\mathbf{u}) = 0. \tag{F.3}$$

Here C_v the specific heat of air at constant column, Ω the angular velocity of the planet, $\mathbf{F}$ is the sum of the radiative heat flux and molecular heat flux, Q_{cnd} is the heating per unit mass due to condensation, Q_{dis} is the dissipative heating, $\boldsymbol{\tau}$ is the viscous stress tensor, and $\boldsymbol{\tau} = v \bigtriangledown \cdot \mathbf{u}$, where v is the kinetic viscosity.

Taking the dot product of $\mathbf{u}$ with Eq. (F.2) gives a kinetic energy equation:

$$\rho \frac{D}{Dt} \frac{u^2}{2} = -\mathbf{u} \cdot \bigtriangledown p - \rho \mathbf{u} \cdot \bigtriangledown \Phi + \bigtriangledown \cdot (\boldsymbol{\tau} \cdot \mathbf{u}) - \boldsymbol{\tau} \cdot (\bigtriangledown \mathbf{u}) \tag{F.4}$$

The final term represents the rate of dissipation of kinetic energy, a positive quantity for Newtonian fluids. With Φ steady, Eq. (F.1) and Eq. (F.4) combine to give

$$\rho \frac{DE}{Dt} = - \bigtriangledown \cdot (p\mathbf{u}) - \bigtriangledown \cdot \mathbf{F} + \rho Q_{cnd} + \rho Q_{dis} - \boldsymbol{\tau} \cdot (\bigtriangledown \mathbf{u}) \tag{F.5}$$

where the total energy, E, per mass is written as

$$E \equiv \frac{|\mathbf{u}|^2}{2} + c_v T + \Phi \tag{F.6}$$

In order that total energy is conserved,

$$\rho Q_{dis} = \boldsymbol{\tau} \cdot (\bigtriangledown \mathbf{u}) = v \cdot (\bigtriangledown \mathbf{u})^2. \tag{F.7}$$

While Eq. (F.7) applies in the interior of the fluid flow, the surface stress is often represented by a bulk aerodynamic formula of the form

$$v \frac{\partial u_i}{\partial x_3}|_0 = C_D u_i \sqrt{u_1^2 + u_2^2}, \qquad i = 1, 2 \tag{F.8}$$

where x_3 is the direction normal to the surface. (This equation applies only to u_1 and u_2, which are the winds in the surface.) Then, at the lowest model level, the frictional term in the thermodynamic equation is

$$\frac{C_D}{h}(u_1^2 + u_2^2)^{3/2}, \tag{F.9}$$

where h is the altitude above the sea level of the lowest model grid point.

APPENDIX G

Discrete equations for the CP-grid

Continuity Equation

$$\frac{\partial p^*}{\partial t} + \nabla \cdot (p^* \mathbf{v})_l + \frac{1}{(\Delta\sigma)_l}[(p^* \dot{\sigma})_{l+1/2} - (p^* \dot{\sigma})_{l-1/2}] = 0. \tag{G.1}$$

for l = 1, 2, ..., L.

where $(\Delta\sigma)_l = \sigma_{l+1/2} - \sigma_{l-1/2}$.

Boundary conditions

$$(p^*\dot{\sigma})_{1/2} = (p^*\dot{\sigma})_{L+1/2} = 0. \tag{G.2}$$

Thermodynamic energy equation

$$\begin{aligned}\frac{\partial}{\partial t}p^* c_p T_{l+1/2} + \nabla \cdot [(p^*\mathbf{v})_{l+1/2} c_p T_{l+1/2}] + \frac{c_p}{(\delta\sigma)_{l+1/2}}[(Tp^*\dot{\sigma})_{l+1} - ((Tp^*\dot{\sigma})_l] \\ = (p^*\alpha\omega)_{l+1/2} + (p^* Q_\theta)_{l+1/2}\end{aligned} \tag{G.3}$$

for l =1, 2, ..., L-1,

where

$$(p^*\mathbf{v})_{l+1/2} = \frac{1}{2(\delta\sigma)_{1+1/2}}[(\delta\sigma)_l (p^* v)_l + (\delta\sigma)_{l+1}(p^* v)_{l+1}] \tag{G.4}$$

for l = 1, 2, ..., L-1,

$$(\delta\sigma)_{l+1/2} = 0.5[(\delta\sigma)_l + (\delta\sigma)_{l+1}],$$

$$(Tp^*\sigma)_l = \frac{1}{2}[T_{l-1/2}(p^*\dot{\sigma})_{l+1/2} + T_{l+1/2}(p^*\dot{\sigma})_{l-1/2}] \tag{G.5}$$

for l = 1, 2, ..., L,

and

$$(p^*\alpha\omega)_{l+1/2} = \frac{RT_{l+1/2}}{p_{l+1/2}}[-p^* \times \sum_{k=1}^{l} \nabla \cdot (p^*\mathbf{v}_k)(\delta\sigma)_k + (p^*\mathbf{v})_{l+1/2} \cdot \nabla p_{l+1/2}] \tag{G.6}$$

for l = 1, 2, ..., L-1.

At the upper and lower boundaries,

$$\frac{\partial}{\partial t}p^* c_p T_{1/2} + \nabla \cdot [(p^*\mathbf{v})_1 c_p T_{1/2}] + \frac{c_p T_{1/2}}{(\delta\sigma)_l}(p^*\dot{\sigma})_{3/2} = (p^* Q_\theta)_{1/2}, \tag{G.7}$$

and

$$\begin{aligned}\frac{\partial}{\partial t}p^* c_p T_{L+1/2} + \nabla \cdot [(p^*\mathbf{v})_L c_p T_{L+1/2}] - \frac{c_p T_{L+1/2}}{(\delta\sigma)_L}(p^*\dot{\sigma})_{L-1/2} \\ = (p^*\alpha\omega)_{L+1/2} + (p^* Q_\theta)_{L+1/2}.\end{aligned} \tag{G.8}$$

In Eq.(G8),

$$(p^*\alpha\omega)_{L+1/2} = \frac{RT_{L+1/2}}{p_{L+1/2}}[-p^* \sum_1^L \nabla \cdot (p^*\mathbf{v}_k)(\delta\sigma)_k + (p^*\mathbf{v})_L \cdot \nabla p_{L+1/2}]. \tag{G.9}$$

Moist equation

$$\frac{\partial}{\partial t}p^* q_{l+1/2} + \nabla \cdot [(p^*\mathbf{v})_{l+1/2} q_{l+1/2}] + \frac{1}{(\delta\sigma)_{l+1/2}}[(p^* q\dot{\sigma})_{l+1} - ((p^* q\dot{\sigma})_l] = (p^* Q_q)_{l+1/2}. \tag{G.10}$$

for l = 1, 2, ..., L-1.

where $(p^*\mathbf{v})_{1+1/2}$ and $(\delta\sigma)_{l+1/2}$ is the same as the thermodynamic energy equation and

$$(p^* q\sigma)_l = \frac{1}{2}[p^* q_{l-1/2}\dot{\sigma}_{l-1/2} + p^* q_{l+1/2}\dot{\sigma}_{l+1/2}], \tag{G.11}$$

where the value of q and $\dot{\sigma}$ at the half levels are simply interpolated by an arithmetic average.

At the upper and lower boundaries,

$$\frac{\partial}{\partial t}p^* q_{1/2} + \nabla \cdot [(p^*\mathbf{v})_1 q_{1/2}] + \frac{q_{1/2}}{(\delta\sigma)_1}(p^*\dot{\sigma})_{3/2} = (p^* Q_q)_{1/2}, \tag{G.12}$$

and

$$\frac{\partial}{\partial t}p^* q_{L+1/2} + \nabla \cdot [(p^*\mathbf{v})_L q_{L+1/2}] - \frac{q_{L+1/2}}{(\delta\sigma)_L}(p^*\dot{\sigma})_{L-1/2} = (p^* Q_q)_{L+1/2}. \tag{G.13}$$

Hydrostatic equation

$$\Phi_l - \Phi_{l+1} = \frac{(p_{l+3/2} - p_{l-1/2})RT_{l+1/2}}{2p_{l+1/2}} \tag{G.14}$$

for l = 1, 2, ..., L-1.

At the lower boundary,

$$\Phi_L - \Phi_{L+1/2} = \frac{(p_{L+1/2} - p_{L-1/2})RT_{L+1/2}}{2p_{L+1/2}}. \tag{G.15}$$

Vertical mass flux

$$\dot{\sigma} = -\frac{1}{p^*}\sum_{k=1}^{l} \nabla \cdot (p^*\mathbf{v})_k(\delta\sigma)_k + \frac{\sigma}{p^*}\sum_{k=1}^{L} \nabla \cdot (p^*\mathbf{v})_k(\delta\sigma)_k. \tag{G.16}$$

for l = 1, 2, ..., L-1.

At the upper and lower boundaries, $(p^*\dot{\sigma})_{1/2} = (p^*\dot{\sigma})_{L/2} = 0$.

Horizontal pressure gradient force

In this model, the horizontal pressure gradient force is simply calculated by

$$-(\nabla_p \Phi)_l = -(\nabla_\sigma \Phi)_l - (\frac{RT\sigma}{p}\nabla p^*)_l. \tag{G.17}$$

In this formulation, mass conservation is satisfied also.

Reference

Anthes, R. A.	1972	Development of asymmetries in a three-dimensional numerical model of a tropical cyclone. *Mon. Wea. Rev.*, **100,** 461-476
Anthes, R. A., S. L. Rosenthal and J. W. Trout	1971a	Preliminary results from an asymmetric model of the tropical cyclone. *Mon. Wea. Rev.*, **99,** 744-758
Anthes, R. A., J. W. Trout and S. L. Rosenthal	1971b	Comparisons of tropical cyclone simulations with and without the assumption of circular symmetry. *Mon. Wea. Rev.*, **99,** 759-766
Anthes, R. A.	1979	Modelling of tropical cyclones and their environment. *Aust. Meteor. Mag.*, **27**, 213-228
Arakawa, A.	1969	Parameterization of cumulus convection. *Proc. WMO/IUGG Symp. Numerical Weather Prediction, Tokyo, 26 November - 4 December 1968, Japan Meteor. Agency IV*, **8,** 1-6
Arakawa, A., and W. H. Schubert	1974	Interaction of a cumulus cloud ensemble with the large-scale environment, Part I. *J. Atmos. Sci.*, **31,** 674-701
Arakawa, A.	1972	Design of the UCLA general circulation model. Numerical Simulation of Weather and Climate, *Tech. Rep. No.7, Dept. of Meteorology, University of California*, 116 pp
Arakawa, A., and V. Lamb	1977	Computational design of the basic dynamical processes of the UCLA general circulation model. *Methods in Computational Physics.* Vol. **17** J. Chang, Ed., Academic Press, 173-265
Arakawa, A., and M. J. Suarez	1983	Vertical differencing of the primitive equations in sigma coordinates. *Mon. Wea. Rev.*, **111,** 34-45
Arakawa, A., and S. Moorthi	1988	Baroclinic instability in vertically discrete systems. *J. Atmos. Sci.*, **45,** 1688-1707
Arakawa, A., and C. S. Konor	1996	Vertical differencing of the primitive equations based on the Charney-Phillips grid in hybrid $\sigma - p$ vertical coordinates. *Mon. Wea. Rev.*, **124,** 511-528
Betts, A. K.	1975	Parametric interpretation of trade-wind budget studies. *J. Atmos. Sci.,* **32,** 1934-1945
Betts, A. K.	1976	The thermodynamic transformation of the tropical subcloud layer by precipitation and downdrafts. *J. Atmos. Sci.,* **33,** 1008-1020
Betts, A. K.	1986	A new convective adjustment scheme. I. Observational and theoretical basis. *Quart. J. Roy. Meteor. Soc.*, **112,** 677-691
Betts, A. K.	1997	Parameterization of deep convection. *The physics and parameterization of moisture atmospheric convection. (Ed. R. K. Smith), Kluwer, Dorecht,* 255-279

Baik, J.-J., M. DeMaria, and S. Raman 1990a Tropical cyclone simulations with the Betts Convective adjustment scheme. Part I: Model description and control simulation *Mon. Wea. Rev.*, **118,** 513-528

Baik, J.-J., M. DeMaria, and S. Raman 1990b Tropical cyclone simulations with the Betts Convective adjustment scheme. Part II: Sensitivity experiments. *Mon. Wea. Rev.*, **118,** 529-541

Bister M. and K. A. Emanuel 1998 Dissipative Heating and Hurricane Intensity. *Meteorol. Atmos. Phys.*, **65,** 233-240

Bretherton, C.S. and P.K.Smolarkiewicz 1989 Gravity waves, compensating subsidence and detrainment around cumulus cloud. *J. Atmos. Sci.*, **46,** 740-759

Bretherton, C. S. 1993 The nature of adjustment in cumulus clouds fields. In *The representation of cumulus convection in numerical models (Ed. K. A. Emanuel and D. J. Raymond). American Meteorological Society, Meteorological Monograph,* No. **46,** 63-74

Charney, J. G., and N. A. Philips 1953 Numerical integration of the quasi-geostrophic equations for barotropic and simple baroclinic flows. *J.Meteor.*, **10,** 71-99

Cullen, M.J.P., and J.James 1994 A comparison of two different vertical grid staggerings. *Preprints, 10th Conf. on Numerical Weather Prediction, Portland, OR, Amer. Meteor. Soc.*, 38-40.

DeMaria, M., and J. D. Pickle 1988 A simplified system of equations for simulating tropical cyclones. *J. Atmos. Sci.*, **45,** 1542-1554

DeMaria, M., and J. Kaplan 1997 An operational evaluation of a statistical hurricane intensity prediction scheme(SHIPS). *Preprints of the 22nd Cond.on Hurricanes and Tropical Meteorology*, 280-281

Emanuel, K. A. 1986 An air-sea interaction theory for tropical cyclones. Part I: Steady-state maintenance. *J. Atmos. Sci.*, **43,** 585-604

Emanuel, K. A. 1989 The finite-amplitude nature of tropical cyclogenesis. *J. Atmos. Sci.*, **46,** 3431-3456

Emanuel, K. A. 1994 Atmospheric convection. *Oxford University Press. New York.*, 580pp

Emanuel, K. A. 1995a The behaviour of a simple hurricane model using a convective scheme based on subcloud-layer entropy equilibrium. *J. Atmos. Sci.*, **52,** 3960-3968

Emanuel, K. A. 1995b Sensitivity of tropical cyclones to surface exchange coefficients and a revised steady state model incorporating eye dynamics. *J. Atmos. Sci.*, **52,** 3969-3976

Emanuel, K. A. 1997 Overview of atmospheric convection. In *The physics and parameterization of moist atmospheric convection. (Ed. R.K. Smith) Kluwer, Dordrecht,* 1-28

Frank, W. M. 1983 The cumulus parameterization problem. *Mon. Wea. Rev.*, **111,** 1859-1871

Fiedler, B.H. 2000 Dissipative heating in climate models. *Quart. J. Roy. Meteor. Soc.*, **126,** 925-939

Gregory, D., J.-J. Morcrette, C. Jakob, A. C. M. Beljaars, and T. Stockdale 2000 Revision of convection, radiation, and cloud schemes in the ECMWF Integrated Forecasting System. *Quart. J. Roy. Meteor. Soc.*, **126,** 1685-1710

Haltiner, G. J., 1971 Numerical Weather Prediction. *John Wiley and Sons, New York,* 317

Hollingsworth, A. 1995 A spurious mode in the "Lorenz" arrangement of ϕ and T which does not exist in the "Charney-Philips" arrangement. *ECMWF Tech. Memo.* **211,** 12 pp.

Jorgensen, D. P. 1984 Mesoscale and convective-scale characteristics of mature hurricanes. Part II: Inner core structure of Hurricane Allen (1980). *J. Atmos. Sci.*, **41,** 1287-1311

Jordan, C. L. 1957 Mean soundings for the West Indies area. *J. Meteor.*, **15,** 91-97

Kitade, T. 1980 Numerical experiments of tropical cyclones on a plane with variable Coriolis parameter. *J. Meteor. Soc. Japan*, **58,** 471-488

Kuo, H. L. 1965 On the formation and intensification of tropical cyclones through latent heat release by cumulus convection. *J. Atmos. Sci.*, **22,** 40-63

Kuo, H. L. 1974 Further studies of the parameterization of the influence of cumulus convection on large-scale flow. *J. Atmos. Sci.*, **31,** 1232-1240

Kuo, Y.-H., J. F. Bresch, M.-D. Cheng, J. Kain, D. B. Parsons, W.-K. Tao, and D.-L. Zhang 1997 Summary of a mini-workshop on cumulus parameterization for mesoscale models. *Bull. Amer. Meteor. Soc.*, **78,** 475-491

Kitade, T. 1980 Numerical experiments of tropical cyclones on a plane with variable Coriolis parameter. *J. Meteor. Soc. Japan*, **58,** 471-488

Kurihara, Y. 1973 A scheme for moist convective adjustment. *Mon. Wea. Rev.*, **101,** 547-553

Kurihara, Y. and R. E. Tuleya 1974 Structure of a tropical cyclone developed in a three-dimensional numerical simulation model. *J. Atmos. Sci.*, **31,** 893-919

Kurihara, Y., and M. A. Bender 1980 Use of a movable nested-mesh model for tracking a small vortex. *Mon. Wea. Rev.*, **108,** 1792-1809

Lorenz, E. N., 1960 Energy and numerical weather prediction. *Tellus*, **12,** 364-373

Manabe, S., J. Smagorinsky, and R. F. Strickler 1965 Simulated climatology of a general circulation model with a hydrological cycle. *Mon. Wea. Rev.*, **93,** 769-798

Mapes, B. E. and R. A. Houze, Jr., 1992 An integrated view of the 1987 Australian summer monsoon and its mesoscale convective systems. Part I: Horizontal structure. *Quart. J. Roy. Meteor. Soc.*, **118,** 927-963

Mapes, B.E. 1993 Gregarious tropical convection. *J. Atmos. Sci.*, **50,** 2026-2037

Mapes, B. E., and P. Zuidema 1996 Radiative-dynamical consequences of dry tongues in the tropical troposphere. *J. Atmos. Sci.*, **53,** 620-638

Molinari, J., and M. Dudek 1992 Parameterization of convective precipitation in mesoscale numerical models: A critical review. *Mon. Wea. Rev.*, **120,** 326-344

Nguyen, C. M., R. K. Smith, H. Zhu, and W. Ulrich 2002 A minimal axisymmetric hurricane model. *Quart. J. Roy Met.*, in press

Nicholls, M. E., R. A. Pielke, and W. R. Cotton 1991 Thermally forced gravity wavesin an atmosphere at rest. *J. Atmos. Sci.*, **48,** 1869-1884

Ooyama, K. V. 1969 Numerical simulation of the life cycle of tropical cyclones. *J. Atmos. Sci.*, **26,** 3-40

Ooyama, K. V. 1982 A theory on parameterization of cumulus convection. *J.Meteor. Soc. Japan*, **49,** 744-756

Pielke R. A. 1984 Mesoscale numerical modelling. *Academic Press, New York*, 612pp

Pielke R. A. Jr., and C. W. Landsea 1998 Normalized hurricane damage in the United States 1925-95. *Weath. Forecast.*, **13,** 621-631

Raymond D. J., and K. A. Emanuel 1993 The Kuo parameterization scheme. In *The representation of cumulus convection in numerical models (Ed. K. A. Emanuel and D. J. Raymond). American Meteorological Society, Meteorological Monograph*, No. **46,** 145-147

Raymond, D. J. 1995 Regulation of moist convection over the West Pacific warm pool. *J. Atmos. Sci.*, **52,** 3945-3959

Randall, D. A., P. Ding, and D.-M. Pan 1997a The Arakawa-Schubert parameterization. *The physics and parameterization of moist atmospheric convection* (Ed. R.K. Smith). Kluwer, Dordrecht, 281-296.

Randall, D. A., D.-M. Pan, and D. G. Cripe 1997b Quasi-equilibrium. In *The physics and parameterization of moist atmospheric convection* (Ed. R.K. Smith). Kluwer, Dordrecht, 359-385

Rosenthal, S. L. 1970a Experiments with a numerical model of tropical cyclone development. *Mon. Wea. Rev.*, **98,** 106-120

Rosenthal, S. L. 1970b A circularly-symmetric primitive equation model of tropical cyclone development containing an explicit water-vapour cycle. *Mon. Wea. Rev.*, **98,** 643-663

Rosenthal, S. L. 1971 The response of a tropical-cyclone model to variations in boundary- layer parameters, initial conditions, lateral boundary conditions, and domain size. *Mon. Wea. Rev.*, **99,** 767-777

Rosenthal, S. L. 1979 The sensitivity of simulated hurricane development to cumulus parameterization details. *Mon. Wea. Rev.*, **107,** 193-197

Rotunno, R., and K. A. Emanuel 1987 An air-sea interaction theory for tropical cyclones. Part II: Evolutionary study using a nonhydrostatic axisymmetric numerical model. *J. Atmos. Sci.*, **44,** 542-561

Shapiro, L. J. 1992 Hurricane vortex motion and evolution in a three-layer model. *J. Atmos. Sci.*, **49,** 140-153

Shapiro, L. J., and H. E. Willoughby 1982 The response of balanced hurricanes to local sources of heat and momentum. *J. Atmos. Sci.*, **39,** 378-394

Shutts, G. J., and M. E. B. Gray 1994 A numerical modelling study of the geostrophic adjustment process following deep convection. *Quart. J. Roy. Meteor. Soc.*, **120,** 1145-1178

Smith, R. K. 2000 The role of cumulus convection in hurricanes and its representation in hurricane models. *Rev. Geophys.* **38,** 465-489

Smith, R. K., W. Ulrich and G. Dietachmayer 1990 A numerical study of tropical cyclone motion using a barotropic model. Part I: The role of vortex asymmetries. *Quart. J. Roy. Meteor. Soc.*, **116,** 337-362

Smith, R. K. 2002 A simple model of hurricane boundary layer. *Quart. J. Roy Met. Soc.* (accepted)

Tokioka, T. 1978 Some consideration on vertical differencing. *J. Meteor. Soc. Japan*, **56**, 89-111

Yamasaki, M. 1968a A tropical-cyclone model with parameterized partition of released latent heat. *J. Meteor. Soc. Japan*, **46,** 202-214

Yamasaki, M. 1968b Detailed analysis of a tropical-cyclone simulated with a 13-layer model. Papers in *Meteorology and Geophysics*, **20,** 559-585

Weber, H.C and R.K.Smith 1995 Data sparsity and the tropical cyclone analysis and prediction problem: some simulation experiment with a barotropic model. *Quart. J. Roy. Meteor. Soc.*, **121**, 631-654

Willoughby, H. E. 1999 Hurricane heat engines. *Nature*, **401,** 649-650

Wada, M. 1979 Numerical experiments of the tropical cyclone model by use of the Arakawa- Schubert parameterization. *J. Meteor. Soc. Japan*, **57,** 505-530

Zhu. H., R. K. Smith and W. Ulrich 2001 A minimal three-dimensional tropical cyclone model. *J. Atmos. Sci.*, **58,** 1924-1944

Zhu. H. and R. K. Smith 2002 The importance of three physical processes in a minimal three-dimensional tropical cyclone model. *J. Atmos. Sci.*, **59,** 1825-1840

Acknowledgement

Among the many people to whom I am indebted for help during my Ph.D study, I wish to express particular thanks to my supervisor, Prof. Roger K. Smith for providing me the oppotunity to work on this interesting and challenging field, tropical convection. With his generous enlightening and guiding, my work has turned out to be fruitful and effective. Meanwhile I am grateful to have had the opportunities to participate in many international conferences and to visit several meteorological research centres in Australia, the UK and the US.

I am also indebted to Dr. Wolfgang Ulrich who is always willing to help me solve numerical problems. With his help, I was able to develop the simple hurricane model. I also want to thank Dipl.-Met. Heinz Loesslein for his efforts in dealing with my computer problems all the time.

Further afield, I am grateful to Prof. Kerry Emanuel, Prof. David Raymond, Dr. Brian Mapes, Dr. Lloyd Shapiro and Dr. Sarah Jones for useful discussions and advice.

I acknowledge the help from my friends and colleges, Helga Weindel, Markus Adams, Dr. Maria Peristeri, Zsusznna Reichmann and Dr. Dominique Möller for the patient explanation whenever I have the problems with the language.

Above all, my profoundest thanks to my husband and my parents for their understanding and encouragement.

My work has been generously supported by US office of Naval Research.

Curriculum Vitae

Name: Hongyan Zhu

Date of Birth: 24 May 1971

Place of Birth: Shandong, China

Education:

Sep. 1989-Aug. 1993	B.S. Meteorology, NanJing Meteorology Institute
Sep. 1995-Aug. 1998	M.S. Meteorology, Chinese Academy of Meteorology Science
Nov. 1998-April 2002	Ph.D Meteorology, University of Munich

Employment:

Sep. 1993-Aug. 1995	Lecturer, NanChang Meteorology School
Nov. 1998-present	Research Scientist, Meteorological institute at the University of Munich